

# Chemical vapor deposition of thin films for 3D lithium-ion microbatteries

**Citation for published version (APA):**

Xie, J. (2016). *Chemical vapor deposition of thin films for 3D lithium-ion microbatteries*. [Phd Thesis 1 (Research TU/e / Graduation TU/e), Chemical Engineering and Chemistry]. Technische Universiteit Eindhoven.

**Document status and date:**

Published: 06/12/2016

**Document Version:**

Publisher's PDF, also known as Version of Record (includes final page, issue and volume numbers)

**Please check the document version of this publication:**

- A submitted manuscript is the version of the article upon submission and before peer-review. There can be important differences between the submitted version and the official published version of record. People interested in the research are advised to contact the author for the final version of the publication, or visit the DOI to the publisher's website.
- The final author version and the galley proof are versions of the publication after peer review.
- The final published version features the final layout of the paper including the volume, issue and page numbers.

[Link to publication](#)

**General rights**

Copyright and moral rights for the publications made accessible in the public portal are retained by the authors and/or other copyright owners and it is a condition of accessing publications that users recognise and abide by the legal requirements associated with these rights.

- Users may download and print one copy of any publication from the public portal for the purpose of private study or research.
- You may not further distribute the material or use it for any profit-making activity or commercial gain
- You may freely distribute the URL identifying the publication in the public portal.

If the publication is distributed under the terms of Article 25fa of the Dutch Copyright Act, indicated by the "Taverne" license above, please follow below link for the End User Agreement:

[www.tue.nl/taverne](http://www.tue.nl/taverne)

**Take down policy**

If you believe that this document breaches copyright please contact us at:

[openaccess@tue.nl](mailto:openaccess@tue.nl)

providing details and we will investigate your claim.

# Chemical Vapor Deposition of Thin Films for 3D Lithium-ion Microbatteries

PROEFSCHRIFT

ter verkrijging van de graad van doctor aan de Technische Universiteit  
Eindhoven, op gezag van de rector magnificus prof.dr.ir. F.P.T. Baaijens,  
voor een commissie aangewezen door het College voor Promoties, in het  
openbaar te verdedigen op dinsdag 6 december 2016 om 16:00 uur

door

Jie Xie

geboren te Hubei, China

Dit proefschrift is goedgekeurd door de promotoren en de samenstelling van de promotiecommissie is als volgt:

voorzitter:	prof.dr.ir. J.C. Schouten
1 <sup>e</sup> promotor:	prof.dr.ir. P.H.L. Notten
2 <sup>e</sup> promotor:	prof.dr.ir. R-A. Eichel (RWTH Aachen)
copromotor(en):	dr. D.L. Danilov
leden:	prof.dr. F.M. Mulder (TUD)
	prof.dr. C. Detavernier (Universiteit Gent)
	prof.dr. R.A. van Santen
	prof.dr. F. Roozeboom

*Het onderzoek of ontwerp dat in dit proefschrift wordt beschreven is uitgevoerd in overeenstemming met de TU/e Gedragscode Wetenschapsbeoefening.*

*I don't know anything, but I do know that everything is interesting if you go into it deeply enough."*

by Richard Feynman

Title: Chemical Vapor Deposition of Thin Films for 3D Lithium-ion Microbatteries  
Author: Jie Xie

A catalogue record is available from the Eindhoven University of Technology Library  
ISBN: 978-90-386-4164-5

The Research presented in this thesis has been financially supported by IWT Flanders (Belgium) under SBO project “SoS-Lion”.

Cover designed by Jie Xie. The front cover displays a schematic view of a 3D thin-film microbattery. Reprint from permission of John Wiley and Sons.

Printed by Gildeprint – The Netherlands

Copyright © 2016 by Jie Xie

All rights reserved. No part of this publication may be reproduced, stored in a retrieval system, or transmitted in any form or by any means without the prior written consent of the author.

# Table of Contents

Chapter 1 Introduction .....	1
1.1 Powering a smart society.....	2
1.2 Introduction to lithium-ion batteries .....	4
1.2.1 Traditional liquid lithium-ion batteries .....	4
1.2.2 All-solid-state lithium-ion microbatteries .....	6
1.3 Concept of three-dimensional (3D) microbatteries .....	9
1.4 Chemical vapor deposition.....	13
1.4.1 Types of CVD .....	13
1.4.2 Deposition processes of CVD .....	14
1.4.3 Kinetics and mass-transport mechanisms .....	15
1.5 Scientific questions and scope of this thesis .....	17
Chapter 2 Chemical Vapor Deposition of Lithium Phosphate.....	23
2.1 Introduction .....	24
2.2 Experimental details .....	24
2.2.1 Thin film deposition .....	25
2.2.2 Sample characterization .....	26
2.3 Kinetic investigation .....	27
2.4 Ionic conductivity.....	30
2.5 Stability window .....	31
2.5.1 Effect of current collectors .....	32
2.5.2 Combining the CV results on Pt and TiN substrates.....	33
2.6 3D deposition of LiPO .....	36
2.7 Conclusions .....	38
Chapter 3 Silicon Anode Materials for Microbatteries .....	41

3.1 Introduction .....	42
3.2 Si anodes with different morphology .....	42
3.2.1 Si nanowires .....	43
3.2.2 Si honeycombs .....	44
3.2.3 Si thin films .....	47
3.2.4 3D-deposited Si thin films.....	51
3.3 Protecting Si electrodes with LiPO solid electrolyte .....	53
3.3.1 Electrochemical tests.....	54
3.3.2 SEM analysis after cycling test .....	57
3.4 Conclusions .....	59
Chapter 4 Planar and 3D Deposition of $\text{Li}_4\text{Ti}_5\text{O}_{12}$ .....	63
4.1 Introduction .....	64
4.2 Experimental details .....	64
4.2.1 Thin film deposition .....	64
4.2.2 Sample characterization .....	65
4.3 Deposition on planar substrates.....	66
4.3.1 Adhesion with the Si/TiN/Pt substrate .....	66
4.3.2 Optimizing deposition parameters .....	67
4.4 Deposition on 3D substrates.....	75
4.5 LTO/LiPON/Li all-solid-state cell .....	78
4.6 Conclusions .....	80
Chapter 5 Deposition of 3D-Structured $\text{TiO}_2$ Electrodes.....	85
5.1 Introduction .....	86
5.2 Experimental details.....	88
5.2.1 Thin film deposition .....	88
5.2.2 Sample characterization .....	90

5.3 Results and discussion.....	90
5.4 Conclusions .....	97
Chapter 6 Modelling TiO <sub>2</sub> Deep Trench Deposition Process .....	101
6.1 Introduction .....	102
6.2 Experimental details.....	103
6.3 Deposition results.....	104
6.4 Theoretical considerations.....	107
6.4.1 System definitions .....	108
6.4.2 Monte-Carlo description .....	113
6.4.3 Monte-Carlo implementation .....	116
6.5 Simulation results and discussion .....	117
6.5.1 Estimation of deposition probability .....	117
6.5.2 Deposition efficiency .....	119
6.5.3 Distribution of precursor inside trench.....	121
6.5.4 Overview of deposition profiles.....	123
6.6 Conclusions .....	124
6.7 Appendix: Markov chains and integral equations.....	125
Chapter 7 Summary and Outlook.....	131
Acronyms .....	135
List of symbols.....	137
List of publications.....	139
Curriculum Vitae.....	141
Acknowledgements .....	143





# Chapter 1 Introduction

## ***Abstract***

This introductory chapter starts with a short overview of modern information society and explains the increasing demand for miniaturized integrated power sources. Furthermore, it explores state of the art technical aspects of solid state batteries and the concept of 3D-microbatteries. The working theory and parameters influencing film homogeneity of chemical vapor deposition, which is the main deposition method used in this thesis, are introduced. Finally, the scientific questions and scope of this thesis are outlined.



wants to buy a shirt can only choose from a range of available sizes rather than take the perfect size for himself. Nowadays, only wealthy people can afford customized services, while the majority is limited to standard mass production. The emerging Industry 4.0 is going to resolve the mismatch between the demand for customization and the need for production simplicity. Industry 4.0 is a collective term, embracing a number of contemporary automation, data exchange and manufacturing technologies. It had been defined as a general definition for technologies and concepts of value chain organization, which draws together cyber-physical systems, the IoT and the internet of services [8, 9]. In the modular-structured smart factories of Industry 4.0, cyber-physical systems monitor physical processes, create a virtual copy of the physical world and make decentralized decisions. Over the IoT, cyber-physical systems communicate and cooperate with each other and with humans in real time, and via the internet of services, both internal and cross-organizational services are offered and utilized by participants of the value chain [9].

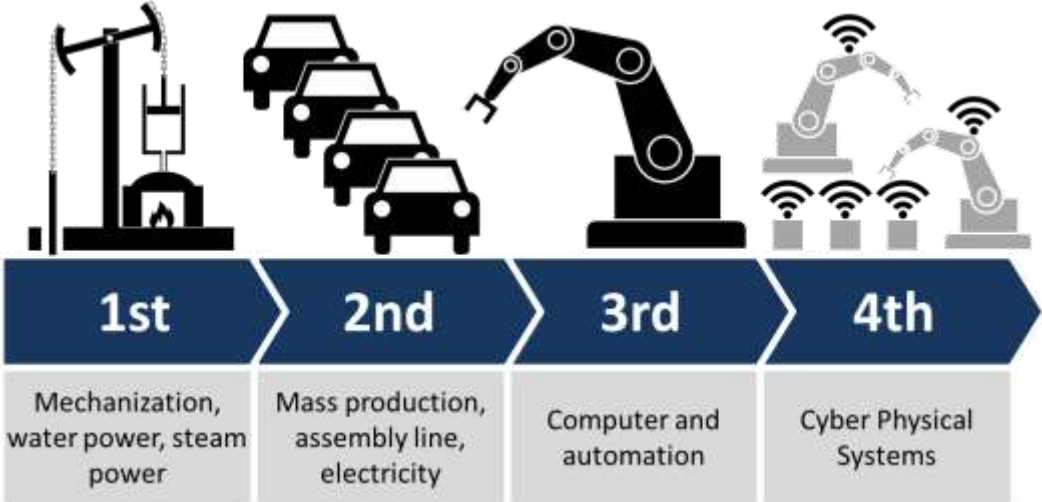


**Figure 1.2** The four industrial revolutions [10].

To reach the “ideal world” outlined by Figure 1.1 and Figure 1.2, thousands of wireless sensors united in networks have to be distributed [3, 4, 11-15]. To be easily embedded into other systems, these sensors must be very small. The micro-sensors can be much smaller than human fingertips and even smaller than a rice particle, as shown in Figure 1.3. Powering these micro-sensors will be challenging. For micro-devices, it is usually required that energy storage functions are physically located on a small chip area, thus micro-sized on-chip batteries would be highly desirable for these applications.

Up to recent times, just two types of technologies have been applied for these purposes: batteries and supercapacitors. Traditional liquid batteries, usually coin cells in the applications mentioned, are relatively large for the amount of power they deliver due to the packaging needed to contain their chemicals. Besides, the presence of liquid electrolyte inside makes these batteries incompatible with reflow soldering methods, which are widely used in semiconductor industry. Rechargeable conventional batteries are also limited by a low cycle life. Typically, they have to be replaced several times during the life-time of a product. Supercapacitors have a different set of drawbacks. Besides the drawbacks of high self-discharge and spark hazard, the output voltage of supercapacitors during discharging keeps decreasing. As a result, a voltage convertor is often needed, which adds to circuit complexity, device volume and cost. In short, chemical batteries and supercapacitors become obsolete for many applications in the face of continued miniaturization, integration and sophistication of new electronics products. Fortunately, solid-state microbatteries offer a potential solution.

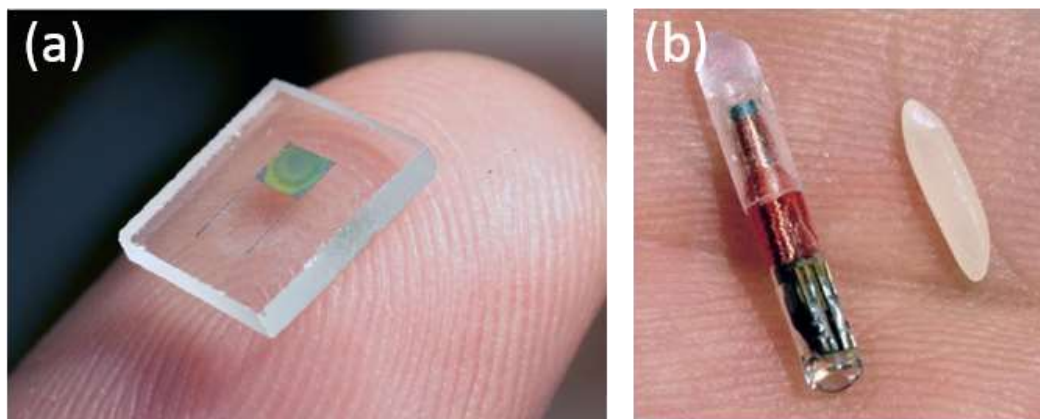


**Figure 1.3** A micro-sensor (a) and a radio frequency identification device (b).

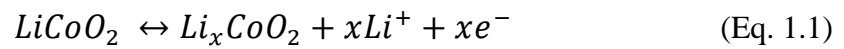
## 1.2 Introduction to lithium-ion batteries

### 1.2.1 Traditional liquid lithium-ion batteries

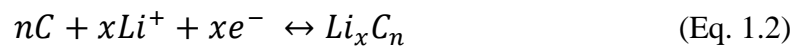
The mechanism for lithium-ion batteries is based on the transport of lithium-ion between the cathode and anode. The cathode usually consists of a lithium metal oxide (*e.g.*  $\text{LiCoO}_2$ ), whereas the anode usually consists of graphitic carbon <sup>[16-19]</sup>. The electrolyte is an organic solvent with a lithium salt dissolved in it <sup>[20, 21]</sup>. Separators for lithium ion batteries (polymer membranes) are used to prevent electrical contact between the electrodes. Such contact would result in internal short circuits inside the batteries and therefore give rise to a complete self-discharge. A typical example of a batteries based on Li-ion chemistry is shown in Figure 1.4.

During discharge, the lithium-ions stored in the negative electrode (anode), have a higher chemical potential and are driven via the electrolyte towards the positive electrode (cathode), which has a lower chemical potential. The charge-compensating electrons are forced to travel via the external circuit, providing the usable electrical energy. This change in lithium concentration in the electrode materials results in structural changes and phase transformations. During charging, the application of an external potential reverses the process and the lithium ions migrate back via the electrolyte to the negative electrode where they are reduced by the electrons. This discharge/charge process involves electronic and ionic charge transport in the electrodes and ionic transport in the electrolyte. Taking the classical  $\text{LiCoO}_2/\text{LiPF}_6/\text{C}(\text{graphite})$  cell as an example, the main storage reactions are described as follows

the cathode half-reaction is:



the anode half-reaction is:



The overall reaction is:

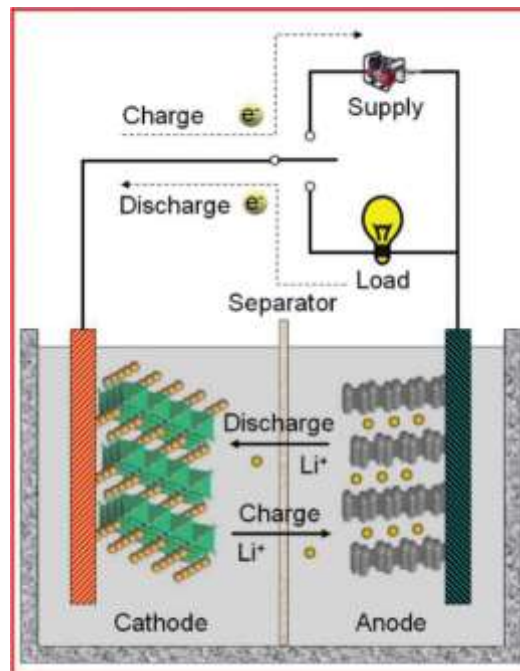
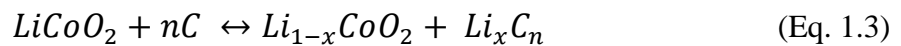


**Figure 1.4** Schematic representation of the operating principles of Li-ion batteries.

## 1.2.2 All-solid-state lithium-ion microbatteries

All-solid-state microbatteries do not principally differ in working mechanism from all other lithium-ion batteries, which also consist of two current collectors, two electrodes and an electrolyte in between as shown in Figure 1.5. The main difference between all-solid state and liquid electrolyte-based batteries is that the liquid electrolyte is substituted by a solid-state electrolyte and the separator is eliminated. Because of the packaging issue, conventional liquid electrolyte-based batteries usually cannot be smaller than typical coin cells. However, all-solid-state thin-film microbatteries can be manufactured with a footprint area of less than one millimeter <sup>[22]</sup>. Solid-state microbatteries are also much thinner than conventional liquid batteries: solid-state electrolytes have a typical thickness of approximately 1  $\mu\text{m}$ , whereas the separator in liquid electrolyte-based cells typically has a thickness of 20  $\mu\text{m}$ . Nanoscale electrolytes prepared in the form of thin films tend to reduce the overall weight and volume of the battery system, offering high energy density and long life cycles <sup>[23-27]</sup>.

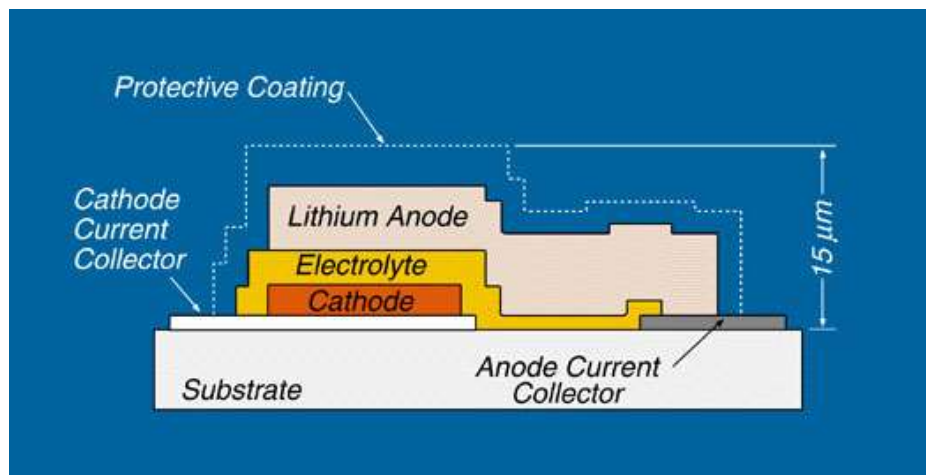


**Figure 1.5** Schematic representation of a planar all-solid-state microbatteries. <sup>[25]</sup>

To reach the goal of a high specific energy and power density, two fundamental requirements must be met by the electrode materials: (1) high specific energies (in Ah/kg) and high energy densities (in Ah/L) <sup>[28]</sup>, *i.e.* a high number of available charge carriers per mass and volume unit of the material; (2) the respective electrode redox reactions must deliver a high standard redox potential for the cathode and a low standard redox potential for the anode, leading to a high overall cell voltage. For a good rechargeable battery, the cycle life is also very important, which means the reactions at both electrodes have to be highly reversible to maintain the specific capacity for hundreds of charge/discharge cycles.

The requirements mentioned above are closely linked with the chemistry of the system. Among the various existing technologies, thin film lithium batteries are considered as the most competitive power source because of their high volumetric energy density and gravimetric energy density, superior power capability and design flexibility [24, 29-32]. Figure 1.6 shows the overview of volumetric and gravimetric energy densities for a number of competing chemistries. Obviously, thin film Li-ion batteries surpass other battery systems in both gravimetric energy density and volumetric energy density.

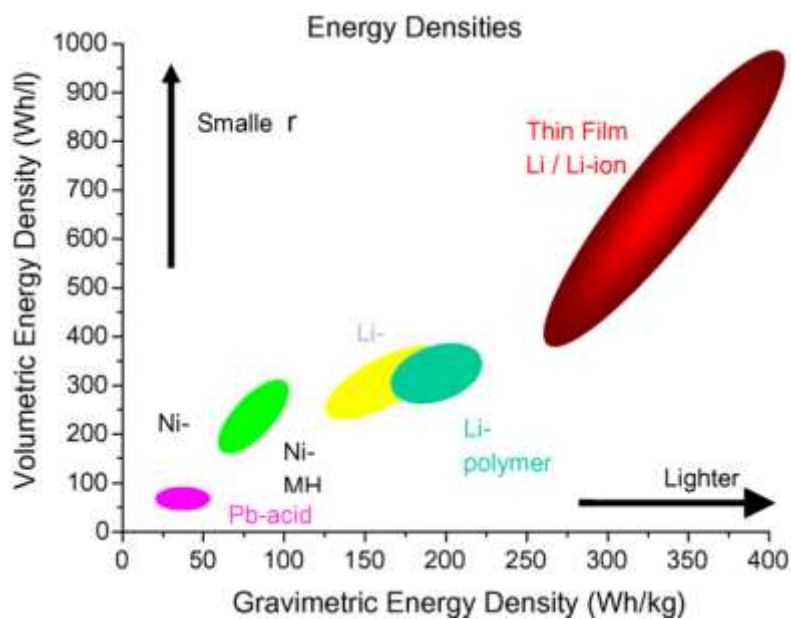


**Figure 1.6** Comparison of the volumetric and gravimetric energy density of various battery systems. [29]

In comparison with other battery systems and supercapacitors, all-solid-state batteries have the following advantages:

1. **High energy density.** For all-solid-state thin film batteries, the current collectors and thickness of the electrodes can be very thin (less than 100 nm), and the amount of inactive materials, such as carbon additives, PVDF binder and Cu/Al current collectors, can be sharply reduced. Thus, the energy density of the whole battery pack is improved because of the decrease of inactive components.
2. **Low self-discharge rate.** Due to the wider stability window and low electronic conductivity of solid electrolytes [33-35], side reactions and internal electricity leakage is very limited. The self-discharge rate of solid thin film batteries is very low.



3. **Long cycle life.** Nowadays, most of the commercial available solid state thin film batteries can surpass 5000 cycles. Some of them were even cycled over 10000 cycles <sup>[36]</sup>.
4. **Extremely small and thin (as low as 0.2 mm<sup>3</sup>).** Due to the advanced deposition techniques, thin film battery components can be deposited on various substrates. Without the worry of liquid electrolyte leakage, the packing process can be much simpler and thinner than conventional liquid-based batteries, which facilitate the miniaturization of thin film batteries.
5. **Compatibility with automated surface-mount technology (SMT) and reflow soldering processes.** The normal temperature of reflow soldering is around 217 °C which would vaporize the liquid electrolyte. However, this soldering temperature will not damage solid-state thin film batteries.
6. **Easy co-packaging with other devices.** Small size all-solid-state batteries are easy to be integrated in various devices. Figure 1.7 gives an example of an intraocular pressure monitoring device. A solar cell, a Cymbet EnerChip™ solid-state battery, a MEMS capacitive sensor, and integrated circuits, all these devices are vertically assembled in mini-scale biocompatible glass housing. Integrating a conventional rechargeable battery in such a small device would be impossible, especially considering the safety issue of electrolyte leakage.
7. **No hazardous chemicals.** Solid-state batteries are “registration, evaluation, authorization and restriction of chemicals” (REACH) compliant, as the systems do not contain hazardous substances from the “Substances of Very High Concern” (SVHC) candidate list published by the European Chemicals Agency. Solid-state batteries have also been tested for full compliancy with the EU’s Restriction of Hazardous Substances Directive (RoHS). Compliance with environmental regulations obviously results in lower manufacturing costs.
8. **No fire or explosion risk.** Unlike supercapacitors and coin cells, solid-state batteries contain no liquids, gels or harmful chemicals. Instead, all the components are made solely from semiconductor materials and ceramics, thus all the batteries components are solid and incombustible. That means no risk of leakage, corrosion, harm to the environment, or worries about shipping or disposal. Solid-state batteries are safe enough for use in electric vehicles and implanted medical devices, due to their intrinsic safety, health and environmental friendly.

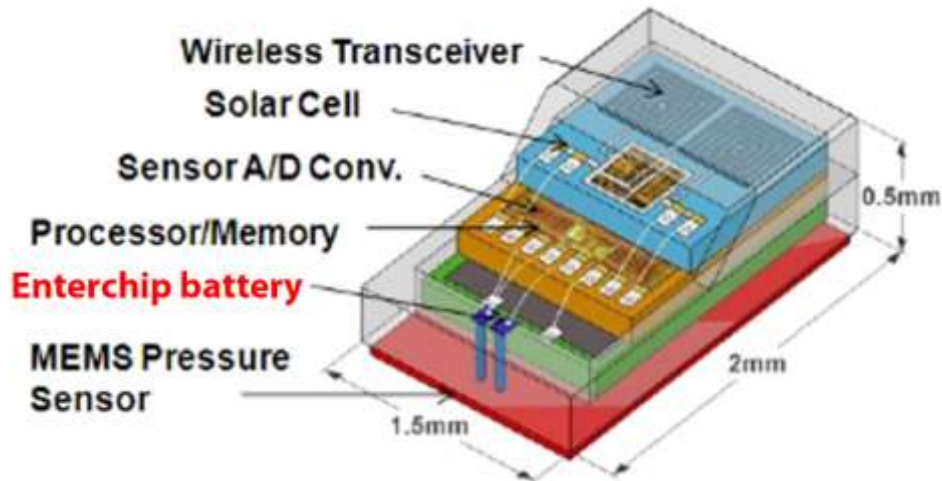


**Figure 1.7** A Cubic-millimeter energy-autonomous wireless intraocular pressure monitor <sup>[37]</sup>.

### 1.3 Concept of three-dimensional (3D) microbatteries

As explained in section 1.1, miniaturized batteries are highly desirable for applications in autonomous MEMS. Moreover, for use in miniaturized devices it is usually required that the energy storage functions are physically located on a small area of a chip, making the energy and power density per footprint area a key attribute of these batteries. Conventional 2D thin film microbatteries can deliver high power, but they require large footprints to provide reasonable energies. On the other hand, making the electrodes thicker boosts the theoretical areal energy density but also increases the electron and ion diffusion lengths, which reduces the effective power and energy densities. The most promising way to combine a high storage capacity and high power capability on a limited area is to integrate the battery components, current collectors, electrodes and electrolyte in a 3-dimensional (3D) arrangement, thus generating 3D microbatteries <sup>[38-43]</sup>. Due to the large available surface area of the electrodes, high capacities per footprint area can then be obtained. High power capabilities also can be achieved by careful design of the batteries to obtain short transport distances between the electrodes <sup>[34, 44, 45]</sup>.

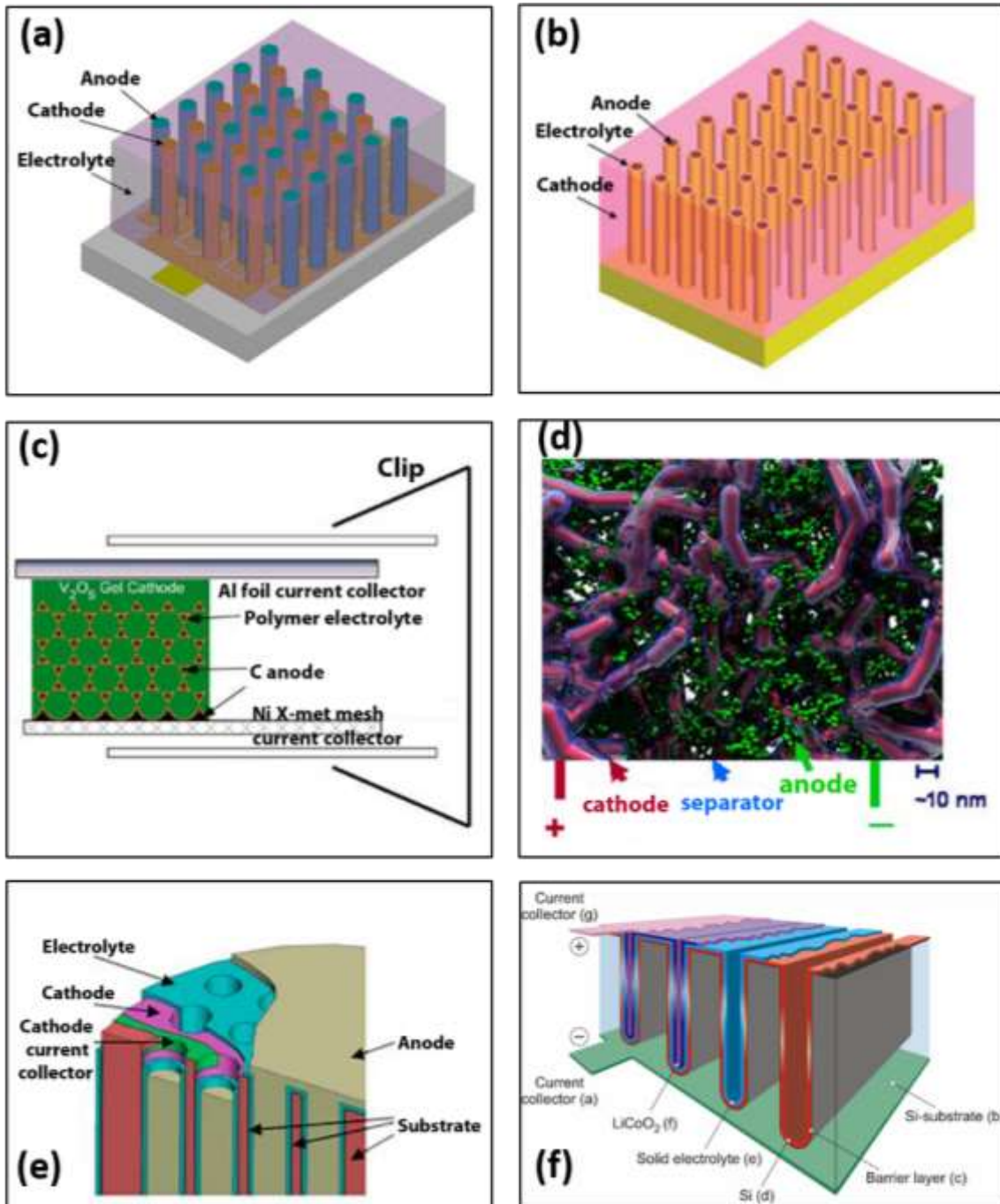


**Figure 1.8** 3D batteries designs: (a) interdigitated <sup>[46]</sup>, (b) concentric tube <sup>[47]</sup>, (c) inverse opal, (d) “sponge” batteries <sup>[48]</sup>, (e) perforated substrate <sup>[40]</sup>, and (f) micro-etched silicon <sup>[49]</sup>.

Various 3D batteries architectures were proposed by different groups. The interdigitated geometry (Figure 1.8a), in which anode and cathode arrays are separated by a continuous electrolyte phase, is perhaps the most easily visualized configuration <sup>[46, 50, 51]</sup>. The short transport distances between the electrodes and the increased interfacial areas lead to a much lower ohmic resistance as compared to traditional planar battery configurations. The concentric

arrangement (Figure 1.8b) has a 3D electrode array coated homogeneously by an electrolyte layer with the remaining free volume filled by the opposite electrode material <sup>[47]</sup>. This design not only provides short transport distances between the electrodes, but also leads to higher energy densities than the interdigitated configuration because of the lower volume fraction occupied by the electrolyte, which doesn't contribute to the storage capacity. The use of templating to form inverse opal structures has also served as the basis for fabricating 3D interpenetrating electrochemical cells <sup>[48]</sup>. The templated electrode is coated by an electrolyte and the remaining void space is filled with the opposite electrode material (Figure 1.8c).

In each of these designs, electrode arrays are formed in which the electrode material is configured in a spatially periodic way. Relaxing the periodicity condition, however, may be an important factor for achieving uniform current distribution. One example of an aperiodic 3D configuration is the “sponge” design <sup>[40]</sup>, in which the battery is constructed within a mesoporous aerogel nanoarchitecture. The electrolyte layer is conformally deposited around the spatially random 3D network of the electrode material. The other electrode material fills the remaining mesoporous and macroporous volume (Figure 1.8d). This design ensures that all batteries components: anode, cathode and electrolyte are continuous throughout the sponge structure.

Another type of 3D architecture is based on amplifying the area of thin film batteries, essentially by increasing the surface area of the substrate upon which the batteries is fabricated. One design uses a perforated substrate (glass or silicon microchannel plate) to serve as the fabrication template (Figure 1.8e) <sup>[52]</sup>. The battery is formed by sequential deposition of the current collector, cathode, and electrolyte, followed by filling the anode material into the center hole that remains after the deposition of the other components. Another thin-film approach is based on anisotropic etching of silicon substrates (Figure 1.8f) <sup>[49]</sup>. The first step in this approach is to use an anisotropic etching method to create a three dimensional structure in the substrate to enlarge the surface area. As etching techniques, either electrochemical or reactive ion etching can be applied <sup>[53]</sup>. The etched 3D structure typically consists of trenches <sup>[49]</sup>, but various other geometries can also be made, like pores or pillars <sup>[39, 54]</sup>. Commonly used dimensions for etched trench structures vary from 1 μm to 30 μm in width, and 10 ~ 100 μm in depth. The surface area enhancement (A) for a trench structure can be calculated according to

$$A = 1 + 2d \frac{L - s}{L(w + s)} \quad (\text{Eq. 1.4})$$

in which  $d$  is the trench depth,  $w$  the width,  $s$  the spacing between the trenches and  $L$  the total footprint length of the battery structure <sup>[55]</sup>. For example, a surface area enhancement of 28 times can be achieved by using  $d = 135 \mu\text{m}$ ,  $w = 5 \mu\text{m}$  and  $s = 5 \mu\text{m}$  for single-sided integration <sup>[55]</sup>, This value doubles for double-sided integration, as shown in Figure 1.9. Trench dimensions mentioned above can be achieved by using standard reactive ion etching technology.

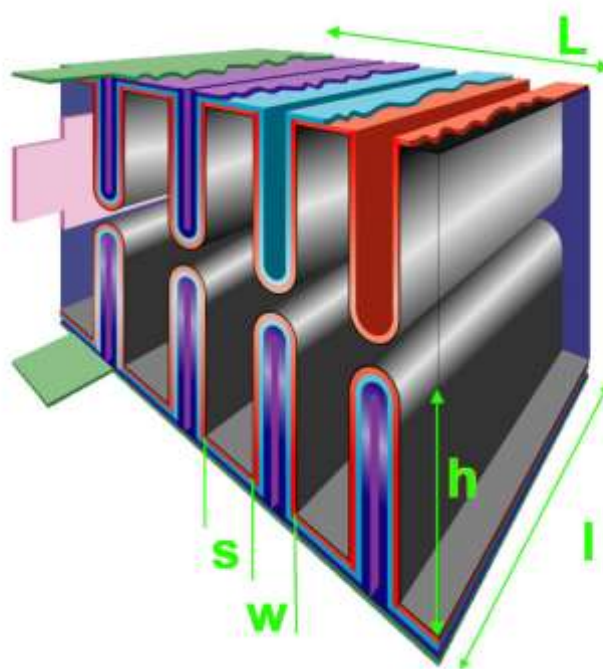


**Figure 1.9** Double side 3D microbattery.

The benefit of the approach shown in Figure 1.8f is that standard microelectronic techniques can be used, which makes integration into autonomous devices more straightforward and allows a simpler transfer to existing production facilities. Also the use of trench geometry is beneficial: the batteries mainly consists of parallel planar films inside the trenches and on top of the substrate, and the risk for local overcharging is therefore reduced. Using a solid-state electrolyte represents another advantage of this concept. Therefore, a longer cycle-life is expected and no leakage risks are present, which expands the possible application fields. What's more, trench structures are mechanically more stable. However, on the other hand, it is the relatively complicate structure, which makes deposition of step-conformal batteries layers challenging. To prevent the batteries from local over(dis-)charging or self-discharge, the cathode film, the electrolyte and the anode have preferably to be deposited step-conformal. To meet this requirement, techniques such as chemical vapor deposition (CVD), atomic layer deposition (ALD) or electrodeposition can be employed to deposit the batteries layers. The CVD technique

and the conditions for successful 3D deposition, will be described in more detail in the following section.

## 1.4 Chemical vapor deposition

In the broadest sense, CVD involves the formation of a thin solid film on a substrate material by a chemical reaction of vapor-phase precursors. The chemical reactions of precursor species occur both in the gas phase and on the substrate. Reactions can be promoted or initiated by heat (thermal CVD), high frequency radiation such as UV (photo-assisted CVD) or plasma (plasma-enhanced CVD) [56-58].

### 1.4.1 Types of CVD

The term of CVD was first introduced by John Blocker at the 1960 symposium of the Electrochemical Society in Houston. Since that time, the terms “chemical vapor deposition” and “physical vapor deposition” have been universally adopted [59]. After decades of developments, CVD is practiced in a variety of formats, such as Reduced Pressure CVD (RPCVD), Plasma-Enhanced CVD (PECVD), Metal-Organic (MOCVD), Low-Pressure (LPCVD), Plasma-Assisted Metal-organic CVD (PAMOCVD), Ultra-High Vacuum CVD (UHVCVD), Laser-Assisted CVD (LACVD), Very Low-Pressure CVD (VLPCVD), Rapid Thermal Low Pressure (RTLPCVD), Electron Cyclotron Resonance CVD (DECRCVD), *etc.* [59]. Some of the more commonly used acronyms are defined below.

MOCVD is a specific type of CVD that utilizes metal-organic precursors. In the strictest sense, a metal-organic (or organometallic) compound contains a direct metal–carbon bond (s or p) (*e.g.* metal alkyls, metal carbonyls). However, the definition of MOCVD has broadened to include precursors containing metal–oxygen bonds (*e.g.* metal-alkoxides, metal-b-diketonates) or metal–nitrogen bonds (*e.g.* metal alkylamides), and even metal hydrides (*e.g.* trimethylamine alane).

PECVD is a technique in which electrical energy rather than thermal energy is used to initiate homogeneous reactions for the production of chemically active ions and radicals that can participate in heterogeneous reactions which, in turn, lead to layer formation on the substrate. A major advantage of PECVD over thermal CVD processes is that deposition can occur at very low temperatures, even close to ambient, which allows temperature sensitive substrates to be used [60].

The low pressure distinguishes LPCVD from other CVD processes. The main reason for using LPCVD instead of atmospheric pressure CVD (APCVD) is the lower Damköhler number ( $D_a$ ).

$$D_a = \frac{\text{Reaction rate}}{\text{mass-transfer rate}} \quad (\text{Eq. 1.5})$$

$D_a$  is a useful ratio for determining whether mass-transfer or reaction are the rate-limiting step. For  $D_a \gg 1$ , the reaction rate is much greater than the mass-transfer rate. The CVD process is mass-transfer controlled. For  $D_a \ll 1$ , mass-transfer occurs much faster than the reaction. In this case, the CVD process is kinetically controlled.

During APCVD, the ratio is close to one as the two rates are of the same order of magnitude. The mass-transfer rate depends mainly on the reactant concentration, diffusion, and thickness of the boundary layer. When the pressure is lowered during LPCVD, the diffusion rate ( $D$ ) of the gas increases proportionally to the reciprocal of the pressure<sup>[61]</sup>, according to

$$D \propto \frac{T^{3/2}}{P} \quad (\text{Eq. 1.6})$$

where  $T$  is temperature,  $P$  is pressure. This means that rate of mass transport will increase at lower pressure, meaning the substrates can approach more closely to the bulk gas phase. So, the deposition process is less dependent on the mass transport limitation. The advantages of LPCVD include excellent uniformity of thickness and quality, simple handling, high reliability, homogeneity of deposited layers and high reproducibility. Disadvantages include lower deposition rates than APCVD and high deposition temperatures.

#### 1.4.2 Deposition processes of CVD

CVD processes are extremely complex and involve a series of gas-phase and surface reactions, such as thermal decomposition (pyrolysis), reduction, hydrolysis, disproportionation, oxidation, carburization, and nitridation. These processes can be used either separately or in combination. These reactions can be activated by several methods: thermal activation, plasma activation and photon activation. Figure 1.10 schematically shows a typical thermal activated CVD process. An important feature of the process is the presence of a hot layer of gas just above the substrate, termed the ‘‘boundary layer’’. Gas-phase pyrolysis reactions occurring in the boundary layer play a significant role in the MOCVD deposition process<sup>[58, 62, 63]</sup>. The key steps are listed below:

1. Evaporation and transport of reagents (*i.e.* precursors) in the bulk gas phase, transport of the gas into the reactor;
2. Gas phase reactions of precursors in the reaction zone to produce reactive intermediates and gaseous by-products;
3. Mass transport of reactants to the substrate surface;
4. Adsorption of the reactants on the substrate surface;
5. Surface diffusion to growth sites, nucleation and surface chemical reactions leading to film formation;
6. Desorption and mass transport of remaining fragments of the decomposition away from the reaction zone.

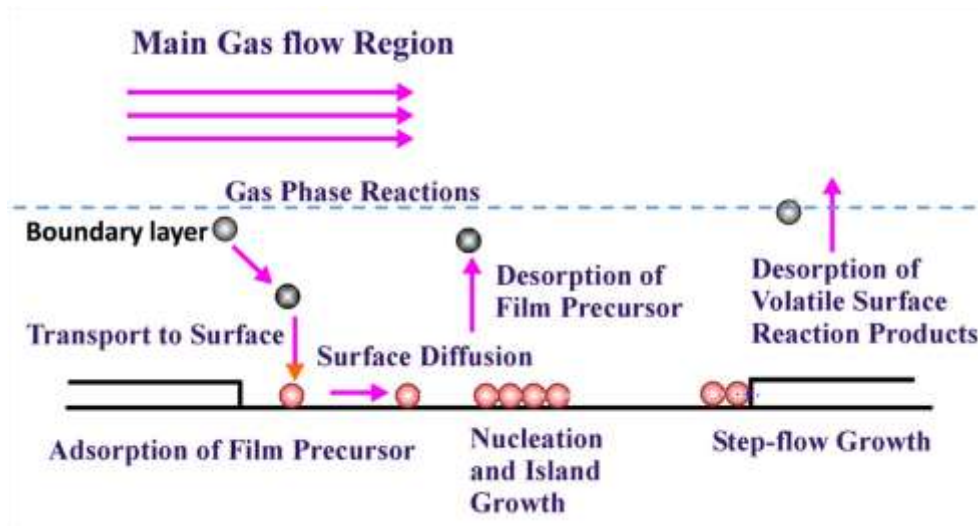


**Figure 1.10** Schematic representation of a typical CVD process.

### 1.4.3 Kinetics and mass-transport mechanisms

In a traditional thermal CVD process, the film growth rate is determined by several parameters. The primary ones include the temperature of the substrate, the operating pressure of the reactor and the chemistry of the gas-phase. A typical growth rate as a function of substrate temperature is shown in Figure 1.11. At low temperatures, the surface reaction is slow, meaning there is surplus of reactants at the substrate surface and the surface reaction is sensitive to the temperature. Therefore, the deposition process is surface-reaction kinetically limited. In this case, the growth rate increases with increasing temperature and is also affected by the substrate orientation. As the film growth rate is controlled by surface reaction rather than precursor



diffusion, uniform film thickness can be achieved by minimizing the temperature variations over the substrate surface. Such technique is applied in hotwall batch reactors used for the commercial production of Si epitaxial wafers by LPCVD.

As the temperature increases, the growth rate becomes nearly independent of temperature and is controlled by the mass transport of reagents through the boundary layer to the growth surface. This growth regime is called ‘mass transport’ or ‘diffusion-controlled’ growth. At even higher temperatures, the growth rate tends to decrease, due to an increased rate of desorption of precursors or matrix elements from the growth surface and/or depletion of reagents due to parasitic gas-phase side reactions. Gas-phase reactions become increasingly important with increasing temperature and higher partial pressures of the reactants.

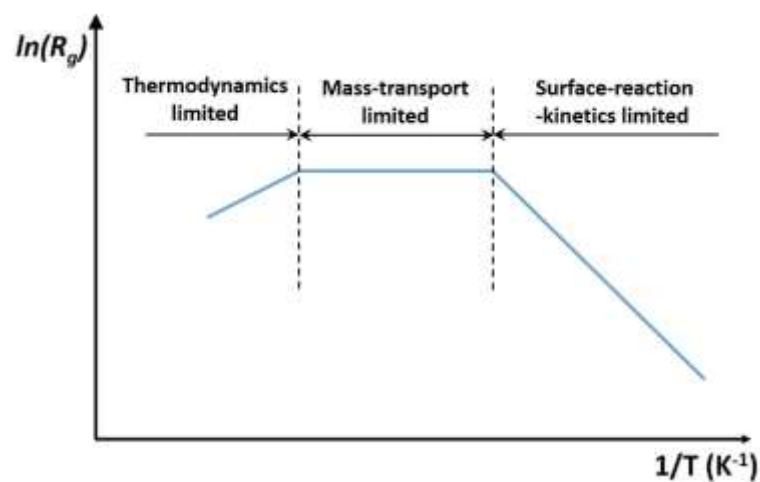


**Figure 1.11** Rate-limiting step as a function of substrate temperature during thin film deposition.

Note that in reality there is no sharp boundaries between these three regions. Usually, mixed regimes are present. Another crucial factor that determines the relative importance of each regime is the pressure of the CVD reactor. From atmospheric pressure (1 bar) to intermediate pressures (*e.g.* 20 mbar) gas phase reactions are important and, in addition, a significant boundary layer is present. Kinetics and mass transport can both play a significant role in the deposition process. As the pressure decreases, gas phase reactions tend to become less important, and particularly at pressures below 10 mbar, layer growth is often controlled by the surface reactions. At very low pressures (*e.g.* 0.1 mbar), mass transport is completely absent and the layer growth is primarily controlled by the gas and substrate temperature and by desorption of precursor fragments and matrix elements from the surface.

## 1.5 Scientific questions and scope of this thesis

Nowadays a new challenging application for Li-ion batteries emerged from the rapid development of micro-electronics. Powering MEMS such as smart sensors using conventional Li-ion batteries is not possible. New batteries based on new materials must be explored, but there is also a need for changes in the design of batteries. Moving from planar structures to high-aspect ratio 3D-structures promises a significant increase in the energy and power densities of microbatteries. This thesis focuses on the deposition and (electro-)chemical characterization of electrode and electrolyte films for all-solid-state 3D-integrated thin-film microbatteries. This study will deal with various aspects, including the effects of the deposition parameters on the properties of the deposited layers. Moreover, the deposition process will be more closely examined with simulations and theoretical modeling. All these topics are crucial steps on the road towards a more detailed understanding of the deposition processes of 3D-integrated microbatteries.

Chapter 1 gives a short overview of modern information society and the increasing demand for miniaturized integrated power sources. Furthermore, it reviews technical aspects of the state of art for solid-state batteries, the 3D concept of microbatteries and the application of CVD.

Chapter 2 systematically investigates LPCVD deposition of lithium phosphate to be used as a solid-state electrolyte.  $\text{Li}_3\text{PO}_4$  films have also been deposited on 3D substrates to investigate the feasibility of 3D deposition of  $\text{Li}_3\text{PO}_4$  by LPCVD.

Chapter 3 gives a short overview of Si anodes with different morphologies. The lithiation process and influence of cutoff voltage on the electrochemical performance of Si anode is investigated.  $\text{Li}_3\text{PO}_4$  films are applied as a protective layer to improve the cycle life of Si film electrodes.

Chapter 4 will focus on the synthesis of  $\text{Li}_4\text{Ti}_5\text{O}_{12}$  electrode. The influences of various deposition parameters, including flow rates of precursors and post-anneal temperatures, have been investigated by material and electrochemical analyses. Thin films were also deposited on highly structured substrates to investigate the uniformity and electrochemical performance.

Chapter 5 reports the deposition of 3D  $\text{TiO}_2$  film anodes. Kinetic studies on planar substrates and film thickness evolution on 3D substrates were investigated. Furthermore, the electrochemical performances of 3D  $\text{TiO}_2$  electrodes are characterized.

Chapter 6 investigated the film thickness profiles of deposited TiO<sub>2</sub> inside trench substrates at various deposition conditions. A Markov Chain Monte-Carlo model was developed to simulate the deposition process. An estimation of the parameters of the deposition process was performed and applied to predict the layer thickness profiles in narrow trenches.

Chapter 7 will finally evaluate the experiments described in this thesis, and give some recommendations for further research.

## References

1. L. Atzori, A. Iera, and G. Morabito, *The Internet of Things: A survey*. Computer Networks **54** (2010) 2787-2805.
2. H. Kopetz, *Internet of Things*, in *Real-Time Systems: Design Principles for Distributed Embedded Applications*. 2011, Springer US: Boston, MA. p. 307-323.
3. S. Abdelwahab, B. Hamdaoui, M. Guizani, and A. Rayes, *Enabling Smart Cloud Services Through Remote Sensing: An Internet of Everything Enabler*. IEEE Internet of Things Journal **1** (2014) 276-288.
4. Libelium. *Libelium Smart World Infographic – Sensors for Smart Cities, Internet of Things and beyond*. [cited 2016 3 April]; Available from: <http://www.libelium.com/libelium-smart-world-infographic-smart-cities-internet-of-things/>.
5. J. Lee, H.-A. Kao, and S. Yang, *Service Innovation and Smart Analytics for Industry 4.0 and Big Data Environment*. Procedia CIRP **16** (2014) 3-8.
6. H. Lasi, P. Fettke, H.-g. Kemper, T. Feld, and M. Hoffmann, *Industry 4.0*. Business & Information Systems Engineering **6** (2014) 239-242.
7. N. Jazdi. *Cyber physical systems in the context of Industry 4.0*. in *Automation, Quality and Testing, Robotics, 2014 IEEE International Conference on*. 2014.
8. K. Schwab, *The Fourth Industrial Revolution*, World Economic Forum (2016).
9. M. Hermann, T. Pentek, and B. Otto, *Design Principles for Industrie 4.0 Scenarios*, in *2016 49th Hawaii International Conference on System Sciences (HICSS)*. 2016: Hawaii p. 3928-3937.
10. Wikipedia. *Industry 4.0*. *Wikipedia, The Free Encyclopedia*. 2016; Available from: [https://en.wikipedia.org/w/index.php?title=Industry\\_4.0&oldid=711066849](https://en.wikipedia.org/w/index.php?title=Industry_4.0&oldid=711066849).
11. M. Zougagh and A. Rios, *Micro-electromechanical sensors in the analytical field*. Analyst **134** (2009) 1274-1290.
12. J.F.M. Oudenhoven, R.J.M. Vullers, and R. Schaijk, *A review of the present situation and future developments of micro-batteries for wireless autonomous sensor systems*. International Journal of Energy Research **36** (2012) 11391150.
13. C. Hagleitner, A. Hierlemann, D. Lange, A. Kummer, N. Kerness, O. Brand, and H. Baltes, *Smart single-chip gas sensor microsystem*. Nature **414** (2001) 293-296.
14. D.C. Bock, A.C. Marschilok, K.J. Takeuchi, and E.S. Takeuchi, *Batteries used to power implantable biomedical devices*. Electrochimica Acta **84** (2012) 155-164.
15. A.C. Fischer, F. Forsberg, M. Lapisa, S.J. Bleiker, G. Stemme, N. Roxhed, and F. Niklaus, *Integrating MEMS and ICs*. Microsystems & Nanoengineering **1** (2015) 15005.
16. J.M. Tarascon and M. Armand, *Issues and challenges facing rechargeable lithium batteries*. Nature **414** (2001) 359-367.
17. J.B. Goodenough and Y. Kim, *Challenges for Rechargeable Li Batteries*. Chemistry of Materials **22** (2010) 587-603.
18. K. Mizushima, P.C. Jones, P.J. Wiseman, and J.B. Goodenough, *Li<sub>x</sub>CoO<sub>2</sub> (0<x<-1): A new cathode material for batteries of high energy density*. Materials Research Bulletin **15** (1980) 783-789.

19. H. Buqa, R.I.R. Blyth, P. Golob, B. Evers, and I. Schneider..., *Negative electrodes in rechargeable lithium ion batteries—Influence of graphite surface modification on the formation of the solid electrolyte interphase*. *Ionics* (2000).
20. X. Kang, *Nonaqueous Liquid Electrolytes for Lithium-Based Rechargeable Batteries*. *Chemical Reviews* **104** (2004).
21. D. Aurbach, *Review of selected electrode–solution interactions which determine the performance of Li and Li ion batteries*. *Journal of Power sources* **89** (2000) 206-218.
22. K. Edström, D. Brandell, T. Gustafsson, and L. Nyholm, *Electrodeposition as a Tool for 3D Microbattery Fabrication*. *The Electrochemical Society interface* **20** (2011) 41-46.
23. J.B. Bates, N.J. Dudney, G.R. Gruzalski, R.A. Zuhr, A. Choudhury, C.F. Luck, and J.D. Robertson, *Fabrication and Characterization of Amorphous Lithium Electrolyte Thin-Films and Rechargeable Thin-Film Batteries*. *Journal of Power Sources* **43** (1993) 103-110.
24. J.B. Bates, N.J. Dudney, D.C. Lubben, G.R. Gruzalski, B.S. Kwak, X. Yu, and R.A. Zuhr, *Thin-film rechargeable lithium batteries*. *Journal of Power Sources* **54** (1995) 58-62.
25. J. Bates, *Thin-film lithium and lithium-ion batteries*. *Solid State Ionics* **135** (2000).
26. N.J. Dudney, *Solid-state thin-film rechargeable batteries*. *Materials Science and Engineering: B* **116** (2005) 245-249.
27. Y.N. Zhou, M.Z. Xue, and Z.W. Fu, *Nanostructured thin film electrodes for lithium storage and all-solid-state thin-film lithium batteries*. *Journal of Power Sources* **234** (2013) 310332.
28. P.G. Bruce, S.A. Freunberger, L.J. Hardwick, and J.-M.M. Tarascon, *Li-O<sub>2</sub> and Li-S batteries with high energy storage*. *Nature materials* **11** (2012) 19-29.
29. A. Patil, V. Patil, D.W. Shin, J.W. Choi, D.S. Paik, and S.J. Yoon, *Issue and challenges facing rechargeable thin film lithium batteries*. *Materials Research Bulletin* **43** (2008) 19131942.
30. K. Takada, *Progress and prospective of solid-state lithium batteries*. *Acta Materialia* **61** (2013) 759770.
31. J.G. Kim, B. Son, S. Mukherjee, N. Schuppert, A. Bates, O. Kwon, M.J. Choi, H.Y. Chung, and S. Park, *A review of lithium and non-lithium based solid state batteries*. *Journal of Power Sources* **282** (2015) 299-322.
32. Y. Wang, B. Liu, Q. Li, S. Cartmell, S. Ferrara, Z.D. Deng, and J. Xiao, *Lithium and lithium ion batteries for applications in microelectronic devices: A review*. *Journal of Power Sources* **286** (2015) 330-345.
33. H.T. Kim, T. Mun, C. Park, S.W. Jin, and H.Y. Park, *Characteristics of lithium phosphorous oxynitride thin films deposited by metal-organic chemical vapor deposition technique*. *Journal of Power Sources* **244** (2013) 641645.
34. J. Xie, J.F.M. Oudenhoven, P.P.R.M.L. Harks, D.J. Li, and P.H.L. Notten, *Chemical Vapor Deposition of Lithium Phosphate Thin-Films for 3D All-Solid-State Li-Ion Batteries*. *Journal of the Electrochemical Society* **162** (2015) A249-A254.
35. P. Knauth, *Inorganic solid Li ion conductors: An overview*. *Solid State Ionics* **180** (2009) 911-916.
36. Excellatron. *advantage of thin film batteries*. [cited 2016 10 May]; Available from: <http://www.excellatron.com/advantage.htm>.
37. G. Chen, H. Ghaed, R.u. Haque, M. Wieckowski, Y. Kim, G. Kim, D. Fick, D. Kim, M. Seok, K. Wise, D. Blaauw, and D. Sylvester. *A cubic-millimeter energy-autonomous wireless intraocular pressure*

- monitor. in *Solid-State Circuits Conference Digest of Technical Papers (ISSCC), 2011 IEEE International*. 2011.
38. P.H.L. Notten, F. Roozeboom, R.A.H. Niessen, and L. Baggetto, *3-D Integrated All-Solid-State Rechargeable Batteries*. *Advanced Materials* **19** (2007).
  39. L. Baggetto, H.C.M. Knoop, R.A.H. Niessen, W.M.M. Kessels, and P.H.L. Notten, *3D negative electrode stacks for integrated all-solid-state lithium-ion microbatteries*. *Journal of Materials Chemistry* **20** (2010) 3703-3708.
  40. J.W. Long, B. Dunn, D.R. Rolison, and H.S. White, *Three-dimensional battery architectures*. *Chem Rev* **104** (2004) 4463-92.
  41. J.F.M. Oudenhoven, L. Baggetto, and P.H.L. Notten, *All-Solid-State Lithium-Ion Microbatteries: A Review of Various Three-Dimensional Concepts*. *Advanced Energy Materials* **1** (2011) 10-33.
  42. S. Ferrari, M. Loveridge, S.D. Beattie, M. Jahn, R.J. Dashwood, and R. Bhagat, *Latest advances in the manufacturing of 3D rechargeable lithium microbatteries*. *Journal of Power Sources* **286** (2015) 25-46.
  43. M. Roberts, P. Johns, J. Owen, D. Brandell, K. Edstrom, G. El Enany, C. Guery, D. Golodnitsky, M. Lacey, C. Lecoeur, H. Mazar, E. Peled, E. Perre, M.M. Shaijumon, P. Simon, and P.-L. Taberna, *3D lithium ion batteries-from fundamentals to fabrication*. *Journal of Materials Chemistry* **21** (2011) 9876-9890.
  44. H.L. Ning, J.H. Pikul, R.Y. Zhang, X.J. Li, S. Xu, J.J. Wang, J.A. Rogers, W.P. King, and P.V. Braun, *Holographic patterning of high-performance on-chip 3D lithium-ion microbatteries*. *Proceedings of the National Academy of Sciences of the United States of America* **112** (2015) 6573-6578.
  45. G. Kim, S. Jeong, J.-H. Shin, J. Cho, and H. Lee, *3D Amorphous Silicon on Nanopillar Copper Electrodes as Anodes for High-Rate Lithium-Ion Batteries*. *ACS Nano* **8** (2014) 1907-1912.
  46. R.W. Hart, H.S. White, B. Dunn, and D.R. Rolison, *3-D Microbatteries*. *Electrochemistry Communications* **5** (2003) 120-123.
  47. N. Cirigliano, G. Sun, D. Membreno, P. Malati, C.J. Kim, and B. Dunn, *3D Architected Anodes for Lithium-Ion Microbatteries with Large Areal Capacity*. *Energy Technology* **2** (2014) 362-369.
  48. N.S. Ergang, J.C. Lytle, K.T. Lee, S.M. Oh, W.H. Smyrl, and A. Stein, *Photonic Crystal Structures as a Basis for a Three-Dimensionally Interpenetrating Electrochemical-Cell System*. *Advanced Materials* **18** (2006) 1750-1753.
  49. P.H.L. Notten, F. Roozeboom, R.A.H. Niessen, and L. Baggetto, *3-D Integrated All-Solid-State Rechargeable Batteries*. *Advanced Materials* **19** (2007) 4564-4567.
  50. W. Chunlei, J. Guangyao, L.H. Taherabadi, and M.J. Madou, *A novel method for the fabrication of high-aspect ratio C-MEMS structures*. *Journal of Microelectromechanical Systems* **14** (2005) 348-358.
  51. H.-S. Min, B.Y. Park, L. Taherabadi, C. Wang, Y. Yeh, R. Zaouk, M.J. Madou, and B. Dunn, *Fabrication and properties of a carbon/polypyrrole three-dimensional microbattery*. *Journal of Power Sources* **178** (2008) 795-800.
  52. M. Nathan, D. Golodnitsky, V. Yufit, E. Strauss, T. Rippenbein, I. Shechtman, S. Menkin, and E. Peled, *Three-dimensional thin-film Li-ion microbatteries for autonomous MEMS*. *Journal of Microelectromechanical Systems* **14** (2005) 879-885.
  53. F. Laermer and A. Urban, *Challenges, developments and applications of silicon deep reactive ion etching*. *Microelectronic Engineering* **67-8** (2003) 349-355.

54. J. Xie, P.-P.R.M.L. Harks, D. Li, L.H.J. Raijmakers, and P.H.L. Notten, *Planar and 3D deposition of  $\text{Li}_4\text{Ti}_5\text{O}_{12}$  thin film electrodes by MOCVD*. *Solid State Ionics* **287** (2016) 83-88.
55. L. Baggetto, R.A.H. Niessen, F. Roozeboom, and P.H.L. Notten, *High Energy Density All-Solid-State Batteries: A Challenging Concept Towards 3D Integration*. *Advanced Functional Materials* **18** (2008) 1057-1066.
56. G.B. Stringfellow, *Organometallic Vapor-Phase Epitaxy: Theory and Practice*, Elsevier Science (1999).
57. T.T. Kodas and M.J. Hampden-Smith, *The Chemistry of Metal CVD*, Wiley (2008).
58. A.C. Jones and P. O'Brien, *CVD of Compound Semiconductors: Precursor Synthesis, Development and Applications*, Wiley (2008).
59. M.L. Hitchman, *Farewell and Welcome*. *Chemical Vapor Deposition* **21** (2015) 213-215.
60. A. Stoffel, A. Kovács, W. Kronast, and B. Müller, *LPCVD against PECVD for micromechanical applications*. *Journal of Micromechanics and Microengineering* **6** (1996) 1.
61. E.L. Cussler, *Diffusion*, Cambridge University Press (1997).
62. K. Seshan, *Handbook of Thin Film Deposition Processes and Techniques*, Elsevier Science (2001).
63. A.C. Jones and M.L. Hitchman, *Chemical Vapour Deposition: Precursors, Processes and Applications*, Royal Society of Chemistry, Cambridge U.K. (2009).

# Chapter 2 Chemical Vapor Deposition of Lithium Phosphate

## ***Abstract***

High quality Lithium phosphate (LiPO) thin films have been deposited by LPCVD, using tert-butyllithium and trimethyl phosphate as precursors. The LiPO films deposited at 300 °C yielded the highest ionic conductivity ( $3.9 \times 10^{-8} \text{ S} \cdot \text{cm}^{-1}$ ). Increasing the deposition temperature led to crystallization of the deposited films and, consequently, to lower ionic conductivities. Kinetic studies on planar substrates showed that LiPO deposition is a diffusion-controlled process in the temperature range of 300 to 500 °C. LiPO films have also been deposited on highly structured substrates to investigate, for the first time, the feasibility of 3D deposition of LiPO by MOCVD.



## 2.1 Introduction

Driven by the fast development of autonomous devices, all-solid-state micro-batteries currently attract a lot of attention. The three dimensional (3D) all-solid-state Li-ion batteries is a challenging concept, which will significantly improve the volumetric capacity and rate capability of micro-batteries [1-3]. A stable thin film electrolyte is one of the important components for micro-batteries. Due to the relatively high Li-ion conductivity and (electro)chemical stability upon contact with Li anodes, lithium phosphate (LiPO) thin films are among the most popularly used electrolytes for micro-batteries [4-8].

Lithium phosphate based thin film electrolytes are generally deposited by sputtering [4, 5, 7, 9], pulsed laser deposition [10] and e-beam evaporation [11]. Because of shadow effects, these methods are hardly suitable for 3D deposition. In addition, during the deposition process using these methods, there is a temperature difference between the substrate and the deposited films. The resulting thermal tensile stress may disadvantageously cause film cracking [12].

Atomic layer deposition (ALD) and metal-organic chemical vapor deposition (MOCVD) are two methods that can deposit very homogeneous and conformal films on highly structured substrates. Unfortunately, the ALD method is relatively slow [13, 14] and therefore rather unpractical for the deposition of batteries materials. Several papers reported the chemical vapor deposition of nitrogen doped lithium phosphate [12, 15] but none of these papers explored the feasibility of deposition in 3D. In this study, LPCVD is investigated to deposit LiPO thin films, using tert-butyllithium (t-BuLi) and trimethyl phosphate (TMPO) as precursors. The LPCVD process for LiPO thin film deposition has been developed and the influence of the substrate temperature on the morphology, crystal structure and ionic conductivity has been systematically studied. In order to investigate the feasibility of three dimensional depositions of LiPO by LPCVD, thin films were also deposited onto highly-structured substrates. The thickness development of the deposited thin films inside these 3D-structures has been investigated.

## 2.2 Experimental details

The setup used for LiPO deposition is a horizontal cold-walled low pressure MOCVD reactor (a modified Aixtron 200RF system). The substrate was positioned on a graphite susceptor that was heated via radio frequency. The temperature was monitored using two thermocouples inside this susceptor. To increase homogeneity of the deposited films, the

sample placed on the susceptor was rotated at 10 rpm during deposition. Growth rates were regulated by the choice of reactor pressure, flow of reactants, and susceptor temperature. It was possible to vary the deposition temperature between 300 and 1000°C and the reactor pressure between atmospheric pressure and 5 mbar.

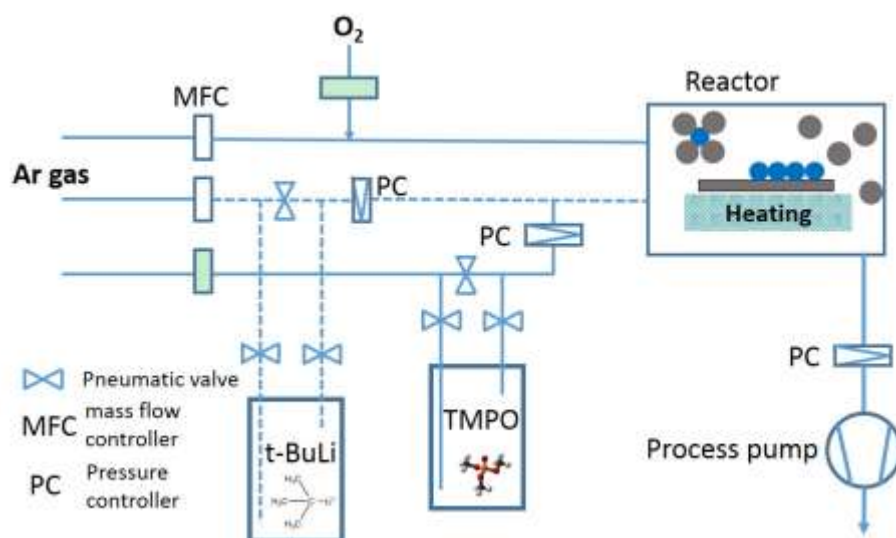


**Figure 2.1** Schematic representation of the LPCVD reactor setup.

The vapor supply system (Figure 2.1) consisted of two precursor bubblers, one of which was placed in a thermostatic bath and the other was positioned in a furnace, to control low and high temperatures, respectively. These bubblers were fed with argon to evaporate the precursors and an extra pusher flow of argon was added further downstream to increase the gas flow and to prevent condensation of the precursor in the transport lines. The precursor evaporation rate was adjusted by varying the argon flow through the bubbler as well as the pressure and temperature of the bubbler. These variables could be regulated independently for both precursors. To prevent condensation, the vapor generated at elevated temperatures (*i.e.*, from the bubbler positioned in the furnace) was led to the reactor through heated lines and valves (indicated as dashed lines in Figure 2.1). Oxygen, mixed with argon, was fed into the reactor via a system completely separated from the precursor bubblers. The oxygen and precursor gas flows were mixed in the deposition chamber.

### 2.2.1 Thin film deposition

The precursors were trimethyl phosphate (TMPO) and tert-butyllithium (t-BuLi), both acquired from SAFC-Hitech (United Kingdom). These materials were delivered in stainless steel bubblers. After the bubblers were connected, the system was tested for leaks. Argon was

supplied via a purifier to assure oxygen- and water-free gas flows. Preliminary parametric variation experiments were first carried out to find the base operating conditions, including the bubbler temperatures and carrier gas flow rates, which are listed in Table 1.1. Argon was used as carrying gas.

**Table 1.1** MOCVD process parameters for LiPO deposition.

Precursor	Temperature	Pressure	Flow
	°C	<i>mbar</i>	<i>cc/min</i>
t-BuLi	50	400	400
TMPO	20	500	40
Oxygen	Room temperature		1
Total gas flow	Room temperature		1550

LiPO layers for thickness and surface morphology analyses were deposited onto square silicon substrates with a width of 3 cm. The LiPO samples prepared for the electrochemical measurements were deposited on similar substrates covered with an adhesive layer of TiO<sub>2</sub> and a layer of platinum (Si/TiN/Pt). For the impedance measurements to be conducted after LiPO deposition, nine Pt dots with a diameter of 3 mm and thickness of 200 nm were deposited on top of the LiPO films by masked sputter deposition. To investigate the feasibility of 3D deposition, LiPO films were deposited onto silicon wafers which were reactive ion etched to obtain trenches with a width and depth of 30 μm.

### 2.2.2 Sample characterization

Thickness and morphology of the LiPO thin films were measured using a scanning electron microscope (SEM, Philips/FEI XL 40 FEG). The structural properties of the LiPO films were investigated by an X-ray diffractometer (XRD, Panalytical X'Pert PRO MPD).

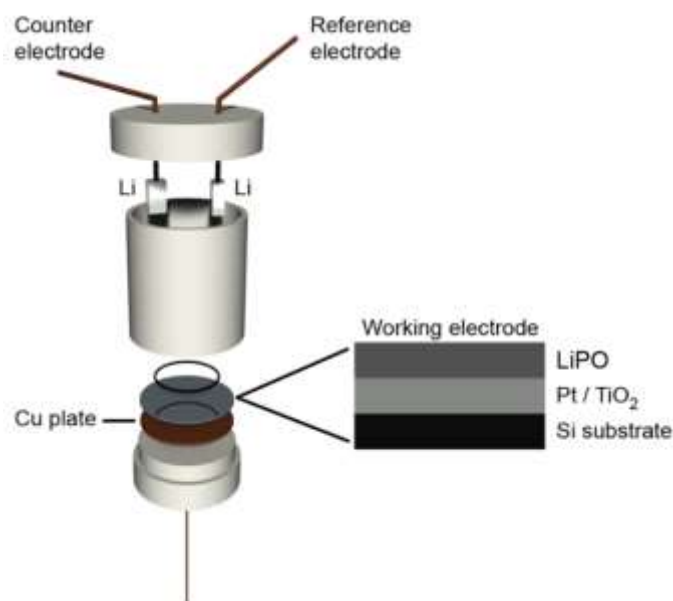


**Figure 2.2** Schematic representation of the three-electrode Teflon cell.

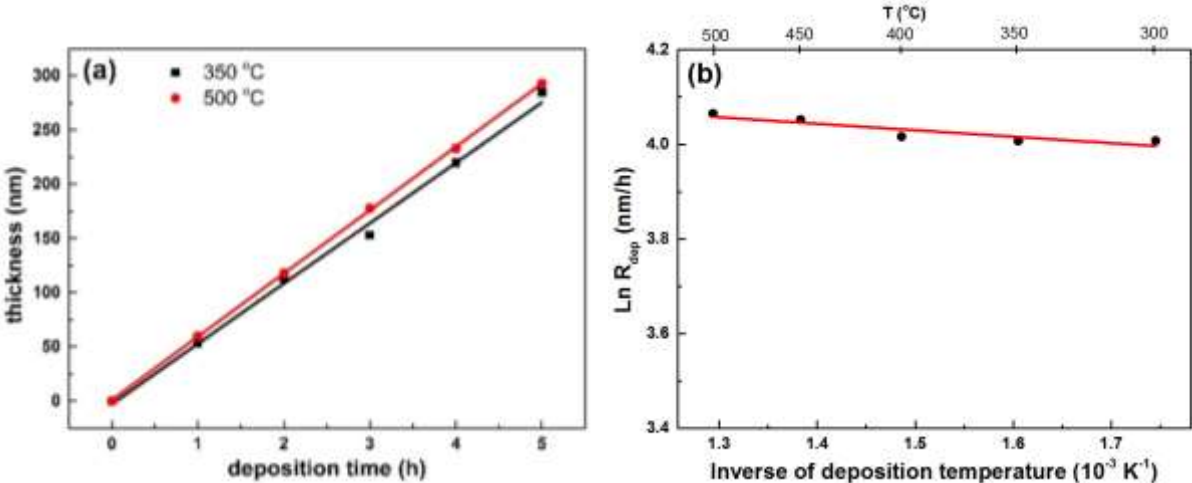
The electrochemical and impedance measurements were performed in an argon-filled glove box ( $O_2$  and  $H_2O < 1$  ppm). An Autolab PGSTAT 302 (Metrohm-Autolab B.V., The Netherlands) and a two electrodes setup were used to carry out the impedance measurements on the Pt/LiPO/Pt stacks. For potentiostatic cyclic voltammetry (CV) and galvanostatic cycling (GC) measurements, the samples were positioned in Teflon cells and used as working electrodes, as shown in Figure 2.2. Lithium metal foils were utilized as reference and counter electrodes. The cell was filled with 1 M  $LiClO_4$  in propylene carbonate (Soulbrain MI, United States). This three-electrodes setup was connected to an Autolab to perform cyclic voltammetry or a M2300 galvanostat (Maccor, Tulsa, USA) to perform galvanostatic (dis)charging. Cyclic voltammetry was executed at 1 mV/s and all potentials are given *vs* the  $Li/Li^+$  reference electrode. All electrochemical tests were carried out at room temperature.

### 2.3 Kinetic investigation

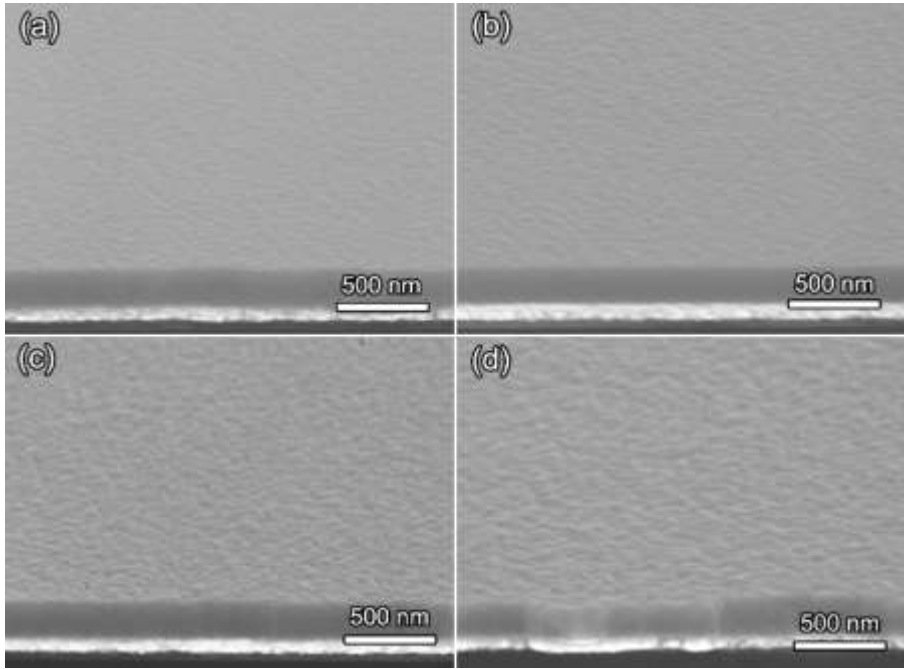
As a start, the film samples are first deposited on planar substrates to optimize the deposition process. The growth rate and morphology of the deposited films are investigated.

Figure 2.3a shows the deposited film thickness as a function of deposition time. The film thickness increases linearly with deposition time, indicating that the deposition rate is constant during the deposition process at 350 and 500 °C, which makes controlling the film thickness straightforward. The slopes of the two lines are almost equal. This suggests that the deposition

temperature does not have a clear influence on the growth rate of LiPO thin films, which is further confirmed by the Arrhenius plot, shown in Figure 2.3b. In the entire temperature range (300 - 500 °C), the deposition rate is only weakly dependent on the deposition temperature. The activation energy calculated from Figure 2.3b is 1.14 kJ/mole, which is very low. Consequently, the MOCVD deposition of LiPO is considered to be diffusion-controlled in the studied deposition temperature range.



**Figure 2.3** Deposited film thickness as a function of deposition time at 350 °C and 500 °C (a) and Arrhenius plot for the deposition rate of LiPO films (b).



**Figure 2.4** SEM images of LiPO thin films deposited at different temperatures 300 °C (a), 350 °C (b), 400 °C (c) and 450 °C (d).

Figure 2.4 shows the morphology of the thin films deposited at different temperatures. The MOCVD deposited LiPO films are very homogeneous, without revealing any cracks or pinholes. Looking into more detail, it can be concluded that the surface becomes somewhat rougher with increasing deposition temperature. It appears that the LiPO films deposited at higher temperatures are polycrystalline, forming grain boundaries. To confirm this, grazing incidence XRD was conducted.

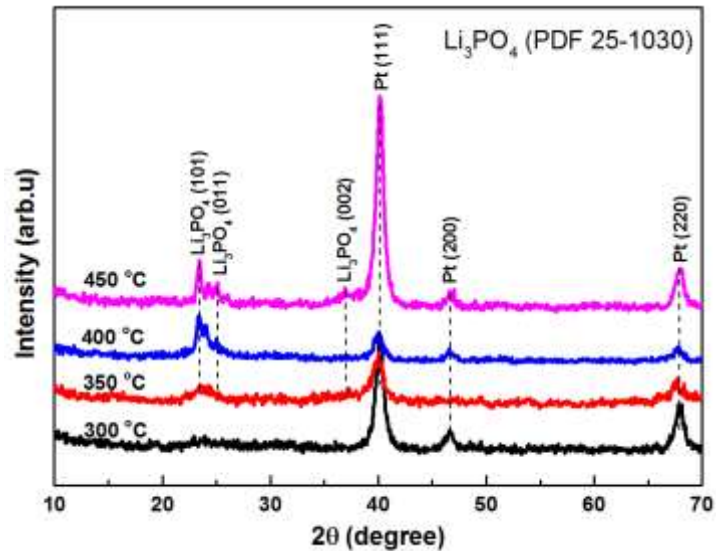


**Figure 2.5** XRD patterns of LiPO films deposited at 300, 350, 400 and 450 °C.

Figure 2.5 shows the XRD patterns of LiPO films deposited at different temperatures. The XRD pattern of the films deposited at 300 °C (black curve) shows no clear reflections, except for the Pt peaks originating from the substrate. The XRD diffraction pattern of the films deposited at 350 °C (red curve) shows a bump at around  $2\theta = 24^\circ$ , where two strong reflections of LiPO (PDF 25-1030), (101) and (011), are located. This indicates that at 350 °C, the deposited LiPO film is partially crystallized, but the crystal structure is not well developed. Another reason might be that the formed LiPO particles are very small, which give rise to broad reflections. For the films deposited at higher temperatures, characteristic peaks of LiPO can be observed. Further increase of the deposition temperature to 450 °C (magenta curve) makes the LiPO films more crystalline. Another peak assigned to LiPO (002) appears in this diffractogram at  $2\theta = 37^\circ$ . The XRD results confirm that the LiPO deposited at lower temperatures is amorphous and becomes (partially) crystalline at higher deposition temperatures, which is consistent with the morphology development observed in the SEM images shown in Figure 2.4.

## 2.4 Ionic conductivity

Ionic conductivity is one of the most important properties of solid-state electrolytes. Electrochemical impedance spectroscopy (EIS) was used to determine the ionic conductivity of the deposited LiPO thin films. The ionic conductivity ( $\sigma$ ) is calculated according to

$$\sigma = \frac{d}{A \times R}, \quad (\text{Eq. 2.1})$$

where  $d$  is the thickness of the lithium phosphate film,  $A$  is the area of the electrode, and  $R$  is the resistance which is evaluated by measuring the diameter of a semi-circle in the measured impedance spectra.

As shown in Figure 2.6, the film deposited at 300 °C has the highest ionic conductivity of  $3.9 \times 10^{-8} \text{ S}\cdot\text{cm}^{-1}$ , which is well within the range of reported values [4, 5]. When the deposition temperature is set at 350 °C, the ionic conductivity dramatically drops. At a deposition temperature of 400 °C, the ionic conductivity stabilizes at around  $3 \times 10^{-9} \text{ S}\cdot\text{cm}^{-1}$ . Further increasing the deposition temperature to 450 °C only slightly affects the ionic conductivity. It is well known that amorphous LiPO has a better ionic conductivity than the crystallized form. As discussed above, the film deposited at 400 °C is crystalline and the film surfaces become rough. So, the decrease in ionic conductivity at higher deposition temperatures is likely to be due to the crystallization of the films.

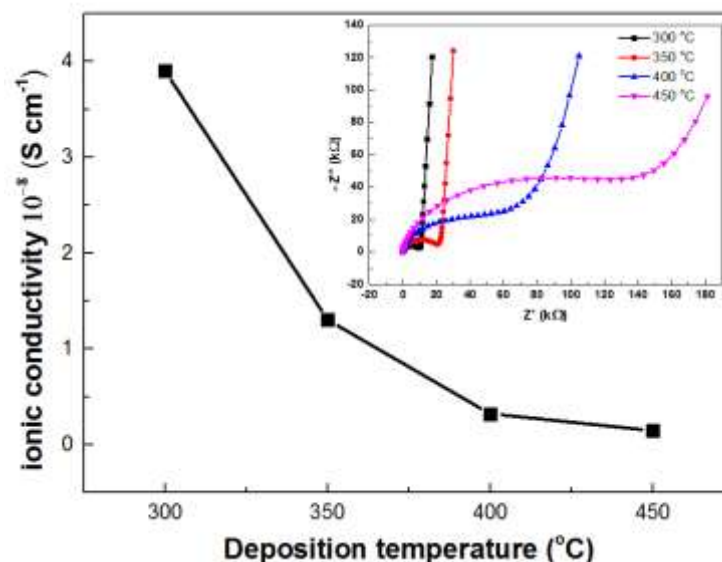


**Figure 2.6** Ionic conductivity of LiPO films as a function of deposition temperatures. The inset shows the corresponding impedance plots.

The inset of Figure 2.6 shows the corresponding EIS plots as a function of deposition temperature. It is worthwhile to note that at higher temperatures, *i.e.* at 400 and 450 °C, semicircles are more depressed. Considering the rough surface and crystallized structure, grain boundaries are likely to have formed, which will introduce additional resistance and capacitor effects [16]. Thus, it is likely that grain boundaries explain the more complex impedance characteristics of LiPO films deposited at higher temperatures.

## 2.5 Stability window

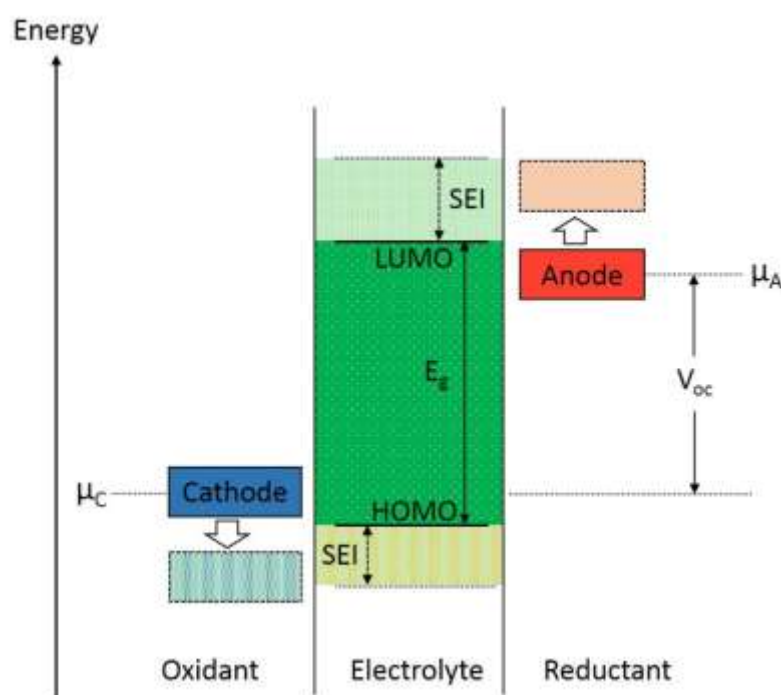


**Figure 2.7** Schematic open-circuit energy diagram of a liquid electrolyte.  $E_g$  is the window of the electrolyte for thermodynamic stability.

The energy separation  $E_g$  of the lowest unoccupied molecular orbital (LUMO) and the highest occupied molecular orbital (HOMO) of the electrolyte is the “stability window” of the electrolyte. For a thermodynamically stable battery, an anode with an electrochemical potential  $\mu_A$  above the LUMO will reduce the electrolyte unless a passivation layer creates a barrier to stop the electron transfer from the anode to the electrolyte LUMO. Similarly, a cathode with an electrochemical potential  $\mu_C$  below the HOMO will oxidize the electrolyte unless a passivation layer blocks electron transfer from the electrolyte HOMO to the cathode. Therefore, a thermodynamic stable battery requires that the electrode potentials  $\mu_A$  and  $\mu_C$  are located within



the stability window of the electrolyte, which constrains the open-circuit voltage  $V_{oc}$  of a battery cell to

$$eV_{oc} = \mu_A - \mu_C \leq E_g \quad (\text{Eq. 2.2})$$

where  $e$  is the electron charge. A passivating solid electrolyte interface (SEI) layer at the electrode/electrolyte interface can give a kinetic stability to a larger  $V_{oc}$  under the condition that  $eV_{oc} - E_g$  is not too large<sup>[17]</sup>. Since the stability window of the electrolyte limits the choices for cathode/anode materials, and thus the open-circuit voltage of a battery, the stability window of the deposited lithium phosphate electrolyte needs to be carefully characterized.

### 2.5.1 Effect of current collectors

Initially, LiPO films were deposited on Pt current collectors. The Pt/LiPO samples were assembled into the cell described in Figure 2.2. Li metal was used as reference and counter electrode. CV scans with scan rate of 1 mV/s, voltage range between 0 - 5 V were applied to the Pt/LiPO/Li cell. Figure 2.8a shows an example for the first three cycles. Notably, at higher voltage range (2 - 5 V), the cell manifests very low currents during both the reduction and oxidation process, indicating very good stability of the deposited LiPO films. However, in the low voltage range, a negative current starts to appear and the starting voltage keeps increasing as the cycle number increases, from 0.3 V to 0.8 V. If this negative current comes from the reduction of LiPO film, then the deposited LiPO film has a limited stability window, which will not cope with Li, Si or graphite anode materials. Since Pt can alloy with Li<sup>[18]</sup>, it is likely that the observed negative current and corresponding positive current are related to the lithiation of Pt current collector.

TiN is known to be a good barrier layer, which doesn't react with lithium<sup>[19]</sup>. Beside, TiN is also electronic conductive and can therefore be applied as current collector. Thus, LiPO films are deposited on substrates covered with TiN as current collector. The CV cycles of TiN/LiPO/Li cell is shown in Figure 2.8b. For the first CV cycle (black curve), the scan started from 1.7 V. Up to 0 V, there is no significant reduction current. Comparing this result with the CV result on a Pt current collector, it can be concluded that, the negative current observed in Figure 2.8a is indeed related to the lithiation of Pt current collector. It is worthwhile to note that during the positive scan of the first CV cycle, an obvious oxidation peak appears at around 4 V. After the first CV cycle, the following two cycles are completely different from the first one, three reduction peaks and two oxidation peaks were observed. However, the CV results on Pt

substrate, as shown in Figure 2.8a, demonstrate that the LiPO film is stable between 2 - 5 V. So, the oxidation peak around 4 V is not related to the oxidation of LiPO solid electrolyte, but from the oxidation of TiN current collector. It can be concluded that the TiN current collector is stable at low voltages, but will be oxidized at high voltages (around 4 V).

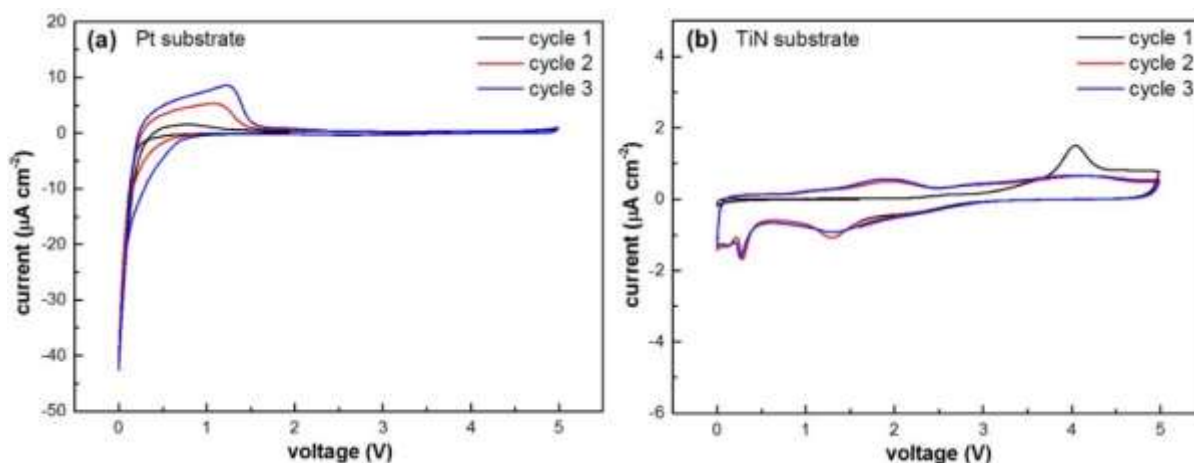


**Figure 2.8** CV scans of LiPO films deposited on substrates covered by Pt (a) and TiN (b) as current collectors, respectively. The scan rate is 1 mV/s.

## 2.5.2 Combining the CV results on Pt and TiN substrates

Based on the above discussion, neither Pt nor TiN as current collector can give a full scan in the voltage range between 0 - 5 V. So, in order to get a full view of the stability window, the CV results of LiPO films deposited on TiN and Pt substrates need to be combined. At low voltage range (0 - 1.5 V), LiPO films were deposited on TiN substrates to test the lower voltage range stability, as shown in Figure 2.9a. During the negative scan towards lower potentials, the current is very low and the current decreases with increasing cycle number. Although the negative current during the first scan is somewhat higher than the following two cycles, the reduction current is still less than  $0.5 \mu\text{A cm}^{-2}$ . This value is quite low, showing the deposited LiPO electrolyte has a good electrochemical stability at low voltages and can contact with Li or Si anodes directly.

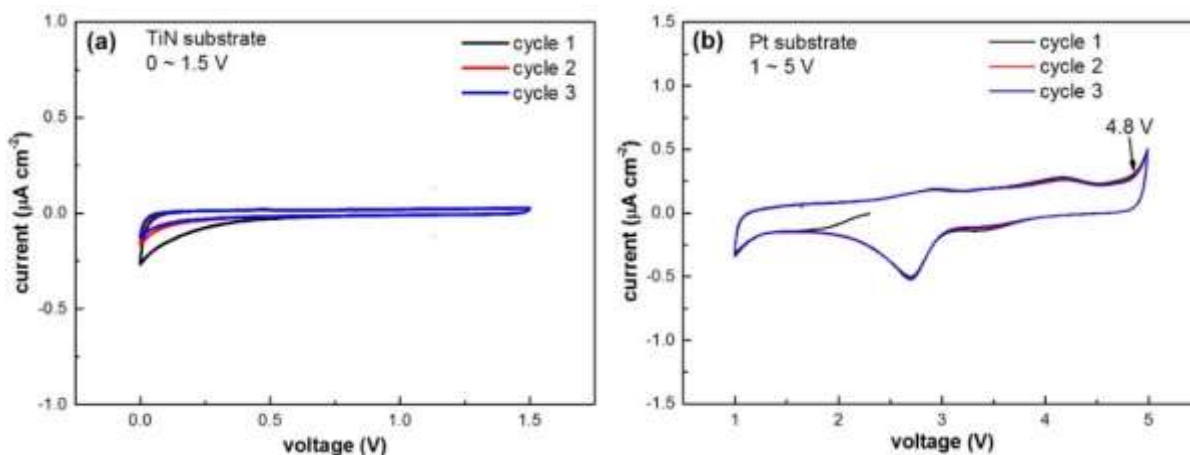


**Figure 2.9** CV scans of LiPO deposited on TiN substrate in the voltage range of -0 - 1.5 V (a) and Pt substrate in the voltage range of 1.5 - 5 V (b). The scan rate is 1 mV/s.

In the high voltage range, Pt substrates were applied. Figure 2.9b shows the CV in the range from 1 to 5 V to avoid the Li-Pt alloy formation. The current never exceeds  $1 \mu\text{A} \cdot \text{cm}^{-2}$  in this potential range. However, starting from 4.8 V, the anodic current increases rapidly, which is probably due to the oxidation of the solid electrolyte. It can therefore be concluded that the electrochemical stability of the deposited LiPO films is in a range from 0 to 4.8 V vs Li/Li<sup>+</sup>. Compared to nitrogen doped lithium phosphate (LiPON), the stability window of present MOCVD grown films is somewhat narrower but consistent with the previously reported values for LiPO films deposited by laser deposition<sup>[18]</sup> and larger than for the reported RF-sputtered films<sup>[4]</sup>. The present electrochemical stability window is, however, large enough for most of the cathode materials used in all-solid-state batteries.

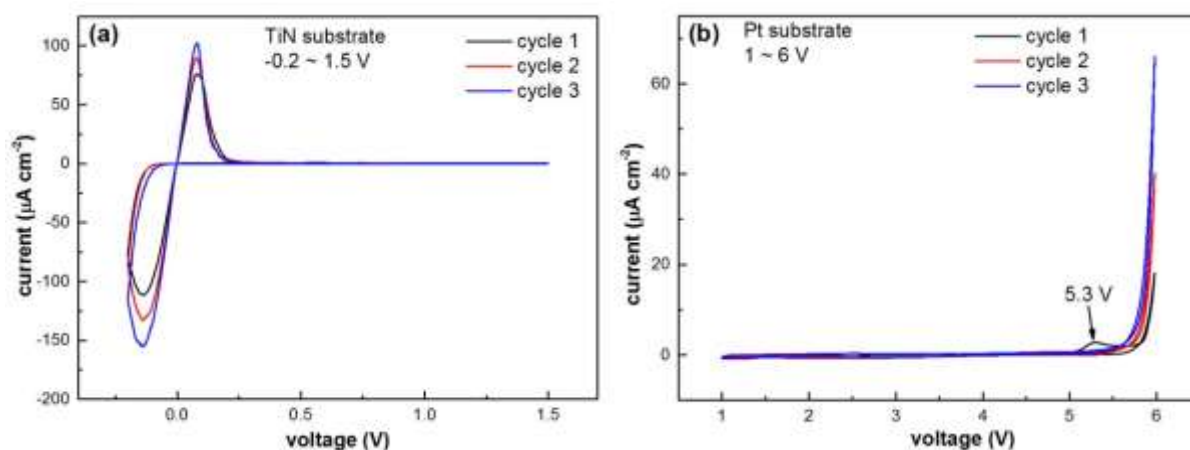


**Figure 2.10** CV scans of LiPO deposited on TiN substrate in the voltage range of -0.2 - 1.5 V (a) and Pt substrate in the voltage range of 1.5 - 6 V (b). The scan rate is 1 mV/s.

To further investigate the stability window of the deposited LiPO films, the solid electrolytes were tested in the voltage range of -0.2 - 1.5 V and 1 - 6 V. As shown in Figure 2.10a, up to 60 mV, there is still no significant reduction current, revealing good low voltage stability of the deposited LiPO film. Further decreasing the voltage, the reduction current increases fast, which is attributed to the deposition of metallic Li. Correspondingly, an oxidation peak around 80 mV appears, which is related to the stripping of the deposited Li film. Above 0.27 V, the current decreases to very low values, further confirming that the deposited LiPO electrolyte is stable in direct contact with metallic Li, which is a major advantage compared to other solid electrolytes, such as sulfide-based glassy electrolytes<sup>[20]</sup>. In the high voltage range, the cutoff voltage was increased from 5 V to 6 V. As indicated in Figure 2.10b, the LiPO electrolyte starts to be obviously oxidized at 5.3 V and oxidation becomes severe at 6 V. Notably, although there is very high oxidation current during the positive scan, no obvious reduction current is observed. This indicates that the oxidation of LiPO from 5.3 to 6 V is irreversible.

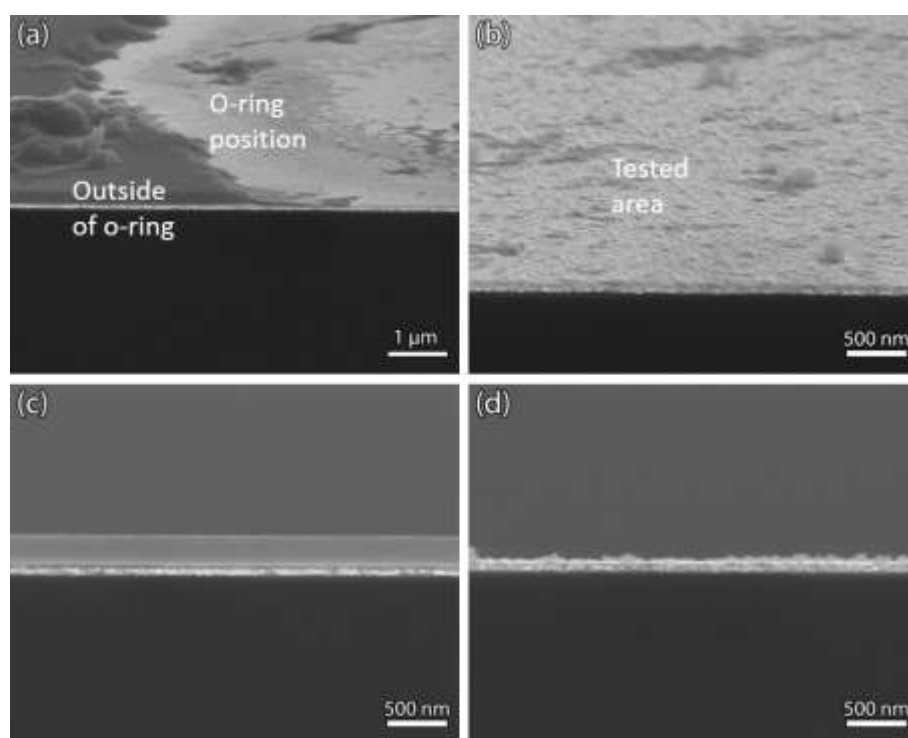


**Figure 2.11** SEM images of Pt/LiPO/Li electrode after CV scans between 1 - 6 V. Tilt view of the cleaned wafer at the O-ring position (a) and inside of the O-ring (b); cross-section view of the area outside of O-ring (c) and inside of the O-ring (d). The LiPO film inside the O-ring contacted with liquid electrolyte and was electrochemically tested.

After the CV test in the high voltage range (1 - 6 V), the Pt/LiPO sample was cleaned by propylene carbonate and dimethyl carbonate. Then, the cleaned wafer was split for cross-sectional observations. Figure 2.11a and c show the surface and cross-section views of LiPO film outside of the O-ring, which was not involved in the CV test. Notably, the deposited film is very homogeneous and attached well to the Pt current collector. However, as shown in Figure 2.11b and d, after scanning at high voltage, the deposited LiPO film was completely decomposed, only the Pt current collector was left. This is consistent with CV result. Between 5 - 6 V, the high voltage oxidized the LiPO solid electrolyte and this process is irreversible. In conclusion, for the stability of the LiPO electrolyte, the batteries must not be overcharged above 4.8 V.

## 2.6 3D deposition of LiPO

The volumetric storage capacity and rate capability are key properties for micro-batteries. Batteries with a three dimensional design would significantly improve the storage capacity due to the enlarged surface area <sup>[1]</sup>. In addition, compared to planar microbatteries, the geometric current density of 3D batteries can be significantly lower because of the enlarged surface area, thereby dramatically improve the rate capability. The key issue of making structured microbatteries is, however, the homogeneous deposition of the various batteries components in 3D. To investigate this possibility for the present solid-state electrolyte, LiPO has been deposited on 3D substrates and the uniformity of the deposited films has been investigated. The used 3D substrates consisted of silicon with etched trenches. Both the depth and width of the trenches are 30  $\mu\text{m}$  as shown in Figure 2.12a.

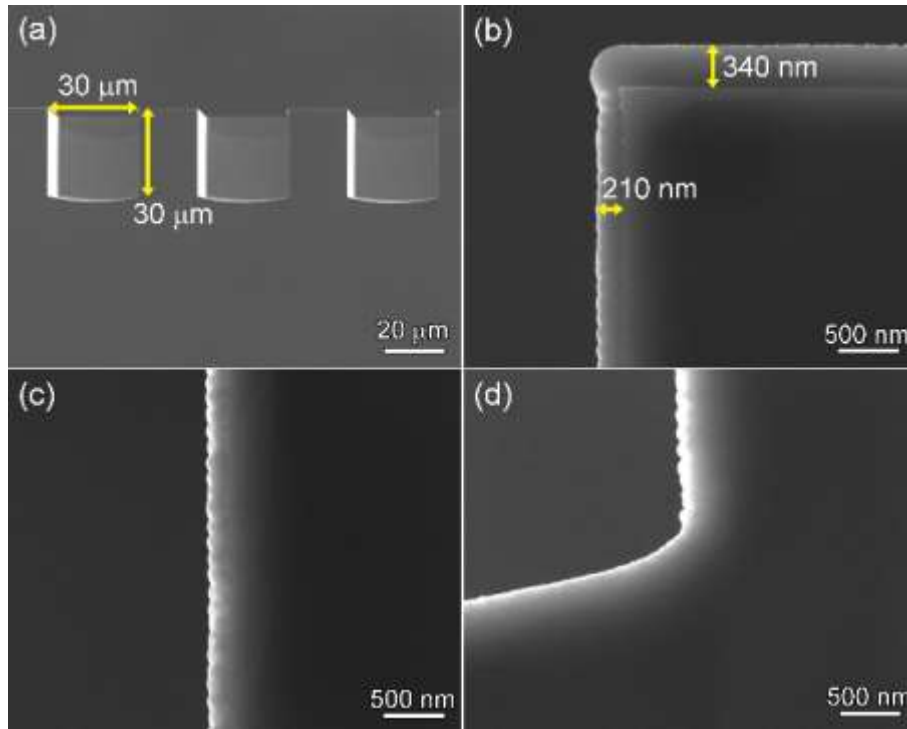


**Figure 2.12** LiPO thin film morphology deposited at 300 °C for 6 h inside a 30 μm wide trench (a) and at higher magnification at the top (b), the center (c) and bottom (d).

Although in the entire deposition temperature range, there is no significant difference in growth rate of LiPO, the lowest deposition temperature (300 °C) was chosen, based on the good electrochemical performance of these films. As shown in Figure 2.12b, the thickness of the LiPO film at the top surface is continuous and homogeneous with a thickness of 340 nm. However, the film thickness quickly decreases to 210 nm just 1 μm away from the top-corner, which indicates that the deposition process is strongly diffusion-controlled. Comparing Figure 2.12b and c, it becomes apparent that the film thickness decreases continuously with distance from the top surface increases. At the bottom (Figure 2.12d) the LiPO layer is no longer continuous.

Figure 2.13 shows the film thickness development as a function of depth inside the trenches. At the top surface the film thickness appears to be quite constant. There is, however, a sharp and almost instantaneous thickness drop inside the Si trench followed by a more continuous decrease. At the bottom, the film thickness is about 75 nm, which amounts to 22% of the thickness at the top surface. As the deposition of LiPO is a transport-controlled process, the growth of the film is limited by the diffusion of the mixed precursor gasses. Compared with the precursor gasses concentration at the top surface, the concentration inside the trenches decreases quickly and hence the layer thickness of the deposited LiPO films will obviously

become thinner. Based on the planar kinetic study and the 3D depositions, it can be concluded that using t-BuLi and TMPO as precursors under the present deposition conditions, MOCVD is not optimal to deposit LiPO homogeneously for 3D micro-batteries.

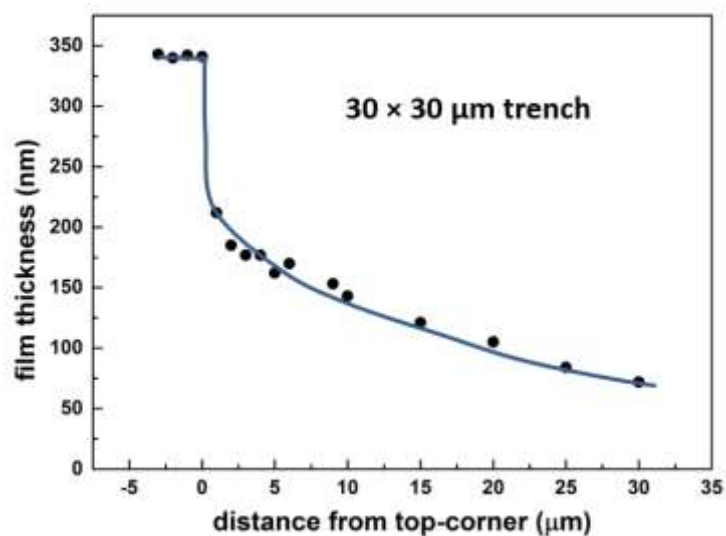


**Figure 2.13** The development of the LiPO film thickness as a function of distance from the top surface.

## 2.7 Conclusions

Lithium phosphate thin-film solid-state electrolytes were successfully deposited by MOCVD. The LiPO film deposited at 300 °C shows the highest ionic conductivity of  $3.9 \times 10^{-8} \text{ S} \cdot \text{cm}^{-1}$ . As the deposition temperature increases, the surface morphology of the deposited films becomes more rough. XRD results show that LiPO starts to crystallize when the deposition temperature increases beyond 350 °C. The ionic conductivity of these films quickly decreases to lower values when the deposition temperature increases. Pt current collectors are stable at high voltages, but alloy with Li at around 0.8 V. On the other hand, TiN current collectors are stable at low voltage ranges, but starts to decompose when the voltage is higher than 4 V. By combining the CV results of LiPO film deposited on the Pt and TiN current collectors together, a full investigation of the stability window of LiPO electrolyte has been achieved, which is between -0.27 - 4.8 V. A kinetic deposition study on planar substrates indicates that the growth of LiPO films is a diffusion-controlled process. This is confirmed by investigating the thickness development of the deposited thin films inside 3D-structures. For the 3D deposition in trenched substrates, the uniformity of deposited LiPO film was limited.

## References

1. P.H.L. Notten, F. Roozeboom, R.A.H. Niessen, and L. Baggetto, *3-D integrated all-solid-state rechargeable batteries*. *Advanced Materials* **19** (2007) 4564-4567.
2. J.F.M. Oudenhoven, R.J.M. Vullers, and R. Schaijk, *A review of the present situation and future developments of micro-batteries for wireless autonomous sensor systems*. *International Journal of Energy Research* **36** (2012) 1139-1150.
3. D. Golodnitsky, M. Nathan, V. Yufit, E. Strauss, K. Freedman, L. Burstein, A. Gladkich, and E. Peled, *Progress in three-dimensional (3D) Li-ion microbatteries*. *Solid State Ionics* **177** (2006) 2811-2819.
4. X.H. Yu, J.B. Bates, G.E. Jellison, and F.X. Hart, *A stable thin-film lithium electrolyte: Lithium phosphorus oxynitride*. *Journal of the Electrochemical Society* **144** (1997) 524-532.
5. J.B. Bates, N.J. Dudney, G.R. Gruzalski, R.A. Zuhr, A. Choudhury, C.F. Luck, and J.D. Robertson, *Electrical-Properties of Amorphous Lithium Electrolyte Thin-Films*. *Solid State Ionics* **53** (1992) 647-654.
6. P. Viet Phong, P. Brigitte, and C. Frédéric Le, *High-Performance All-Solid-State Cells Fabricated With Silicon Electrodes*. *Advanced Functional Materials* **22** (2012).
7. J.B. Bates, N.J. Dudney, G.R. Gruzalski, R.A. Zuhr, A. Choudhury, C.F. Luck, and J.D. Robertson, *Fabrication and Characterization of Amorphous Lithium Electrolyte Thin-Films and Rechargeable Thin-Film Batteries*. *Journal of Power Sources* **43** (1993) 103-110.
8. J. Li, C. Ma, M. Chi, C. Liang, and N.J. Dudney, *Solid Electrolyte: the Key for High-Voltage Lithium Batteries*. *Advanced Energy Materials* (2014) n/a-n/a.
9. H.Y. Park, S.C. Nam, Y.C. Lim, K.G. Choi, K.C. Lee, G.B. Park, S.R. Lee, H.P. Kim, and S.B. Cho, *Effects of sputtering pressure on the characteristics of lithium ion conductive lithium phosphorous oxynitride thin film*. *Journal of Electroceramics* **17** (2006) 1023-1030.
10. N. Kuwata, N. Iwagami, Y. Tanji, Y. Matsuda, and J. Kawamura, *Characterization of Thin-Film Lithium Batteries with Stable Thin-Film Li<sub>3</sub>PO<sub>4</sub> Solid Electrolytes Fabricated by ArF Excimer Laser Deposition*. *Journal of the Electrochemical Society* **157** (2010) A521-A527.
11. W.Y. Liu, Z.W. Fu, C.L. Li, and Q.Z. Qin, *Lithium phosphorus oxynitride thin film fabricated by a nitrogen plasma-assisted deposition of E-beam reaction evaporation*. *Electrochemical and Solid State Letters* **7** (2004) J36-J40.
12. L. Meda and E.E. Maxie, *Lipon thin films grown by plasma-enhanced metalorganic chemical vapor deposition in a N<sub>2</sub>-H<sub>2</sub>-Ar gas mixture*. *Thin Solid Films* **520** (2012) 1799-1803.
13. J. Hamalainen, J. Holopainen, F. Munnik, T. Hatanpaa, M. Heikkila, M. Ritala, and M. Leskela, *Lithium Phosphate Thin Films Grown by Atomic Layer Deposition*. *Journal of the Electrochemical Society* **159** (2012) A259-A263.
14. B.Q. Wang, J. Liu, Q. Sun, R.Y. Li, T.K. Sham, and X.L. Sun, *Atomic layer deposition of lithium phosphates as solid-state electrolytes for all-solid-state microbatteries*. *Nanotechnology* **25** (2014) 8.
15. H.T. Kim, T. Mun, C. Park, S.W. Jin, and H.Y. Park, *Characteristics of lithium phosphorous oxynitride thin films deposited by metal-organic chemical vapor deposition technique*. *Journal of Power Sources* **244** (2013) 641-645.
16. J.T.S. Irvine, D.C. Sinclair, and A.R. West, *Electroceramics: Characterization by Impedance Spectroscopy*. *Advanced Materials* **2** (1990) 132-138.



17. B.G. John and K. Youngsik, *Challenges for Rechargeable Li Batteries †*. Chemistry of Materials **22** (2010).
18. N. Kuwata, N. Iwagami, Y. Tanji, Y. Matsuda, and J. Kawamura, *Characterization of Thin-Film Lithium Batteries with Stable Thin-Film  $\text{Li}_3\text{PO}_4$  Solid Electrolytes Fabricated by ArF Excimer Laser Deposition*. Journal of The Electrochemical Society **157** (2010) A521.
19. H.C.M. Knoops, L. Baggetto, E. Langereis, M.C.M.v.d. Sanden, J.H. Klootwijk, F. Roozeboom, R.A.H. Niessen, P.H.L. Notten, and W.M.M. Kessels, *Deposition of TiN and TaN by Remote Plasma ALD for Cu and Li Diffusion Barrier Applications*. Journal of The Electrochemical Society (2008).
20. P. Knauth, *Inorganic solid Li ion conductors: An overview*. Solid State Ionics **180** (2009) 911-916.

## Chapter 3 Silicon Anode Materials for Microbatteries

### ***Abstract***

The electrochemical performances of Si anodes with various morphologies, such as nanowires, honeycomb structures, planar thin films and 3D-film structure, are reviewed. The initial crystal structure has a strong influence on the electrochemical performance of Si film anodes. Higher charging cutoff voltage increases (dis)charge capacity, but compromises cycle life and columbic efficiency. The normalized voltage-capacity curves show that the capacity decay of unprotected Si is mainly attributed to active material loss. To suppress the SEI formation and improve cycle stability of Si anode, a thin film of lithium phosphate (LiPO) was deposited as protecting layer on top of Si film anodes. LiPO film with a thickness of only 200 nm fully suppresses the SEI formation and dramatically improves the cycle life of Si thin film electrodes. The coulombic efficiency of the LiPO-protected Si anode is higher than 99.98%. Up to almost 500 cycles, hardly any capacity loss can be observed. The SEM images of LiPO-protected Si anodes after cycling test manifest that there is no SEI formation and the Si film anode is intact.

### 3.1 Introduction

In modern society, numerous wireless autonomous devices are used to control our working and living environment, making people's life more comfortable. In order to increase occupant comfort, intelligent and cooperative sensor networks are employed in so-called smart buildings. In a typical building, with 1 ~ 10 sensor nodes per room, one can expect thousands of sensors to be installed<sup>[1]</sup>. Another example of autonomous devices is medical implants used to stimulate nerves and muscles and to deliver drugs *in vivo* by miniaturized electronic pills<sup>[2]</sup>. Characteristic for small autonomous devices is the need for wireless operation, implying that on-board electricity storage is essential. Electricity can be stored effectively in either capacitors or batteries. Generally, the energy density of batteries is four orders of magnitude higher than that of capacitors. Considering the limited volume of the autonomous devices and avoiding hazardous liquid electrolytes, all-solid-state lithium batteries emerged as interesting power sources for these devices.

Unfortunately, the energy density of existing planar all-solid-state batteries is rather low considering the energy demand of many autonomous devices. These planar systems are based on metallic Li serving as anode with N-doped lithium phosphate (LiPON) serving as solid-state electrolyte<sup>[3]</sup>. The use of the extremely reactive metallic Li requires an expensive packaging technology. Moreover, pure lithium has a low melting point of 181°C, a temperature lower than the soldering temperature usually applied in the electronic industry. Therefore, it would be advantageous to make use of the more stable, so-called intercalation materials, which can store Li safely inside the electrodes during the operation of the batteries, resulting in Li-free structures. Si is a good option, since it has the highest theoretical specific capacity and fast reaction kinetics. In addition, several new concepts have been proposed based on 3D-batteries, making use of the combined effect of intercalation materials and surface area enlargement<sup>[4]</sup>. One of these methods exploits modern IC-technology and makes use of the excellent storage capabilities of Si thin film anodes as will be highlighted in this overview.

### 3.2 Si anodes with different morphology

Silicon is an attractive negative electrode candidate as it offers interesting properties with respect to reversible Li-ion alloying, *i.e.* very high volumetric energy density (more than 8300 mAh·cm<sup>-3</sup>), as well as fast charge transfer kinetics and Li-ion diffusion, resulting in very high rate capabilities<sup>[5, 6]</sup>. Moreover, Si improves the processing and operation safety of lithium

batteries compared to metallic Li. Si electrodes with different morphologies, prepared by various methods, have been vastly investigated [7-9]. In this chapter, the main focus is on Si nanowires, Si honeycombs and Si thin films.

### 3.2.1 Si nanowires

Si nanowire electrodes were directly grown on the desired current collector substrate by vapor-liquid-solid (VLS) growth method [10]. The small diameter of the nanowires allows for better accommodation of the large volume changes without initiation of fractures that can occur in bulk or micro-sized materials [11]. Moreover, each nanowire is electrically connected to the metallic current collector. Thus, all nanowires contribute to the storage capacity independently. Furthermore, as every nanowire is connected to the current-carrying electrode, the need for binders or conducting additives, which add extra weight, is eliminated.

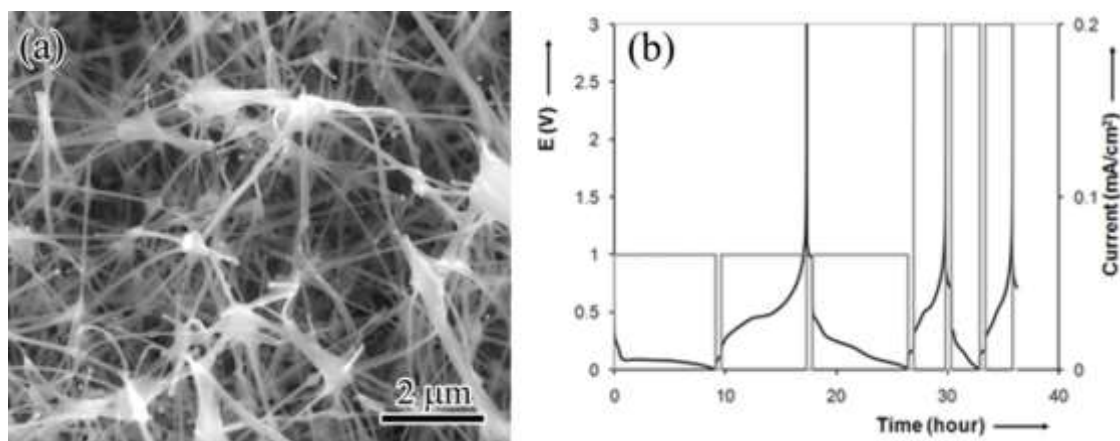


**Figure 3.1** (a) SEM images of as-prepared Si nanowires onto a TiN-covered Si substrate, (b) Charge and discharge cycles of a Si-nanowire electrode, first with a constant current of about C/10 rate and subsequently with C/3 rate.

As shown in Figure 3.1a, the nanowires, with average length of 5  $\mu\text{m}$ , do not exhibit a preferential growth orientation. Moreover, it is clear that the diameter of the wires varies from one wire to another and some wires agglomerate. Figure 3.1b exhibits the potential profiles of Si nanowires during charge and discharge. It is found that even at very low discharging rate (C/10), Si nanowires only partially crystallized into  $\text{Li}_{15}\text{Si}_4$ , as evidenced by the narrow plateau around 0.45 V during charge (delithiation). If the discharge current was set to a higher value (C/3), the plateau during charge is absent, which clearly indicates that the formation of  $\text{Li}_{15}\text{Si}_4$  is suppressed. Although the dimensions of nanowires are sufficiently large to allow long range ordering (LRO) formation of cubic  $\text{Li}_{15}\text{Si}_4$  (unit cell of about 1 nm), only partial crystallization was observed at low current. From these results, it is clear that the Li-ion (de)insertion reaction

has poor kinetics, as also suggested by the results reported earlier <sup>[11]</sup>. The poor kinetics of Si nanowire electrodes probably result from the combination of a high electrical resistance and a poor wetting of the nanowires by the liquid electrolyte.

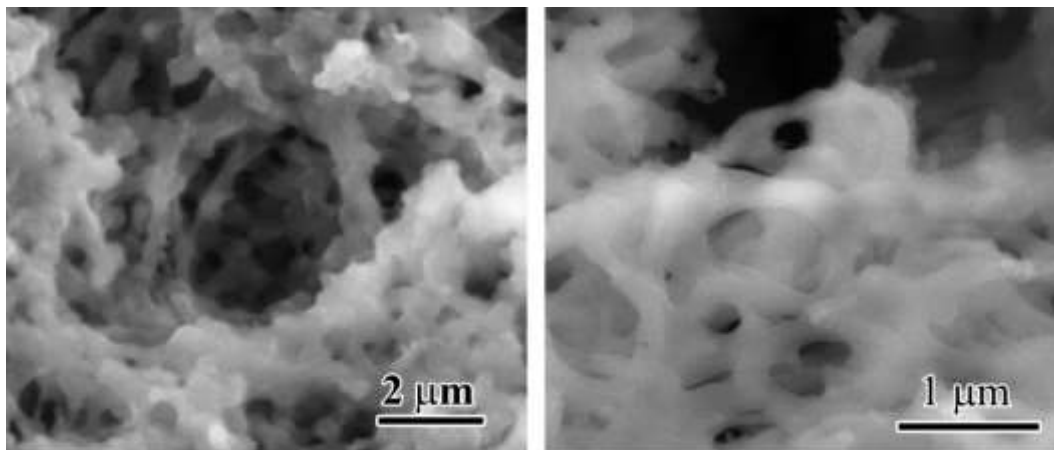


**Figure 3.2** SEM images of fully lithiated Si-nanowires. Two locations are shown with different magnifications.

The morphology of fully lithiated Si-nanowires after cycling is shown in Figure 3.2. It is clear that the diameter of the fully lithiated nanowires is larger than that of the as-prepared material, as expected from the large volume expansion occurring during lithiation. In addition, large voids are present between areas where wires have agglomerated, forming islands of interconnected nanowires. This change in morphology is caused by the expansion/shrinkage occurring during repeated cycling. Obviously, the agglomeration of the nanowires is not ideal as it can lead to local densification of the material and deprivation in adjacent areas, as observed on a larger scale during SEM inspection. Under this circumstance, the adhesion to the substrate might therefore not be sufficient to withhold the active materials which attach to the current collector after prolonged cycling.

### 3.2.2 Si honeycombs

Honeycombs, adopted as an optimum structure in, for instance, beehives were first reported in the literature in 1947 as an element of aeronautic sandwich structures, showing excellent mechanical properties <sup>[12]</sup>. In our laboratory, Si honeycombs with micro- and nanometer-sized dimensions were produced by means of photolithography and etching, and were evaluated as negative electrode materials for Li-ion microbatteries <sup>[13]</sup>.

As-prepared Si honeycombs supported on planar TiN covered Si substrates were inspected with SEM and are shown in Figure 3.3a. These honeycombs have typical dimensions of 250 nm

wall thickness, 1.1  $\mu\text{m}$  height and 4.8  $\mu\text{m}$  wall-to-wall spacing. The walls intersect into so-called triple points. The distance between the closest triple points is 2.9  $\mu\text{m}$ . Hence, it can be calculated that the surface coverage of these honeycombs is only about 10 % of the geometric footprint area. As the honeycomb height is about 1.1  $\mu\text{m}$ , this honeycomb structure is equivalent to a thickness of about 110 nm of planar Si. Since Si can absorb up to 3.75 Li or 8303  $\text{mAh}\cdot\text{cm}^{-3}$  of starting material <sup>[5]</sup>, a reversible electrochemical storage capacity of approximately 90  $\mu\text{Ah}\cdot\text{cm}^{-2}$  is expected. At full lithiation, the Si honeycombs adopt a remarkable morphology change, as presented in Figure 3.3b. Strikingly, fully lithiated honeycombs become highly curved. The original hexagonal structure adopted a shape with opposite parallel walls bending to the same direction. The triple points, however, keep their original positions and the distance between the nearest neighbors is still 2.9  $\mu\text{m}$  (the original structure is indicated by the dashed line for reference). However, the wall thickness, the curved wall length and the height have all increased considerably in comparison with the starting material.

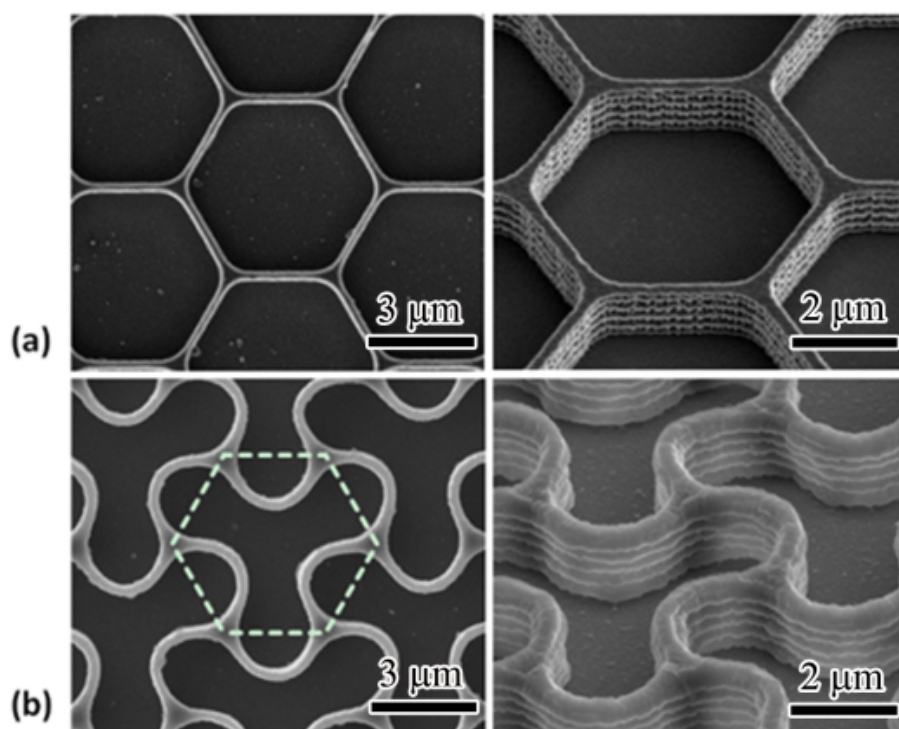


**Figure 3.3** SEM top and tilted view photographs of (a) as-prepared and (b) fully lithiated silicon honeycombs. The dashed line indicates the original honeycomb structure before lithiation at the same magnification <sup>[13]</sup>.

The initial electrochemical voltage profile of a Si honeycomb electrode is presented in Figure 3.4. The initial Li-ion insertion curve clearly shows a transformation plateau around 250 mV, which is different from Poly-Si (110 mV). Since the starting material is amorphous

hydrogenated Si ( $\alpha$ -Si:H), the plateau at 250 mV could be related to the formation of LiH<sup>[14, 15]</sup>. Beside this plateau, the rest of the discharge (a) and the subsequent charge (Li-ion extraction) curves are similar to those of amorphous Si and are characterized by two sloping regions<sup>[9]</sup>. The storage capacity of these Si honeycombs is close to that expected, however, it is somewhat low for practical use. In order to increase the storage capacity, a denser structure should be designed. This can be achieved by increasing the wall thickness/length ratio and the honeycomb height.

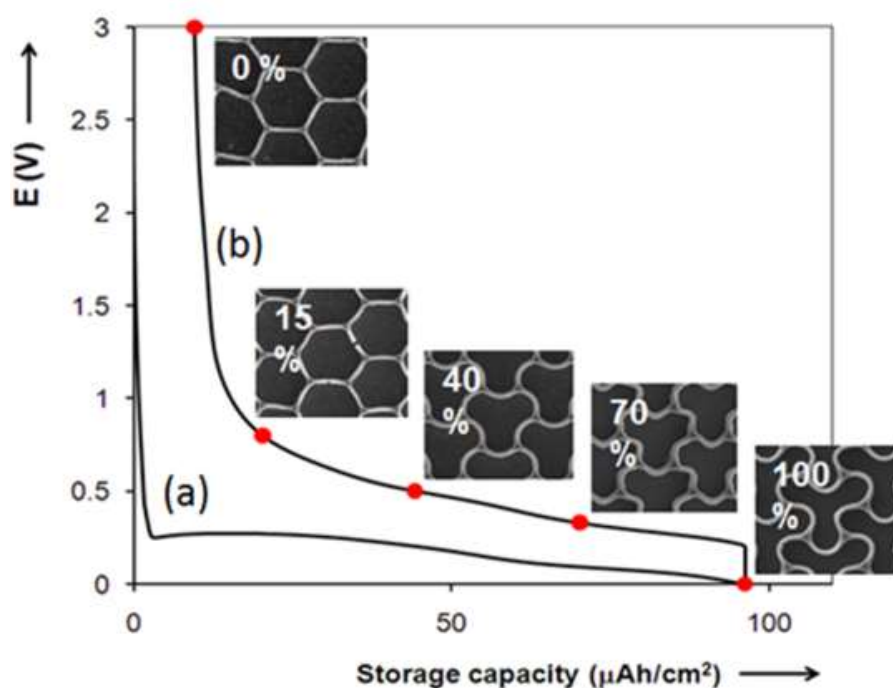


**Figure 3.4** Morphological changes of the Si honeycomb structure as a function of Li content. The main plot presents the potential profile for Si honeycombs upon (a) lithiation and (b) delithiation measured at  $75 \mu\text{A}\cdot\text{cm}^{-2}$  during the first cycle. The SEM photographs are inserted<sup>[13]</sup>.

In order to investigate the morphological changes of the honeycomb structure, fully lithiated electrodes were delithiated to various Li contents and inspected by SEM after dismantling the electrodes. The corresponding photographs, shown as inserts in Figure 3.4, clearly reveal that the mechanical deformation of the honeycombs is remarkably reversible: the highly curved structure gradually converts back to the original hexagonal structure upon delithiation. However, after repeated cycling, triple points of the Si honeycombs will detach from the current collector. As a result, the Si honeycombs are only capable of retaining a stable capacity close to the expected value for about 30–50 cycles, after which the storage capacity decreases.

### 3.2.3 Si thin films

It is well known that the volume expansion of a Si electrode induced by Li-ion insertion can be as high as about 380%. This expansion brings high compressive stress, which results in severe degradation of bulk silicon<sup>[16]</sup>. Si thin films, on the other hand, are able to accommodate this stress much better and maintain their mechanical integrity<sup>[17-19]</sup>. The electrochemical properties of nominally 50 nm thick Poly-Si electrodes deposited on top of 70 nm thick TiN barrier layers have been studied. The optical micrograph (Figure 3.5a) shows a typical patterned Poly-Si layer on top of a Si substrate that is fully covered with a TiN barrier. The patterning procedure is performed in order to accurately control the amount of active material. Typically, a 50 nm Si layer with this configuration is equivalent to an active mass of 19 mg. Figure 3.5b and c shows SEM cross-section views of such a stack.

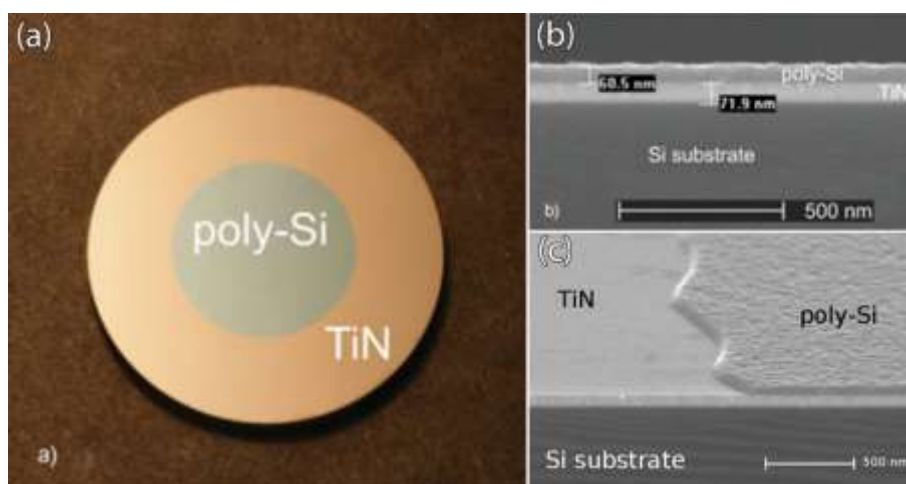


**Figure 3.5** Optical photograph (a) and SEM cross-section (b) and tilt view (c) of a LPCVD-deposited poly-Si thin film anode.

#### 3.2.3.1 Investigation of lithiation process

Si film can be deposited by sputtering<sup>[17, 20]</sup>, LPCVD<sup>[21]</sup> and Electron Beam Physical Vapor Deposition (EBPVD)<sup>[22]</sup>, *etc.* Due to the high deposition temperature, the LPCVD Si is crystallized, denoted as c-Si. While, sputtering and EBPVD are normally performed at low deposition temperature, the yielded Si films are usually amorphous, denoted as a-Si. To get an estimation of the electrochemical behavior for the Si electrodes deposited by different techniques, cyclic voltammetry (CV) measurements were conducted on LPCVD- and EBPVD-Si to identify the electrochemical responses of the lithium insertion and extraction processes. Cells using silicon thin films as working electrodes and Li metal foils as counter/reference



electrodes were subjected to potential sweeps between 0 V and 1 V vs. Li/Li<sup>+</sup> at a scan rate of 50  $\mu\text{V s}^{-1}$  for five times.

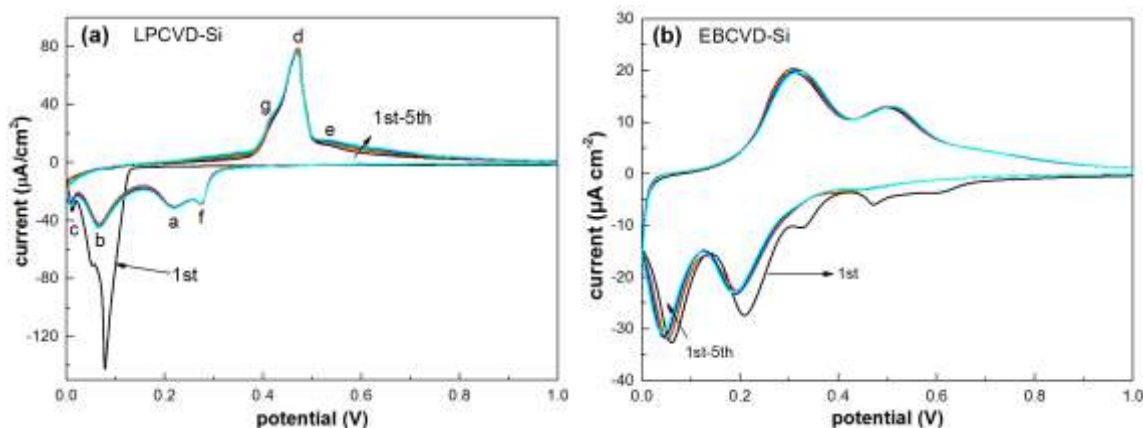


**Figure 3.6** CV scans of a LPCVD c-Si (a) and EBPVD a-Si thin film electrodes measured from 0 to 1 V for 5 times.

As shown in Figure 3.6a, during the first intercalation of poly-Si, the material transforms irreversibly into an amorphous structure [23]. This process corresponds to the sharp reduction peak at 80 mV which only exists in the first CV cycle. In the following cycles, during reduction (negative currents), the LPCVD-Si reveals two broad peaks ((a) and (b)) that correspond to transitions of Si into amorphous lithium silicides. Close to 0 V, an additional peak (c) appears that can be ascribed to the crystallization of the material into the Li<sub>15</sub>Si<sub>4</sub> cubic phase [23-25]. When extracting Li ions during oxidation, essentially one sharp peak is visible (d). This peak represents the single-step phase transition of crystalline Li<sub>15</sub>Si<sub>4</sub> into an amorphous lithium silicide of unknown composition ( $\alpha$ -Li<sub>x</sub>Si). This reaction is subsequently followed by the removal of all Li ions, peak (e) and following slope. Beside the reported reduction peaks of (a), (b) and (c), there is an additional reduction peak (f) at approximately 0.3 V. Correspondingly, an oxidation peak (g) is observed. Some other LPCVD Si samples are also tested. These abnormal reduction/oxidation peaks are reproducible. It is likely that the related redox reaction is attributed to the oxidation and reduction of SiO<sub>2</sub>. Further efforts are needed to clarify this interesting phenomenon.

The first CV cycle of EBPVD-Si is also different from the following cycles. There are several irreversible reduction peaks appearing at ~0.33, ~0.46, and ~0.61 V in the first reduction process, which have been traditionally attributed to the SEI formation on Si electrodes [26]. The onset potential of lithiation during the first negative scan is 0.3 V, corresponding to the alloying reaction of Li to form  $\alpha$ -Li<sub>2.33</sub>Si [27]. The phase transformation at ~70 mV corresponds to the

formation of  $\alpha$ -Li<sub>3.17</sub>Si. The delithiation reactions, occurring at ~0.3 and ~0.5 V corresponding to the phase transition from Li<sub>3.17</sub>Si to Li<sub>2.33</sub>Si and from Li<sub>2.33</sub>Si to LiSi, respectively. This reaction is subsequently followed by the removal of all Li ions. Different from LPCVD-Si, it is clear that EBPVD-Si does not convert into crystalline Li<sub>15</sub>Si<sub>4</sub>, since the characteristic delithiation peak of a two-phase reaction (c-Li<sub>15</sub>Si<sub>4</sub> and  $\alpha$ -Li<sub>x</sub>Si) is not observed.

It is interesting to find that the CV results of LPCVD and EBPVD-Si film anodes are different from each other, although the applied scan rate and voltage range are the same. The reason behind this different electrochemical performance is originated from the initial crystal structure of the Si anodes. The obtained amorphous Si has a totally different structure from the initial c-Si [25, 28]. The Lithiation of c-Si (LPCVD-Si) starts and progresses with bond breakage of the Si matrix from the surface by forming both lithiated isolated silicon anions and small lithiated silicon clusters until the bulk crystalline Si is consumed and total amorphization is achieved. This is followed by breakage of the remaining Si clusters to form predominantly fully lithiated isolated silicon environments (possible to nucleate a crystalline phase comprised by isolated Si ions). The mechanism for delithiation of the fully lithiated phase progresses from a small number of nuclei, growing directly to form the amorphous (delithiated) Si phase. During the second lithiation process, the amorphous silicon matrix is much more open, so the whole matrix can now be partially lithiated at higher voltages, with a much lower overpotential than that required to break the crystalline framework [29, 30].

### 3.2.3.2 Influence of cutoff voltage on cycle performance.

The cutoff voltages of discharging and charging process are important for the cycling performance of the silicon anodes. On one hand, higher cutoff voltages for charging process will extract more Li from lithiated Si anode [31]. On the other hand, it has been reported that the formed solid electrolyte interphase (SEI) may dissolve at high potentials and lose its function of protecting the underlying silicon [32]. In order to evaluate the influence of cutoff voltages on the long term cycling stability of the silicon thin film electrodes, two cutoff voltage ranges of 0 - 1.2 V and 0 - 3 V are chosen for galvanostatic cycling. The LPCVD-Si and EBPVD-Si were cycled at a constant current rate of 1 C (40  $\mu$ A·cm<sup>2</sup>) in 1 M LiClO<sub>4</sub>/PC.

Although the initial (dis-)charge capacities of the LPCVD-Si cycled in the voltage range of 0 - 3 V (denoted as Si<sub>0-3</sub>) are larger than that cycled in the voltage range of 0 - 1.2 V (denoted as Si<sub>0-1.2</sub>) during the first 20 cycles, as shown in Figure 3.7a, the capacity of Si<sub>0-3</sub> decreases

rapidly upon cycling. After 20 cycles, Si<sub>0-1.2</sub> shows higher (dis)charge capacity than Si<sub>0-3</sub> and the capacity drops slowly upon cycling. Obviously, the LPCVD-Si electrode cycled with a lower charging cutoff voltage shows a better stability. Similar to the LPCVD-Si, the capacity of the EBPVD-Si electrode cycled in the voltage range of 0 - 3 V is stable in the first 30 cycles, and then drops rapidly to 0 in the following few cycles. The electrode cycled in the voltage range of 0 - 1.2 V shows a good stability up to 40 cycles and the capacity starts to drop slowly afterwards.

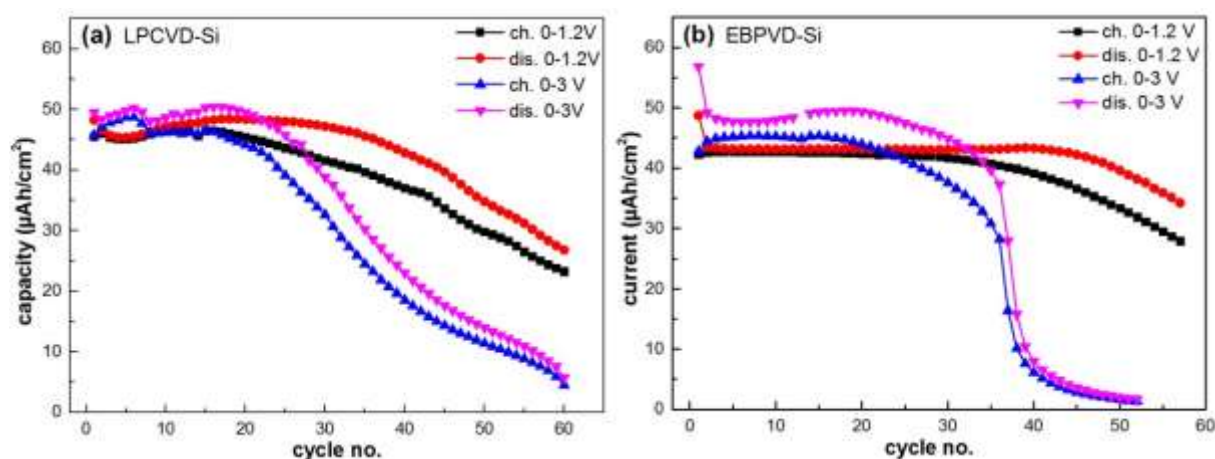


**Figure 3.7** Cycle performances of LPCVD-Si (a) and EBPVD-Si (b) cycled at different cutoff voltage ranges.

Figure 3.8 show the columbic efficiency of LPCVD-Si (a) and EBPVD-Si (b) cycled at different cutoff voltage ranges. Notably, for both Si film anodes, the samples cycled in narrower voltage window (0 - 1.2 V) always have higher columbic efficiency (CE) than that cycled in wider voltage window (0 - 3 V). This indicates that there is less irreversible reaction (mainly due to SEI formation) when the Si film anodes were cycled between 0 - 1.2 V. The likely reason is that when the Si film anodes were charged between 1.2 - 3 V, the SEI formed during discharging process was partially dissolved and can no longer effectively insulate the Si film anode anymore. So, during the next discharging process, new SEI will form again, result in more irreversible capacity loss.

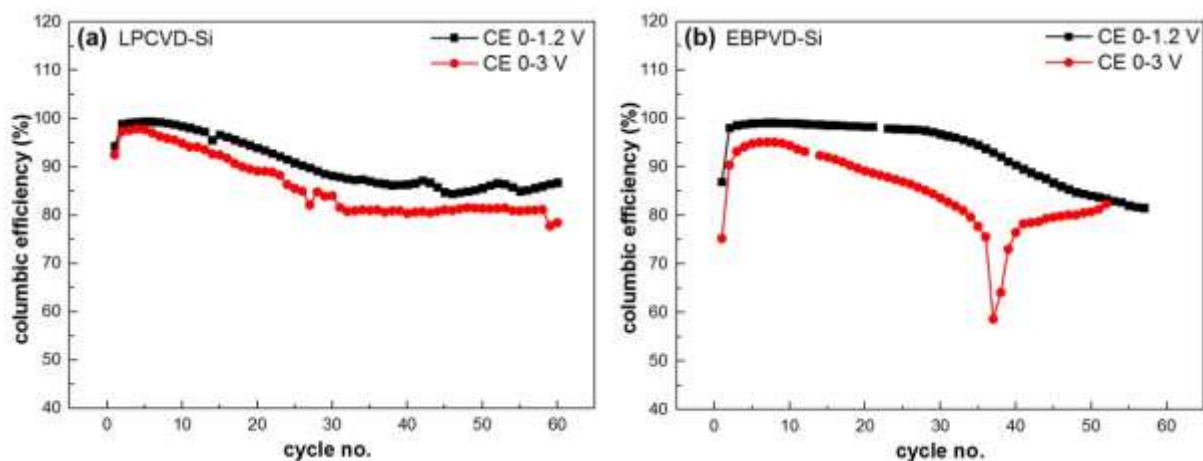


**Figure 3.8** Columbic efficiency of LPCVD-Si (a) and EBPVD-Si (b) cycled at different cutoff voltage ranges.

Based on the above discussion, it can be concluded that cycling the Si film electrodes in a wider voltage range may increase (dis)charge capacity in the beginning, but compromise the cycling stability and columbic efficiency. This phenomenon holds both for the crystallized (LPCVD-Si) and amorphous (EBPVD-Si) Si electrodes.

### 3.2.4 3D-deposited Si thin films

As a step towards achieving 3D-integrated battery prototypes, a 3D-Si electrode prepared by low pressure chemical vapor deposition (LPCVD) was deposited into porous structures (Figure 3.9). TiN deposited by atomic layer deposition (ALD) was used as barrier layer and current collector. Different locations inside the pores were inspected at higher magnifications. On the top surface, continuous films are formed. At the entrance of the pores, both TiN and Si show uniform layers. However, it is clear that Poly-Si is composed of fine crystalline grains and reveals a so-called island-like morphology. Moreover, it is evident that the thickness of both the TiN and Si layers decreases at the entrance of the pores as compared to the layer thickness on the top surface. Going deeper into the pores, the layers are thinning down and reach their minimal thickness near the bottom of the structure <sup>[21]</sup>.

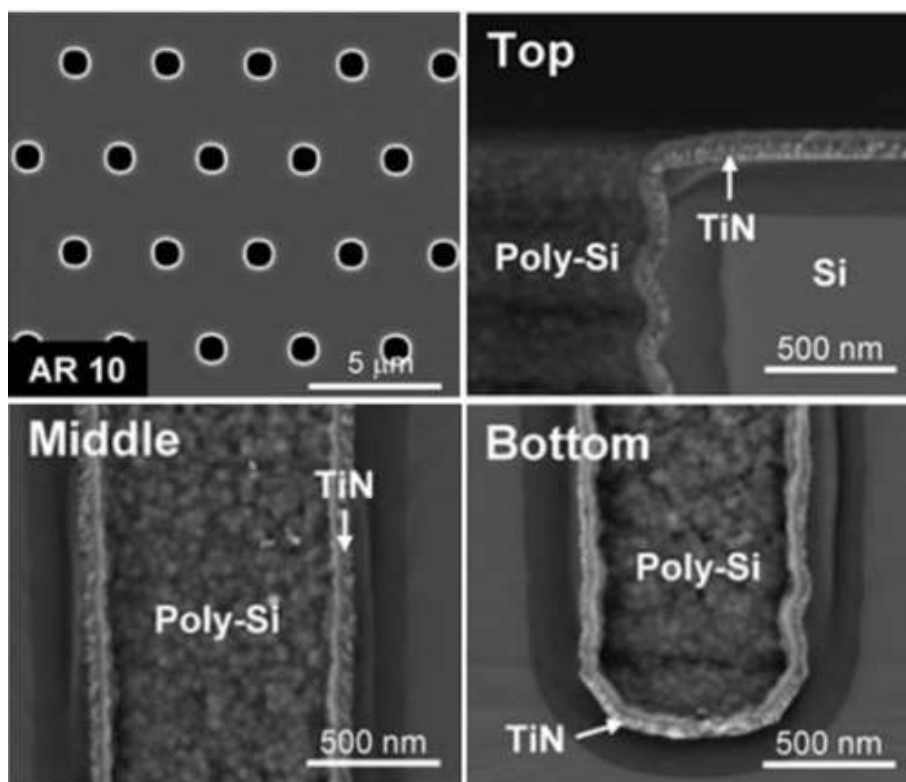


**Figure 3.9** SEM photographs of pore structure (aspect ratio 10) covered by ALD TiN and LPCVD poly-Si, showing top surface and cross-sections for different parts of a pore <sup>[21]</sup>.

The capacities measured during the first (dis)charge cycle and the expected storage capacities, as well as the corresponding capacity ratio increase, are plotted as a function of the surface area enlargement factor in Figure 3.10. The calculated storage capacities are all based on the top surface layer thickness and assuming uniform poly-Si deposition inside the pores. The measured storage capacities are approximately 30 and 40% less than expected for the aspect ratio pores of 10 and 20 at values of about 140 and 255  $\mu\text{Ah}\cdot\text{cm}^{-2}$ , respectively. Since the pores are narrower at the bottom as the depth becomes larger and the deposited Si layers inside the pores are only about 55 and 60% of the expected thickness for the aspect ratio 10 and 20 pores, respectively, this deviation in capacity is reasonable. Nevertheless, these poly-Si films deposited inside the narrow pores of aspect ratio 20 show a large increase of the storage capacity by a factor of about 5 compared to planar films.

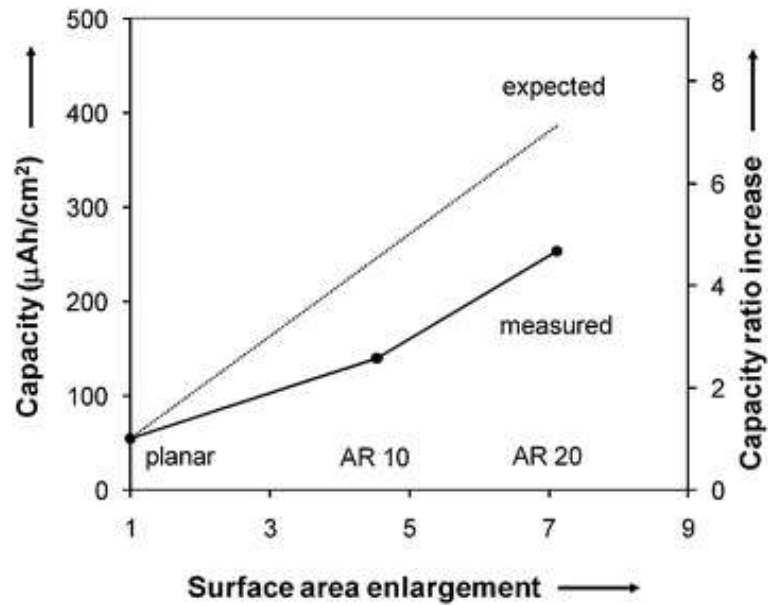


**Figure 3.10** Expected and measured reversible Li-ion storage capacities and capacity ratio increase of poly-Si thin films during the first cycle as a function of the surface area enlargement. The expected storage capacities are calculated, assuming a homogeneous layer thickness equal to the top surface layer thickness [21].

### 3.3 Protecting Si electrodes with LiPO solid electrolyte

As introduced before, silicon is a promising anode material due to its high specific and volumetric energy density [2]. Besides, silicon is also a competitive candidate to replace metallic lithium electrodes in micro-batteries, which is incompatible with reflow soldering due to its low melting point. However, the large volumetric changes induced by the (de)lithiation processes and the continuous loss and regeneration of SEI limits its practical application. Here, the LPCVD-deposited LiPO films are introduced as a protective layer to isolate the Si anode from direct contact with the liquid electrolyte.

### 3.3.1 Electrochemical tests

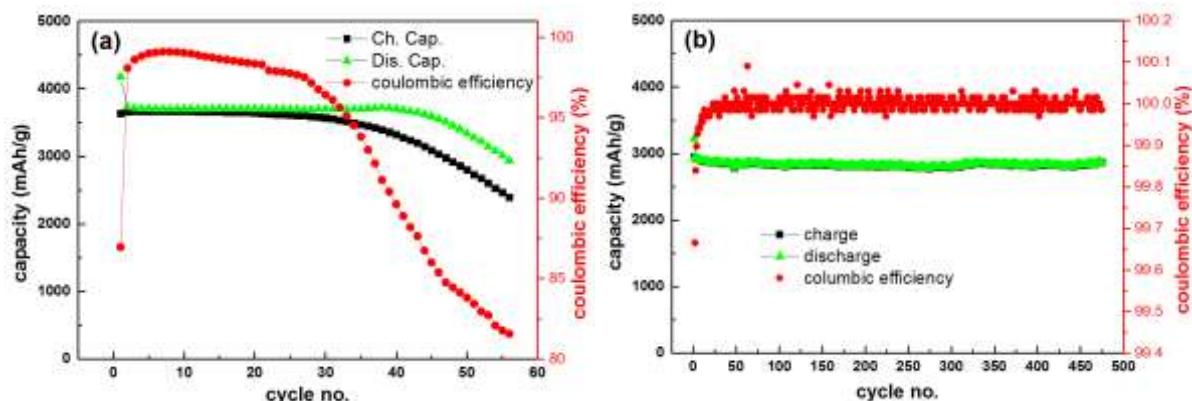


**Figure 3.11** Cycle life performance of a 50 nm thickness Si anode without (a) and with LiPO (200 nm) protection (b).

As shown in Figure 3.11a, the storage capacity of the unprotected Si anode decays very quickly. After 55 cycles, about 35% of the initial capacity has been lost and the coulombic efficiency drops to 81%. However, for the LiPO-protected Si anode hardly any capacity loss can be observed even up to almost 500 cycles (Figure 3.11b). The coulombic efficiency of LiPO-protected Si is close to 100% and is very stable after the initial activation cycles. Such a high coulombic efficiency indicates that there are almost no side reactions occurring during charging and discharging.

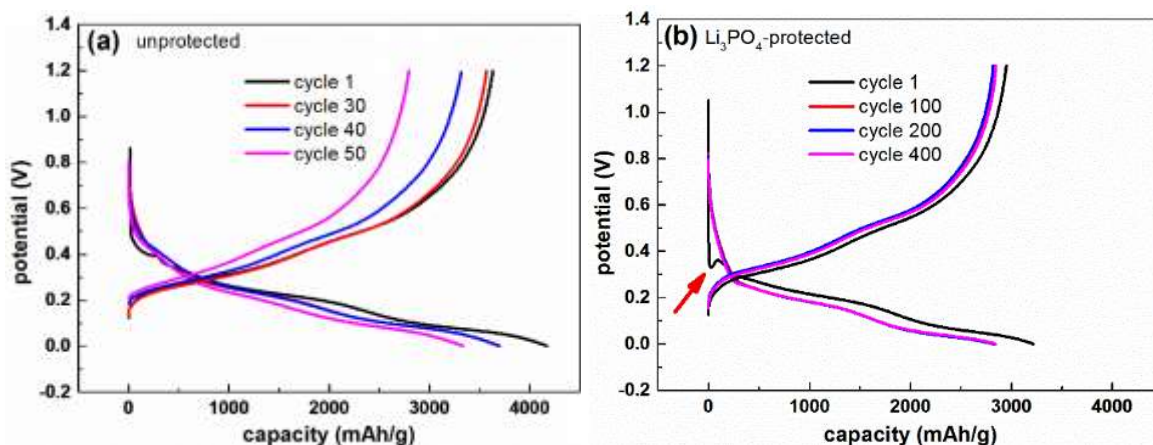


**Figure 3.12** Capacity-voltage curves of Si anodes without (a) and with LiPO protection (b).

The capacity-voltage curves of Si anodes without and with LiPO protection are shown in Figure 3.12a and b, respectively. The capacity of the Si electrode without LiPO protection quickly shifts to lower values after 30 cycles. However, for the LiPO-protected Si electrode, after 400 cycles, the capacity-voltage curve still overlaps with previous ones, indicating that the

LiPO-protected Si anode is indeed not attacked during the entire cycling performance test. It is worthwhile to note that the first cycles of both unprotected and LiPO-protected Si anodes (black curves) are somewhat different from the other cycles. For unprotected Si electrode, this deviation comes from SEI formation. For the  $\text{Li}_3\text{PO}_4$ -protected Si electrode, an additional reduction peak only appears in the first cycle (indicated by the arrow), which may be attributed to the activation of the Si/ $\text{Li}_3\text{PO}_4$  interface as has been reported before <sup>[33]</sup>.

To better understand the decay mechanism of Si film anodes, the voltage curves are normalized from 0 to 1 to exclude the effect of state-of-charge (SoC), as shown in Figure 3.13. For a discharging (lithiation) process, the storage capacity is normalized at 1 when the Si anode is at fully lithiated state. Si anode with the same normalized capacity is approximately at the same SoC. Figure 3.13a shows the voltage curves of Si anode without LiPO protection. Due to large amount of SEI formation and activation process, such as reducing the formed  $\text{SiO}_2$  on the surface, the voltage curves of the first cycle is different from the subsequent (dis)charging cycles. Except the first cycle, after normalizing the capacity, the voltage curves of cycle 30, 40 and 50 are overlapping with each other, revealing typical voltage curves of Si anodes. This indicates that Si anode doesn't transform into other kinds of materials and is still the only active material which contributes to the capacity of the cell. The decrease of capacity during cycling is mainly due to the loss of active material (Si) rather than deterioration of Si anode.

Another reason of capacity decrease is likely to be related to the actual (dis)charging current rate, which keeps increasing as the capacity decreases. From Figure 3.11, the charging capacities of unprotect Si are 3568, 3319 and 2796 mAh/g for cycle 1, cycle 30 and cycle 50, respectively. The capacity of the anode is decreasing upon cycling, but the applied (dis)charging current is constant. In this case, the actual C rates is increasing as the cycle number increases. Compared with cycle 30, the actual C rate of cycle 50 is increased 28%, to be 1.28 C. However, as shown in Figure 3.13a, the overpotential (voltage difference between charge and discharge voltage curves) of cycle 50 is only slightly higher than that of cycle 30 and cycle 1, which indicates that the increase of actually current rate doesn't have a significant influence on the overpotential of the (dis)charging processes. So, the capacity losses attributed to increase of overpotential is also negligible. Based on the above discussion, it can be concluded that the capacity decrease of unprotected Si is mainly due to active materials loss and the influence of materials transformation and overpotential increase are negligible.



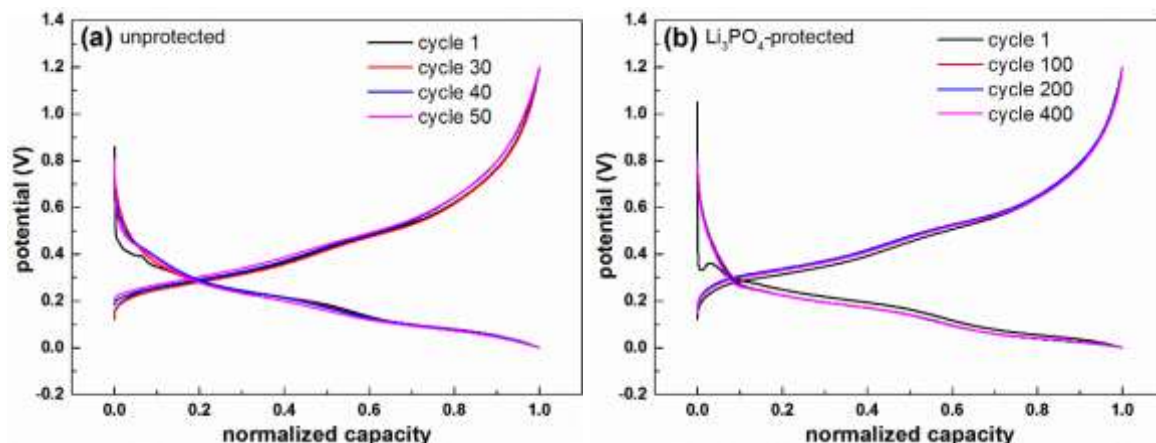


**Figure 3.13** Normalized capacity-voltage curves of Si anodes without (a) and with LiPO protection (b).

The normalized voltage curves of LiPO-protected Si is shown in Figure 3.13b, except for the first cycle, the voltage curves are perfectly overlapping with each other, indicating the electrode is very stable during the entire cycling test. Obviously, a MOCVD-deposited thin film of LiPO with a thickness of only 200 nm fully suppresses the SEI formation completely and dramatically improves the cycle life of Si thin film electrodes.

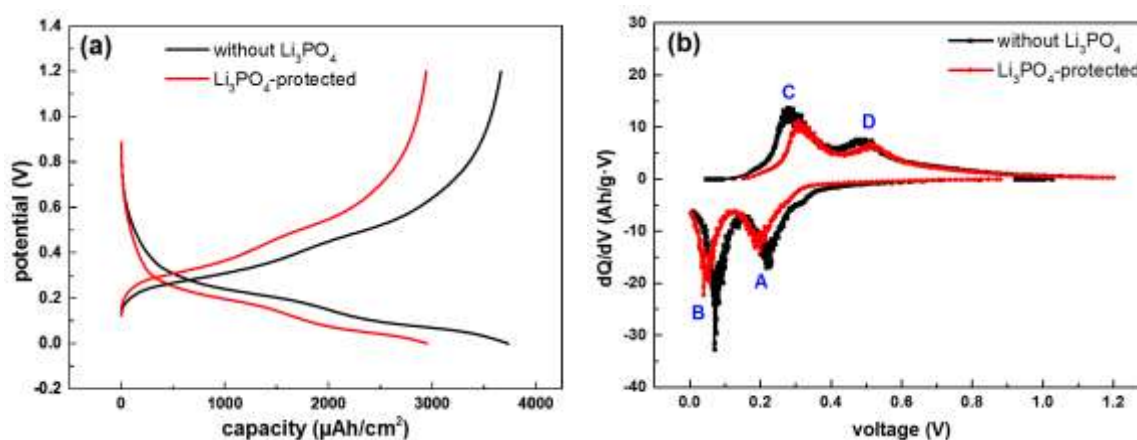


**Figure 3.14** Capacity-voltage curves (a) and derivative of storage capacity with respect to voltage curves (b) for unprotected and LiPO-protected Si electrodes at cycle 2.

Furthermore, it is interesting to note that after covering the Si electrode with a LiPO film, the initial storage capacity of the LiPO-protected Si anode is somewhat lower than that of the unprotected electrode. This may be due to the additional resistance introduced by the solid-state electrolyte. In order to investigate this influence, the capacity-voltage curves of the second (dis)charge cycle have been investigated. To avoid the influence of the SEI formation in the case of the unprotected electrode and the activation process in the case of LiPO-protected

electrode, the second cycle has been compared. Figure 3.14a shows that the overpotential for the LiPO-protected Si electrode during (dis)charging are higher than for the unprotected electrode. This is also confirmed by the derivative of storage capacity with respect to the voltage curves shown in Figure 3.14b. Two reduction peaks (A and B) are observed, which correspond to the transition of Si into amorphous lithium silicides <sup>[17]</sup>. Correspondingly, two oxidation peaks (C and D) are found during the oxidation process. Compared to the unprotected electrode, the reduction peaks of the LiPO-protected Si electrode shift to lower potentials and the oxidation peaks to higher potentials, indicating an increase of overpotential during the charge and discharge process.

Conclusively, Figure 3.14b clearly indicates that the LiPO-protected electrode reveals similar (de)lithiation processes, which are characteristic for Si anodes. But due to the additional resistance introduced by the LiPO film, the overpotentials are increased, resulting in the observed virtual capacity loss. However, given the improved cycle-life performance, such a capacity sacrifice is very acceptable, because after 50 cycles the LiPO-protected electrode actually already has a much higher storage capacity. The LiPO film thickness on the Si electrode for which the results are given in Figure 3.11b is only 200 nm, which apparently is pinhole-free and sufficient to protect the underlying Si electrode. The extraordinary performance of LiPO-protected Si thin film electrode also shows excellent mechanical and electrochemical stability of the MOCVD-deposited LiPO film.

### 3.3.2 SEM analysis after cycling test

After the cycling test, the cells are disassembled and rinsed with propylene carbonate (PC) and dimethyl carbonate (DMC) solvent. Figure 3.15a shows the top surface images of unprotected Si anode after 60 cycles. It is obvious that lots of cracks are formed that are due to the volume expansion/shrinkage during the repeatedly (dis)charging. The cracks will damage the adhesion between the Si anode and the current collector. After many cycles, the adhesion may become very weak, and some Si active materials is likely to lose contact with the current collector, becoming “dead Si”, which will not contribute to the storage capacity anymore. What’s more, the fomed cracks will be filled with liquid electrolyte and new SEI will be formed inside the cracks, which expands the size of the cracks and accelerate the capacity loss of the unprotected Si. The cross-section view of the unprotected Si film anode is shown in Figure 3.15b. A loose but thick SEI layer is formed on the surface. The TiN barrier can still be clearly observed, but the Si film becomes invisible. As discussed in section 3.3.2, as the cycling test continues, the

Si active material is gradually lost. There are two likely ways to explain this disappearance: the Si anode may form some intermediates with the SEI layer and mixed into it. Alternatively, it might be due to the peeling off of Si film from the substrate by continuous expansion and shrinkage. However, in either way, the unprotected Si is not stable during (dis)charge and the disappearance of the Si film is consistent with the observed dramatical capacity loss at the end of cycling.

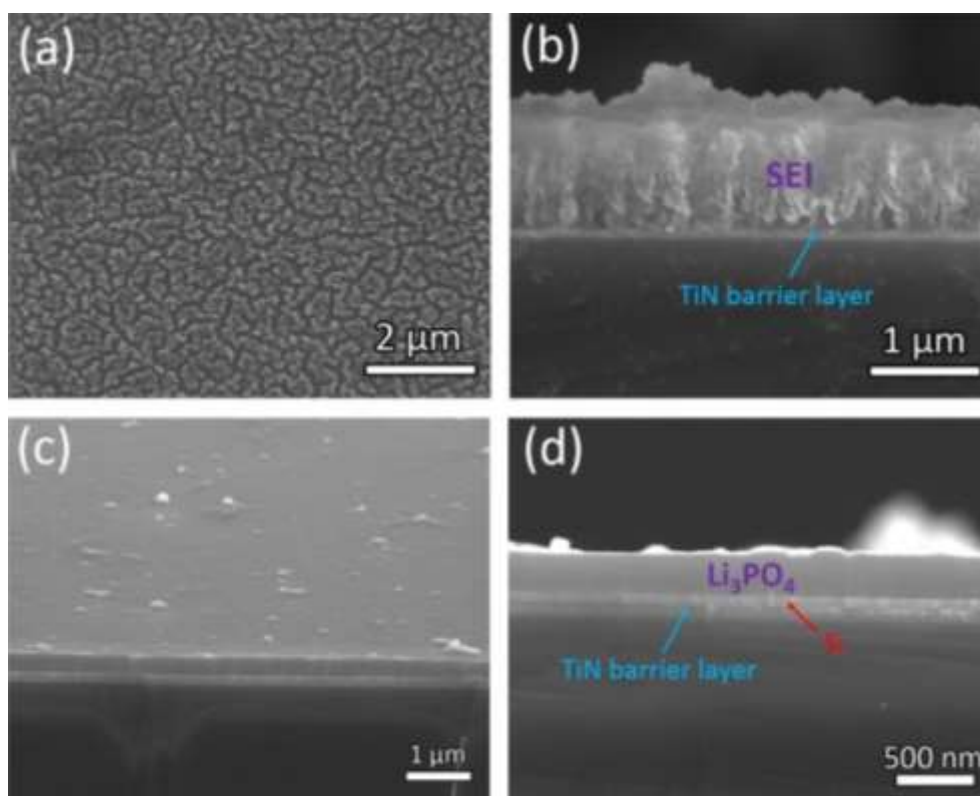


**Figure 3.15** SEM images of unprotected (a) and LiPO-protected Si film (b) after galvanostatic cycling.

In contrast, the LiPO-protected Si is intact even after almost 500 cycles, without revealing any cracks or SEI formation on the surface, as shown in Figure 3.15c and d. What's more, the layers of TiN barrier layer, Si film and LiPO can still be clearly distinguished. On one hand, the solid electrolyte, LiPO, prevents direct contact between the Si anode and liquid electrolyte. Due to the high electronic resistance of LiPO, electrons cannot pass through the solid electrolyte to reduce the liquid electrolyte. Therefore, the SEI formation is suppressed. On the other hand, due to the good adhesion between LiPO and Si layers and the good mechanical stability of the deposited LiPO films, the LiPO-protected Si electrodes mainly expand perpendicular to the surface as reported previously <sup>[34]</sup>. As a result, the LiPO film is homogeneously lifted rather than cracked and effectively protects the Si anode from being attacked by the liquid electrolyte.

### 3.4 Conclusions

Si anodes with three different morphologies are reviewed. Si nanowires tend to agglomerate upon expansion/shrinkage to form a porous network separated by voids, which is not favorable if the electrodes are repeatedly cycled for a long time. Si honeycombs can undergo very large mechanical deformation. However, detachment of small parts of the honeycomb from the current collector will happen after repeatedly cycling and only a moderate cycle life is achieved. The deposition feasibility of a highly structured negative electrode stack to be applied in future 3D-integrated batteries has been demonstrated. In comparison with planar thin films, these 3D-structured Poly-Si films present a storage capacity increase of about 5 times.

The lithiation and delithiation processes of poly-crystalline and amorphous Si thin films have been investigated. For LPCVD deposited crystalline Si,  $\text{Li}_{15}\text{Si}_4$  is formed in the end of lithiation process, followed by a strong oxidation peak during the delithiation process. In contrast, the EBPVD deposited amorphous Si cannot form  $\text{Li}_{15}\text{Si}_4$  crystalline and two oxidation peaks appear during the delithiation process. It is clear that the original crystal structure of Si films strongly influences their electrochemical performance as anode material. Higher charging cutoff voltage increases (dis)charge capacity, but compromises cycle life and columbic efficiency. For unprotected Si, the film electrode cracks into pieces due to the repeated volume expansion and shrinkage. The normalized capacity-voltage curves show that the capacity decrease of Si anodes during cycling is mainly attributed to active material losses and the influence of materials transformation and overpotential increase on the capacity loss are negligible. When very thin films of lithium phosphate are deposited onto Si films as protective layers, it was found that LiPO films effectively suppress the SEI formation and dramatically improve the cycle stability of Si electrodes. The coulombic efficiency of the LiPO-protected Si anode is higher than 99.98%. Up to almost 500 cycles, hardly any capacity loss is observed.

## References

1. J.F.M. Oudenhoven, R.J.M. Vullers, and R. Schaijk, *A review of the present situation and future developments of micro-batteries for wireless autonomous sensor systems*. International Journal of Energy Research **36** (2012) 11391150.
2. P.H.L. Notten, F. Roozeboom, R.A.H. Niessen, and L. Baggetto, *3-D Integrated All-Solid-State Rechargeable Batteries*. Advanced Materials **19** (2007) 4564-4567.
3. J.B. Bates, N.J. Dudney, D.C. Lubben, G.R. Gruzalski, B.S. Kwak, X. Yu, and R.A. Zuhr, *Thin-film rechargeable lithium batteries*. Journal of Power Sources **54** (1995) 58-62.
4. J.F.M. Oudenhoven, L. Baggetto, and P.H.L. Notten, *All-Solid-State Lithium-Ion Microbatteries: A Review of Various Three-Dimensional Concepts*. Advanced Energy Materials **1** (2011) 10-33.
5. L. Baggetto, R.A.H. Niessen, F. Roozeboom, and P.H.L. Notten, *High Energy Density All-Solid-State Batteries: A Challenging Concept Towards 3D Integration*. Advanced Functional Materials **18** (2008) 1057-1066.
6. L. Baggetto, J.F.M. Oudenhoven, T. van Dongen, J.H. Klootwijk, M. Mulder, R.A.H. Niessen, M.H.J.M. de Croon, and P.H.L. Notten, *On the electrochemistry of an anode stack for all-solid-state 3D-integrated batteries*. Journal of Power Sources **189** (2009) 402-410.
7. P. Kuiqing, J. Jiansheng, Z. Wenjun, and L. Shuit-Tong, *Silicon nanowires for rechargeable lithium-ion battery anodes*. Applied Physics Letters **93** (2008).
8. L.-F.F. Cui, Y. Yang, C.-M.M. Hsu, and Y. Cui, *Carbon-silicon core-shell nanowires as high capacity electrode for lithium ion batteries*. Nano letters **9** (2009) 3370-3374.
9. U. Kasavajjula, C. Wang, and A.J. Appleby, *Nano- and bulk-silicon-based insertion anodes for lithium-ion secondary cells*. Journal of Power Sources **163** (2007) 1003-1039.
10. R. Ruffo, S.S. Hong, C.K. Chan, R.A. Huggins, and Y. Cui, *Impedance Analysis of Silicon Nanowire Lithium Ion Battery Anodes*. The Journal of Physical Chemistry C **113** (2009) 11390-11398.
11. C.K. Chan, H. Peng, G. Liu, K. Mcllwraith, X.F. Zhang, R.A. Huggins, and Y. Cui, *High-performance lithium battery anodes using silicon nanowires*. Nat Nano **3** (2008) 31-35.
12. W.W. Troxell and H.C. Engel, *Column Characteristics of Sandwich Panels Having Honeycomb Cores*. Journal of the Aeronautical Sciences **14** (1947) 413-420.
13. L. Baggetto, D. Danilov, and P.H. Notten, *Honeycomb-structured silicon: remarkable morphological changes induced by electrochemical (de)lithiation*. Advanced Materials **23** (2011) 1563-6.
14. T.L. Kulova, A.M. Skundin, Y.V. Pleskov, E.I. Terukov, and O.I. Kon'kov, *Lithium insertion into amorphous silicon thin-film electrodes*. Journal of Electroanalytical Chemistry **600** (2007) 217-225.
15. L. Yong Min, L. Jun Young, S. Heung-Taek, L. Joong Kee, and P. Jung-Ki, *SEI Layer Formation on Amorphous Si Thin Electrode during Precycling*. Journal of The Electrochemical Society **154** (2007).
16. L.Y. Beaulieu, T.D. Hatchard, A. Bonakdarpour, M.D. Fleischauer, and J.R. Dahn, *Reaction of Li with Alloy Thin Films Studied by In Situ AFM*. Journal of The Electrochemical Society **150** (2003) A1457-A1464.
17. J.P. Maranchi, A.F. Hepp, and P.N. Kumta, *High Capacity, Reversible Silicon Thin-Film Anodes for Lithium-Ion Batteries*. Electrochemical and Solid-State Letters **6** (2003).

18. H. Jung, M. Park, S.H. Han, H. Lim, and S.-K. Joo, *Amorphous silicon thin-film negative electrode prepared by low pressure chemical vapor deposition for lithium-ion batteries*. *Solid State Communications* **125** (2003) 387-390.
19. T. Takamura, S. Ohara, M. Uehara, J. Suzuki, and K. Sekine, *A vacuum deposited Si film having a Li extraction capacity over 2000 mAh/g with a long cycle life*. *Journal of Power Sources* **129** (2004) 96-100.
20. V. Baranchugov, E. Markevich, E. Pollak, G. Salitra, and D. Aurbach, *Amorphous silicon thin films as a high capacity anodes for Li-ion batteries in ionic liquid electrolytes*. *Electrochemistry Communications* **9** (2007) 796-800.
21. L. Baggetto, H.C.M. Knoop, R.A.H. Niessen, W.M.M. Kessels, and P.H.L. Notten, *3D negative electrode stacks for integrated all-solid-state lithium-ion microbatteries*. *Journal of Materials Chemistry* **20** (2010) 3703-3708.
22. J. Yin, M. Wada, K. Yamamoto, Y. Kitano, S. Tanase, and T. Sakai, *Micrometer-Scale Amorphous Si Thin-Film Electrodes Fabricated by Electron-Beam Deposition for Li-Ion Batteries*. *Journal of The Electrochemical Society* **153** (2006) A472-A477.
23. T.D. Hatchard and J.R. Dahn, *In Situ XRD and Electrochemical Study of the Reaction of Lithium with Amorphous Silicon*. *Journal of The Electrochemical Society* **151** (2004) A838-A842.
24. M.N. Obrovac and L. Christensen, *Structural Changes in Silicon Anodes during Lithium Insertion/Extraction*. *Electrochemical and Solid-State Letters* **7** (2004) A93-A96.
25. J. Li and J.R. Dahn, *An In Situ X-Ray Diffraction Study of the Reaction of Li with Crystalline Si*. *Journal of The Electrochemical Society* **154** (2007) A156-A161.
26. H. Bryngelsson, M. Stjern Dahl, T. Gustafsson, and K. Edstrom, *How dynamic is the SEI?* *Journal of Power Sources* **174** (2007) 970-975.
27. M.K. Datta, J. Maranchi, S.J. Chung, R. Epur, K. Kadakia, P. Jampani, and P.N. Kumta, *Amorphous silicon-carbon based nano-scale thin film anode materials for lithium ion batteries*. *Electrochimica Acta* **56** (2011) 4717-4723.
28. C.K. Chan, R. Ruffo, S.S. Hong, R.A. Huggins, and Y. Cui, *Structural and electrochemical study of the reaction of lithium with silicon nanowires*. *Journal of Power Sources* **189** (2009) 34-39.
29. N. Dimov, S. Kugino, and M. Yoshio, *Carbon-coated silicon as anode material for lithium ion batteries: advantages and limitations*. *Electrochimica Acta* **48** (2003) 1579-1587.
30. B. Key, M. Morcrette, J.-M. Tarascon, and C.P. Grey, *Pair Distribution Function Analysis and Solid State NMR Studies of Silicon Electrodes for Lithium Ion Batteries: Understanding the (De)lithiation Mechanisms*. *Journal of the American Chemical Society* **133** (2011) 503-512.
31. M.N. Obrovac and L.J. Krause, *Reversible Cycling of Crystalline Silicon Powder*. *Journal of The Electrochemical Society* **154** (2007) A103-A108.
32. K. Tasaki, A. Goldberg, J.-J. Lian, M. Walker, A. Timmons, and S.J. Harris, *Solubility of Lithium Salts Formed on the Lithium-Ion Battery Negative Electrode Surface in Organic Solvents*. *Journal of The Electrochemical Society* **156** (2009) A1019-A1027.
33. L. Baggetto, R.A.H. Niessen, and P.H.L. Notten, *On the activation and charge transfer kinetics of evaporated silicon electrode/electrolyte interfaces*. *Electrochimica Acta* **54** (2009) 5937-5941.
34. P. Viet Phong, P. Brigitte, and C. Frédéric Le, *High-Performance All-Solid-State Cells Fabricated With Silicon Electrodes*. *Advanced Functional Materials* **22** (2012).



## Chapter 4 Planar and 3D Deposition of $\text{Li}_4\text{Ti}_5\text{O}_{12}$

### ***Abstract***

$\text{Li}_4\text{Ti}_5\text{O}_{12}$  is well known to be a safe and efficient anode material for Li-ion batteries. A metal-organic chemical vapor deposition process has been developed for the synthesis of  $\text{Li}_4\text{Ti}_5\text{O}_{12}$  thin film anodes on planar and 3D substrates. The influence of various deposition parameters, including precursor flow rates and post-annealing temperatures, have been investigated by material and electrochemical analyses.  $\text{Li}_4\text{Ti}_5\text{O}_{12}$  thin films deposited at the optimized process parameters showed a high crystallinity and high electrochemical activity. A reversible storage capacity of 151 mAh/g was achieved at a current of 0.5 C, corresponding to 86.3% of the theoretical specific capacity of  $\text{Li}_4\text{Ti}_5\text{O}_{12}$ . Up to almost 600 cycles, the electrodes showed no significant capacity loss. Furthermore, the deposited thin film anodes also showed excellent rate performance. Compared to the storage capacity at 0.5 C, 93% of the capacity was maintained at 10 C. Thin films were also deposited on highly structured substrates to investigate the uniformity and electrochemical performance. With the same footprint area, the 3D  $\text{Li}_4\text{Ti}_5\text{O}_{12}$  film anodes showed a 2.5 times higher storage capacity than planar electrodes.



## 4.1 Introduction

During the past decade, microelectronic mechanical systems, smart cards, on-chip power sources and portable electronic devices have become more widespread. To power these devices, all-solid-state thin film batteries are widely applied. By contrast, there have been only a few reports on the synthesis of thin film anode materials for lithium-ion batteries. Li metal is the mostly used anode material for solid micro-batteries. However, the use of extremely reactive metallic lithium anodes requires an expensive packaging technology. Moreover, pure lithium is highly volatile and melts at about 181 °C, a temperature usually lower than that applied during re-flow soldering processes, widely used in the electronic industry <sup>[1]</sup>.  $\text{Li}_4\text{Ti}_5\text{O}_{12}$  (LTO), on the other hand, is an attractive alternative anode material, which has the advantages of reliable safety characteristics, negligible volume change during cycling and no formation of a solid electrolyte interface <sup>[2, 3]</sup>.

Many techniques have been applied to synthesize LTO film anodes, including sol-gel <sup>[4, 5]</sup>, magnetron sputtering <sup>[6, 7]</sup>, spray pyrolysis <sup>[8]</sup>, aerosol <sup>[9]</sup>, and mist CVD <sup>[10]</sup>. However, all these depositions have been carried out on planar substrates and the electrochemical storage capacity of these planar film electrodes remains relatively low. To facilitate the current energy demand, the challenging concept of three-dimensional (3D) integrated all-solid-state rechargeable batteries has been proposed <sup>[11, 12]</sup>. In this way, the storage capacity of a thin film electrodes can be significantly increased without an increase of footprint area. Chemical vapor deposition has demonstrated to be a viable tool to deposit battery components for 3D micro-batteries <sup>[13, 14]</sup>.

In this work, we report the first attempt of using metal-organic chemical vapor deposition (MOCVD) to synthesize thin films of LTO as a potential anode material for micro-batteries. Furthermore, thin films were also deposited onto highly structured substrates to investigate the feasibility of 3D deposition of LTO by MOCVD. The thickness development of the deposited thin films and the electrochemical performance were investigated.

## 4.2 Experimental details

### 4.2.1 Thin film deposition

The MOCVD setup used for LTO deposition has been described in detail in chapter 2. In short, a cold wall MOCVD reactor (Aixtron 200 RF) was used, in which the substrate was positioned on a radio frequency heated susceptor. The precursors were titanium isopropoxide

(TTIP) and tert-butyllithium (t-BuLi), both acquired from SAFC-Hitech (United Kingdom). Preliminary parametric variation experiments were first carried out to find the base operating conditions, including the bubbler temperatures and carrier gas flow rates, which are listed in Table 4.1. Argon was used as carrier gas. The pressure of the reactor was 5 mbar during the deposition processes. The depositions were performed at a temperature of 500 °C for 120 min, unless stated otherwise.

**Table 4.1** Preliminary optimized MOCVD process parameters for LTO deposition.

Precursor	Temperature °C	Pressure <i>mbar</i>	Flow <i>sccm</i>
t-BuLi	50	400	100 ~ 400
TTIP	25	300	200
Oxygen	Room temperature		1 ~ 50
Total gas flow	Room temperature		1550

LTO films for thickness and surface morphology analyses were deposited onto square silicon substrates with a width of 3 cm. The LTO samples prepared for the electrochemical measurements were deposited on similar substrates covered with a barrier layer of TiN and a layer of platinum (Si/TiN/Pt) as current collector. To investigate the uniformity of 3D deposition, LTO films were deposited onto silicon wafers, which were reactive ion etched to obtain trenches with a constant depth of 30 µm and widths of 30 and 10 µm, as shown in Figure 4.12. To investigate the electrochemical performance of 3D LTO anodes, films were deposited on reactive ion etched Si pillars. The pillars were coated with TiN, which was used as current collector. The diameter and depth of the Si pillars are 2 µm and 50 µm, respectively, and the distance between pillars is 5 µm, as shown in Figure 4.14.

#### 4.2.2 Sample characterization

The structural properties of the deposited films were investigated by a grazing incidence X-ray diffractometer (XRD, Panalytical X'Pert PRO MPD) with a Cu K $\alpha$  X-ray source. The thickness and morphology of the LTO thin films were measured using a scanning electron microscope (SEM, Philips/FEI XL 40 FEG).

The electrochemical measurements were performed in an argon-filled glove box ( $O_2$  and  $H_2O < 1$  ppm). The samples were positioned in Teflon cells and used as working electrodes. Lithium metal foils were utilized as reference and counter electrodes. The cell was filled with 1 M  $LiClO_4$  in propylene carbonate (Soulbrain MI, United States). This three-electrode setup was connected to a M2300 galvanostat (Maccor, Tulsa, USA) to perform galvanostatic (dis)charging. The constant current experiments were performed at different C rates (for LTO anode, 1 C corresponds to 175 mAh/g or  $60 \mu A/cm^2 \cdot \mu m$ ). All electrochemical tests were carried out at room temperature ( $\sim 22$  °C). The mass ( $M$ ) used to calculate the gravimetric capacity is determined according to  $M = Ah\rho$ , where  $A$  is confined active surface area,  $h$  is film thickness measured by cross-section view of SEM and  $\rho$  is theoretical density of LTO ( $3.43 \text{ g/cm}^3$ ).

### 4.3 Deposition on planar substrates

The films were first deposited on planar substrates to optimize the deposition parameters, and to investigate the electrochemical performances.

#### 4.3.1 Adhesion with the Si/TiN/Pt substrate

500 °C was selected as a starting temperature to carry the depositions. When the sample was taking out from the reactor, it is noticed that some cracks were very obvious and the deposited film loosely attached with the Si/TiN/Pt substrate and can be easily wiped out. Figure 4.1a and b shows the SEM images of the deposited film. Obviously, the adhesion between the LTO film and Pt current collector is very poor and the LTO film couldn't form a dense and continuous film on the Pt substrate. To solve this problem, before the start of LTO deposition, we first deposit 10 min  $TiO_2$  as an adhesion layer. The thickness of the  $TiO_2$  adhesion layer is around 10 nm. After adding this  $TiO_2$  adhesion layer, the deposited LTO film attach very well to the substrate and homogeneous films are deposited, as shown in Figure 4.1c and d.

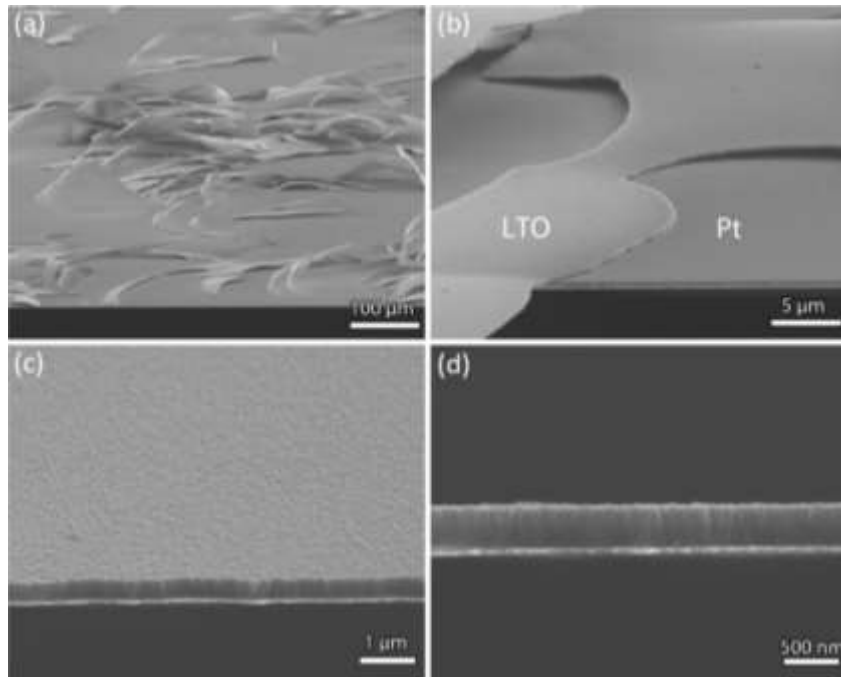


**Figure 4.1** SEM images of LTO deposited directly on Pt substrate at 500 °C (a) and (b); after adding a buffer layer of 10 nm TiO<sub>2</sub> (c) and (d).

### 4.3.2 Optimizing deposition parameters

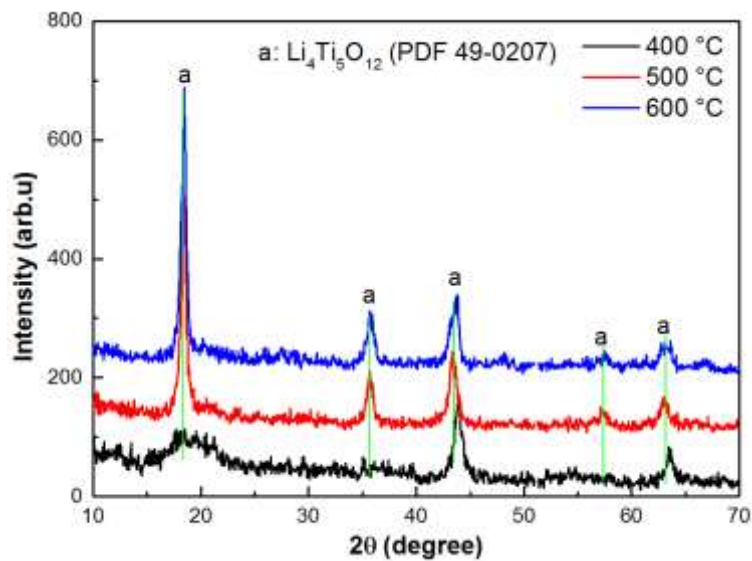


**Figure 4.2** XRD patterns of thin films deposited at different temperatures. with constant flow rates of Ti (200 sccm) and Li (400 sccm) precursors and O<sub>2</sub> flow rate of 1 sccm.

Figure 4.2 shows the XRD patterns of thin films deposited at different temperatures. At 400 °C, some characteristic peaks of LTO (PDF 49-0207) appeared, but the peak is wide and the intensity of diffraction peaks is limited, indicating the deposited film is not well crystallized.

When the deposition temperature increased to 500 and 600 °C, the deposited film generated strong and sharp diffraction peaks. Since the XRD patterns of films deposited at 500 and 600 °C are similar, it can be concluded that 500 °C is sufficient to deposit crystallized LTO films. In the following section, without any specific indication, all the depositions are carried at 500 °C.

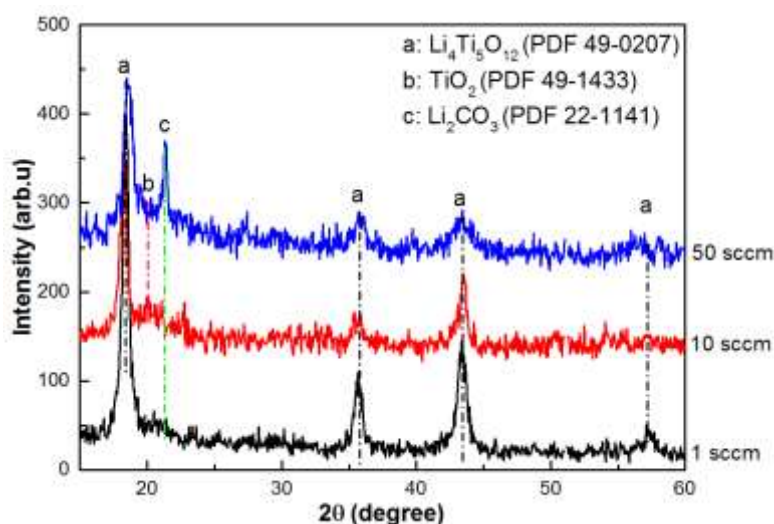
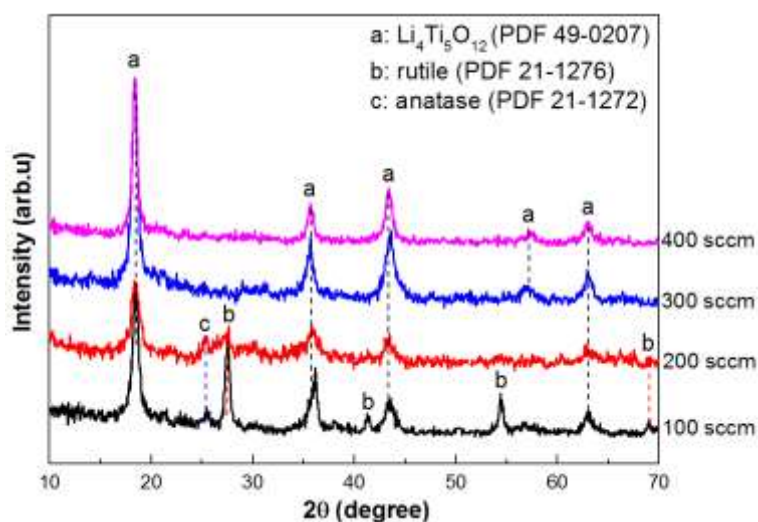


**Figure 4.3** XRD patterns of thin films deposited with constant flow rates of Ti (200 sccm) and Li (400 sccm) precursors and various indicated O<sub>2</sub> flow rates.

Figure 4.3 shows the XRD patterns of films deposited with different O<sub>2</sub> flow rates. The flow rates of the Ti and Li precursors were fixed at 200 and 400 standard cubic centimeters per minute (sccm), respectively. The film deposited with an O<sub>2</sub> flow rate of 1 sccm (black curve) shows only reflections of LTO (PDF 49-0207). This indicates that an O<sub>2</sub> flow rate of 1 sccm is sufficient to obtain phase pure LTO. Since the Ti precursor is TTIP, which could also provide oxygen atoms during the deposition process, it is reasonable that not much additional O<sub>2</sub> flow is needed to deposit LTO. The deposition with an O<sub>2</sub> flow of 10 sccm also yields pure LTO (red curve). However, when the O<sub>2</sub> flow is increased to 50 sccm (blue curve), two additional diffraction peaks appear, indicated by b and c, which can be assigned to TiO<sub>2</sub> (PDF 49-1433) and Li<sub>2</sub>CO<sub>3</sub> (PDF 22-1141), respectively. Based on these XRD results, it can be concluded that an O<sub>2</sub> flow of 1 sccm is sufficient to deposit pure LTO. The introduction of too much O<sub>2</sub> gives rise to the formation of TiO<sub>2</sub> and Li<sub>2</sub>CO<sub>3</sub>.

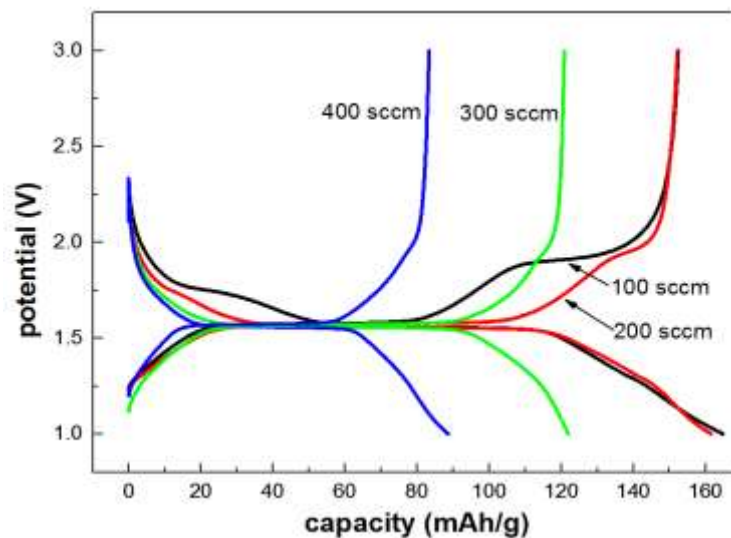
After optimizing the O<sub>2</sub> flow rate to 1 sccm, the effect of Li-precursor flow rate on the deposited films was also investigated, as shown in Figure 4.4. The films deposited at lower Li-precursor flow rates (100 sccm and 200 sccm) show the characteristic diffraction pattern of

LTO. However, beside LTO, the presence of TiO<sub>2</sub> impurity was also detected, indicated by b. It is likely that for these relatively low Li flow rates, the amount of supplied lithium is not sufficient to facilitate the growth of pure LTO. When the Li flow rate is increased to 300 sccm, pure LTO was obtained. Increasing the Li flow rate to 400 sccm does not have further influence on the phase formation process. At this high Li-precursor flow rate, the extra supply of Li may lead to the formation of amorphous Li-compounds, which cannot be detected by XRD. Based on the discussed XRD results, it can be concluded that 300 sccm is the optimal Li-precursor flow rate for the deposition of pure LTO.



**Figure 4.4** XRD patterns of thin films deposited with various Li-precursor flow rates and fixed oxygen and titanium precursor flow rates at 1 and 200 sccm, respectively.

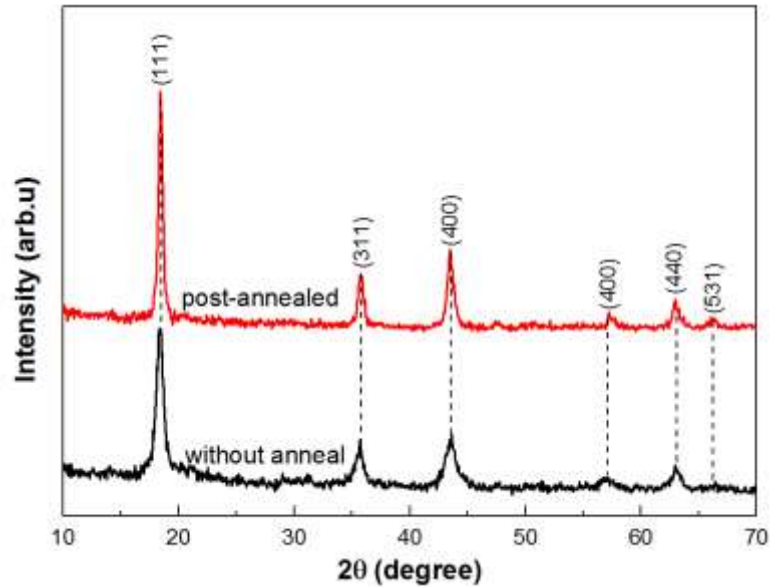
The electrochemical performance of the films deposited with various Li-precursor flow rates is shown in Figure 4.5. In the (dis)charge voltage curves of the films deposited at a 100 sccm Li flow rate (black curve), two discharging plateaus can be observed at 1.72 and 1.55 V, respectively. Comparably, two charging plateaus are present at 1.55 and 1.91 V. The flat (dis)charging plateaus around 1.55 V match very well with the potential at which the reaction  $\text{LTO} + 3\text{Li}^+ + 3\text{e}^- \leftrightarrow \text{Li}_7\text{Ti}_5\text{O}_{12}$  takes place. The additional discharging plateau at 1.72 V and the charging plateau at about 1.91 V match with those reported for TiO<sub>2</sub> [15]. For the film synthesized with a Li-precursor flow rate of 200 sccm, the high voltage (dis)charging capacity, which can be attributed to TiO<sub>2</sub>, decreases. This result is consistent with the XRD pattern shown in Figure 4.4, which indicates that TiO<sub>2</sub> is formed at lower Li flow rates.



**Figure 4.5** Voltage curves of thin film electrodes deposited with different Li-precursor flow rates at a (dis)charge rate of 0.5 C.

The increase of the Li-precursor flow rate to 300 sccm results in films that do not show any plateaus corresponding to  $\text{TiO}_2$  during electrochemical testing. Further increasing the Li-precursor flow rate to 400 sccm doesn't change the shape of the (dis)charging curve, but the storage capacity of the film decreases significantly. This may be due to excess Li in the form of amorphous  $\text{Li}_2\text{O}$  or  $\text{Li}_2\text{O}_2$  which might be incorporated into LTO during the deposition process <sup>[16]</sup>.

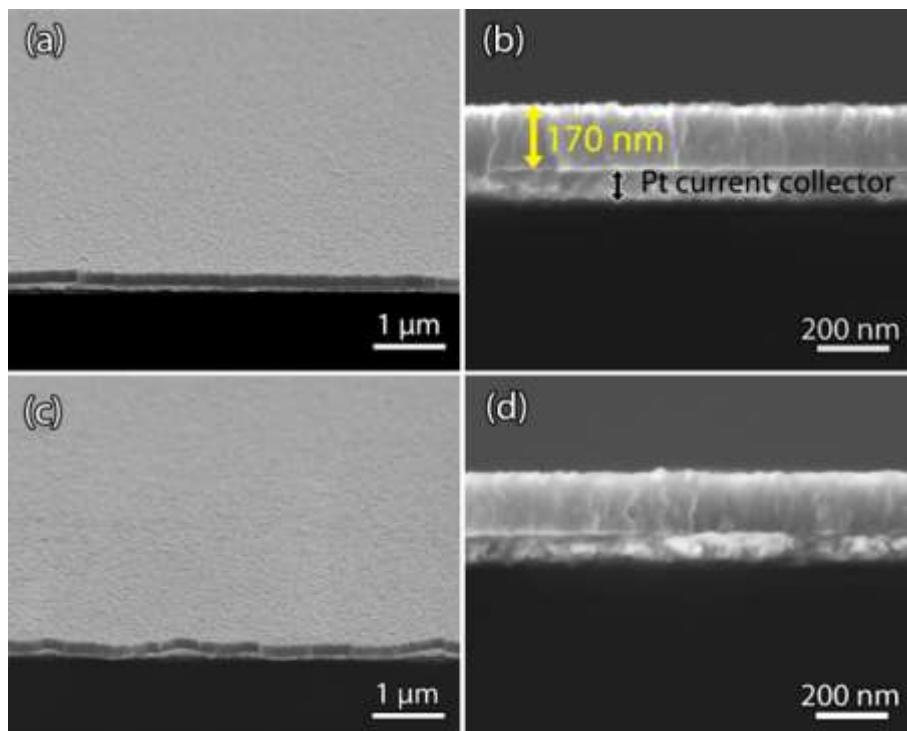
The (de)lithiation of LTO involves a two-phase reaction. Different from solid solution like (de)lithiation materials, the voltage of LTO electrode quickly goes to 1.55 V at the beginning of the (dis)charging process, where the two-phase process takes place. Subsequently, at the end of (dis)charging, the potential quickly reaches the cut-off voltage <sup>[17]</sup>. The voltage curve of the film deposited with a Li-precursor flow rate of 300 sccm shows the typical (dis)charging plateaus of a LTO anode. However, at the beginning and the end of discharging, the voltage is slowly decreasing or increasing, which is different from the generally observed behavior, aforementioned. The relatively low deposition temperature used in this study (500°C), which is much lower than the deposition temperature of other preparation methods, such as sol-gel <sup>[4]</sup>, ALD <sup>[18]</sup> and solid-state reaction <sup>[19]</sup>, might be the reason for this deviating behavior.



**Figure 4.6** XRD patterns of LTO films (deposited with 1 sccm  $O_2$ , 300 sccm Li and 200 sccm Ti-precursor flow rates) with and without post-annealing.

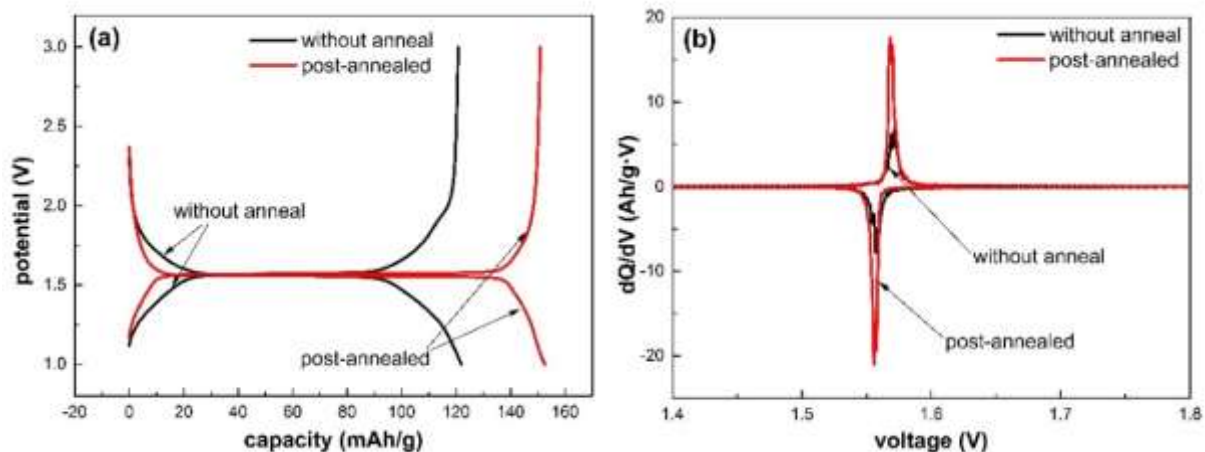
In order to get better crystallized LTO, the films deposited with optimized  $O_2$  and Li-precursor flow rates (1 and 300 sccm, respectively) were annealed at 800 °C for 15 min under Ar atmosphere. As shown in Figure 4.6, the intensity of the diffraction peaks of LTO increased significantly after post-annealing. In addition, the full width at half maximum (FWHM) of the diffraction peaks decreased substantially. For example, the FWHM of the (111) reflection decreased from 0.69° to 0.41°. According to Scherrer Equation, the mean size of LTO is increased from 12.1 nm to 20.4 nm. Based on the increase of peak intensity and decrease of the FWHM, it can be concluded that the crystallinity of the deposited LTO films improved as a result of the post-annealing process. Figure 4.7 shows the SEM images of a deposited film without and with post-annealing. The film appears very homogenous, without any obvious cracks or pinholes. The film attached very well with the substrate. The visible delaminating is the result of sample preparation for cross-section view. Two hours of deposition yields a 170 nm thick film and hence the growth rate is about 85 nm/h.





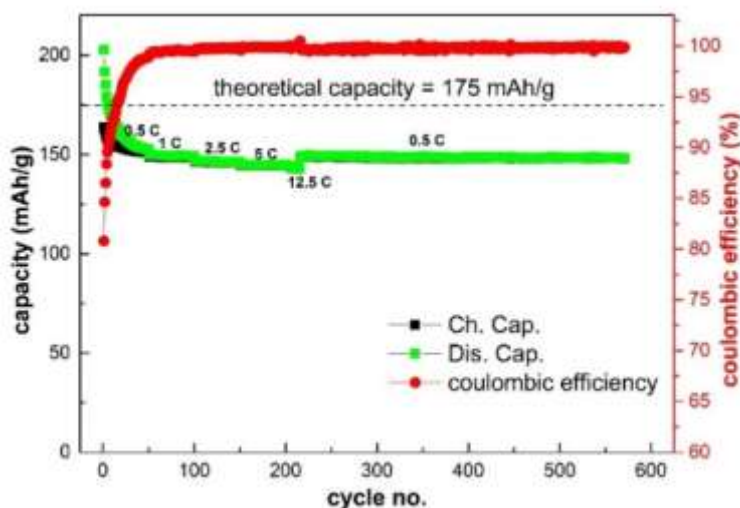
**Figure 4.7** SEM images of LTO films deposited at 1 sccm O<sub>2</sub> and 300 sccm Li-precursor flow rate without ((a) and (b)) and with ((c) and (d)) post-annealing at 800 °C for 15 min.

Figure 4.8a shows the influence of post-annealing on the voltage curves. After being annealed at 800 °C, the post-annealed film now shows the conventional (dis)charging behavior. Two sharp redox peaks around 1.55 V can be clearly seen from the derivative of storage capacity with respect to voltage curves, as shown in Figure 4.8b. Besides the shape change of the voltage curve, the annealing treatment also induced an increase of storage capacity. The (de)lithiation of LTO anode is a two phase reaction between Li<sub>4</sub>Ti<sub>5</sub>O<sub>12</sub> and Li<sub>7</sub>Ti<sub>5</sub>O<sub>12</sub>. Both Li<sub>4</sub>Ti<sub>5</sub>O<sub>12</sub> and Li<sub>7</sub>Ti<sub>5</sub>O<sub>12</sub> are crystals. A well crystallized Li<sub>4</sub>Ti<sub>5</sub>O<sub>12</sub> electrode would facilitate the two phase transformation, resulting in better electrochemical performance, as reported before [4, 18, 19]. Thus, the capacity increase after post-annealing can most likely be attributed to the increased degree of crystallinity of the LTO film as confirmed by XRD.



**Figure 4.8** Voltage curves (a) and derivative of storage capacity with respect to voltage curves (b) of LTO films with and without post-annealing. Discharging and charging current is 0.5 C.

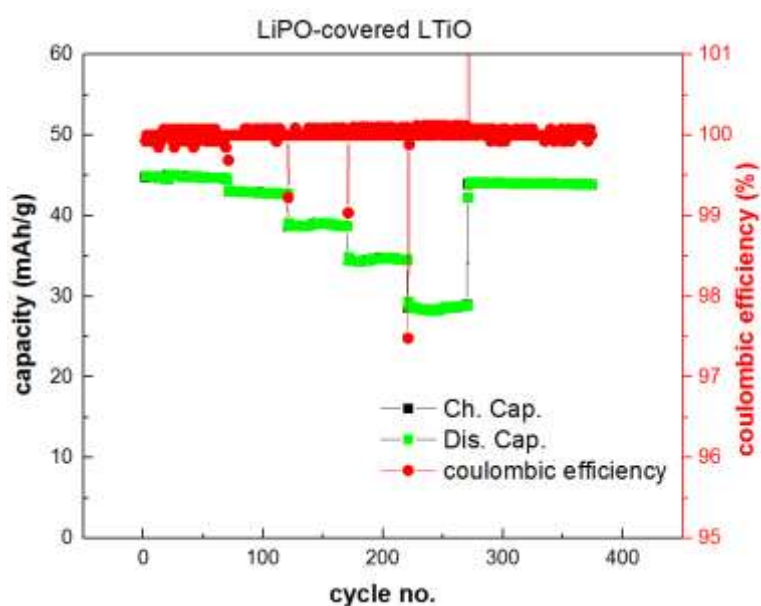
Figure 4.9 shows the cycling performance of the post-annealed LTO films, which were deposited using the optimized deposition parameters (flow rates of O<sub>2</sub>, Li and Ti-precursors are 1, 300 and 200 sccm, respectively). A capacity of 151 mAh/g, 86% of the theoretical specific capacity (175 mAh/g), can be attained at 0.5 C, which is comparable or higher than the value reported for films deposited by other methods [6, 8, 10]. There is no significant capacity loss up to 570 cycles.



**Figure 4.9** Storage capacity retention of the post-annealed LTO films (800 °C for 15 min).

It is interesting to notice that during the initial stages of cycling, the coulombic efficiency is relative low, which may due to side reactions. Various (electro)chemical reactions between

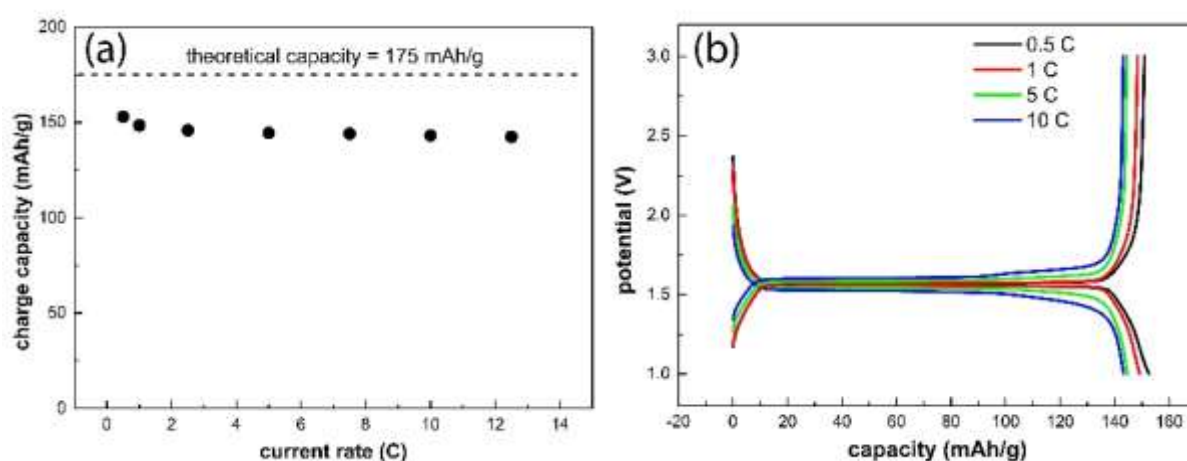
LTO and the electrolyte have been reported in the literature, leading to severe gassing of LTO anodes during (dis)charging [20-22]. Besides, aging effects, surface contamination, or moisture in the electrolyte may also induce other side reactions, resulting in irreversible capacity losses. The phenomenon of low coulombic efficiency of LTO anodes in the initial stages of (dis)charging has been reported in previous reports, including thin film electrodes [8, 10, 23] and conventional paste electrodes [24]. After protecting the LTO electrode with a thin film solid-state electrolyte, we found that the coulombic efficiency of the LTO electrode was significantly improved, even at the beginning of cycling, as shown in Figure 4.10. However, this improvement is at the expense of extra capacity losses due to the increased electrode impedance. Consequently, the likely explanation of the low coulombic efficiency in the beginning of the cycling tests may be attributed to side reactions. It is worthy to notice that, except for the initial cycles, the coulombic efficiency of the LTO electrode is almost equal to 100% (varied from 99.5% to 99.9%) up to 500 cycles, clearly indicating that the prepared LTO electrodes have excellent reversibility.



**Figure 4.10** Rate performance and coulombic efficiency of a LiPO-covered LTO electrode.

Beside the good cycle performance, the thin film electrode also shows an excellent rate capability. As shown in Figure 4.11a, compared to the capacity obtained at 0.5 C, the deposited LTO anode shows a capacity retention of 93% and 91% at 5 C and 10 C, respectively. Figure 4.11b shows the voltage curves at different current rates. At low current densities (0.5 and 1 C), the charge and discharge curves show the plateau regions between 1.5 and 1.6 V vs Li/Li<sup>+</sup>. As

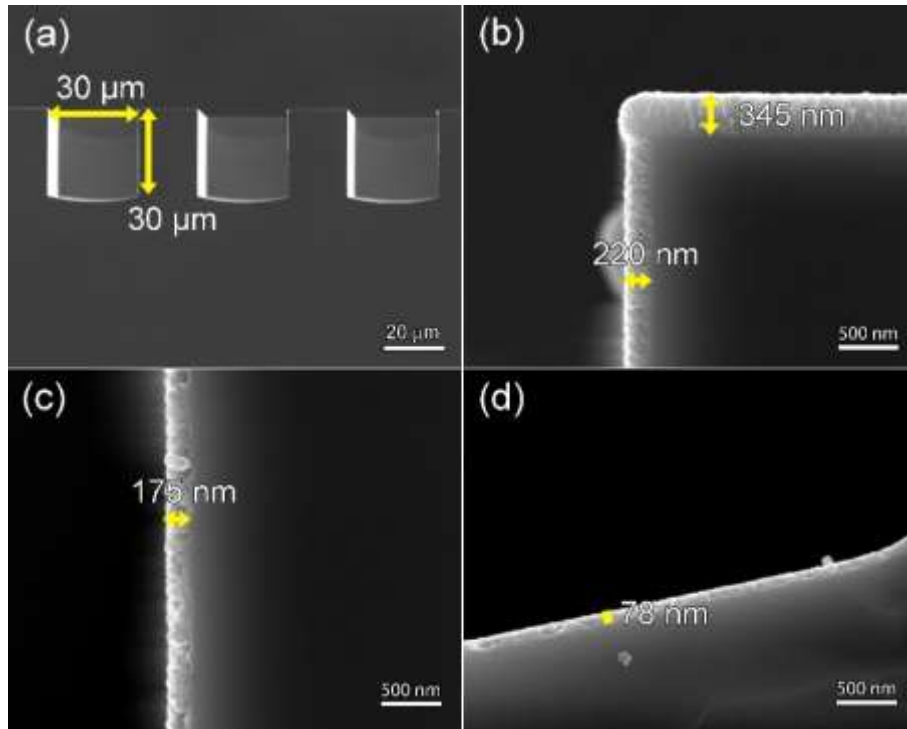
the current densities increases, the charging plateau shifts to higher voltage and the discharging plateau shifts to lower voltage, indicating an increase of overpotential. But from 0.5 C to 10 C, the increase of overpotential is very limited, which is consistent with the marginal capacity loss as (dis)charging current increases. Without adding any conducting additives or special morphology optimization, the MOCVD deposited LTO film electrodes manifest an excellent cycling performance and rate capability, which are comparable with LTO anodes with special morphologies, such as nanowires [25, 26] and nanosheets [27].



**Figure 4.11** Rate performance (a) and voltage curves at different current rate (b) of the post-annealed LTO films (800 °C for 15 min).

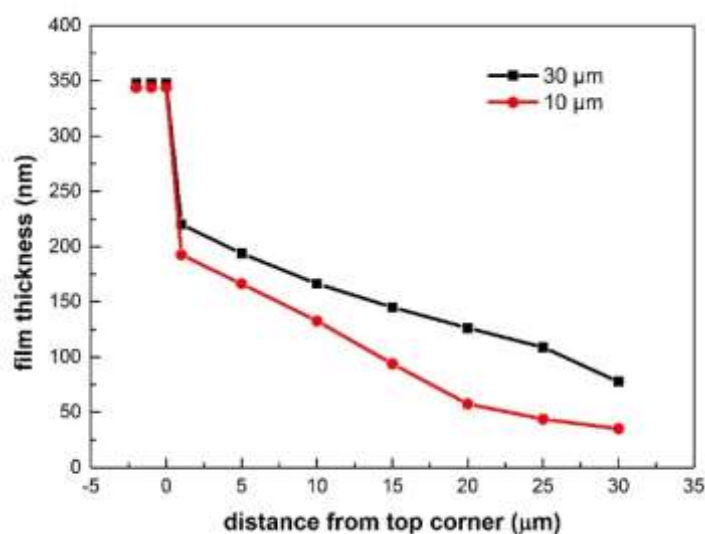
#### 4.4 Deposition on 3D substrates

The volumetric storage capacity and rate capability are key properties for micro-batteries. 3D electrode structures hold promise for significant energy density enhancement without much loss of power performance, or alternatively a tunable optimization and tradeoff between energy and power to fit the application [11, 28]. The key issue of making highly structured micro-batteries is the homogeneous deposition of various batteries components in 3D. To investigate this possibility for a LTO anode, films were deposited on 3D substrates to analyze the uniformity.



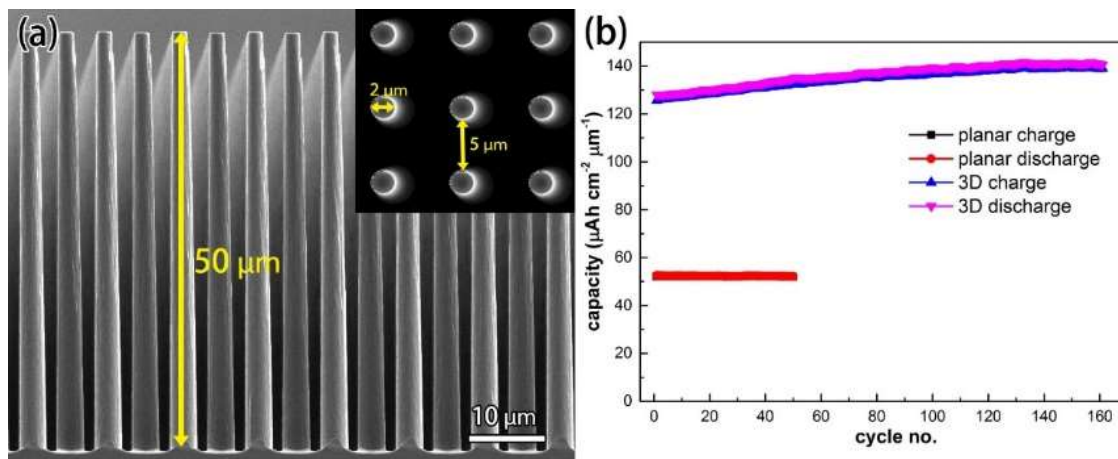
**Figure 4.12** Configuration of the 3D substrate for layer uniformity analysis (a), deposited LTO film on the top (b), middle (c) and bottom (d) of a 3D trench.

Figure 4.12a shows a SEM image of a 3D trench substrate. Figure 4.12b, c and d show the deposited film thicknesses at the top, middle and bottom of a 30  $\mu\text{m}$  wide and deep trench, respectively. A high quality continuous film is deposited on the top surface and inside the trenches. However, the film reveals an instantaneous thickness drop inside the trench, followed by a continuous decrease further down to the bottom of the trench. The film thickness is about 78 nm at the bottom (Figure 4.12d), which amounts to 23% of the thickness at the surface. The film deposited inside the 10  $\mu\text{m}$  wide trench shows a similar thickness evolution but the step coverage, defined as the ratio of the film thickness at the bottom and the thickness at the top, was reduced to 10%, as summarized in Figure 4.13. Most likely the deposition of LTO at 500  $^{\circ}\text{C}$  is a diffusion-controlled process and the thin film growth is therefore, at least partially, limited by the diffusion of the mixed precursor gasses. Compared to the precursor gasses concentration at the surface, the concentrations inside the trenches decrease quickly and hence the deposited film thickness will become thinner. This effect is more pronounced for smaller trenches with high aspect ratio.



**Figure 4.13** Film thickness as a function of depth in trenches with two difference widths, 10 and 30  $\mu\text{m}$  respectively. The top-corner of the trench is taken as 0.

To prove the concept of 3D electrodes, the LTO film anodes were deposited on 3D micro-pillar substrates to test the electrochemical performance. Figure 4.14a shows the configuration of the applied 3D substrate. Based on the geometry of the substrate, the theoretical surface area increase is 7.4 times. As shown in Figure 4.14b, due to the enlarged active surface area, under the same deposition time, the LTO film deposited on the 3D substrate shows a 2.5 times higher storage capacity than the film deposited on planar substrate. As shown earlier for the trenched substrates, the thickness of the film along the pillars will not be uniform and therefore the theoretical capacity enhancement was not obtained. However, the result shows that the ability of depositing high quality electrodes on a 3D substrate is a powerful tool to enhance the storage capacity within limited footprint area. It is interesting to notice that the storage capacity of the film deposited on a 3D substrate is slowly increasing during the electrochemical test. Since the length of the pillars (50  $\mu\text{m}$ ) is much bigger than the distance between them (5  $\mu\text{m}$ ), some gas may be trapped at the bottom when the cell was filled with liquid electrolyte, resulting in a (partially) inactive (not wetted) electrode surface at the bottom. During the electrochemical test, the liquid electrolyte may slowly infiltrate to the bottom part, resulting in a slow storage capacity increase. Actually, after 100 cycles, the capacity of 3D LTO electrode stabilized, as shown in Figure 4.14b.



**Figure 4.14** Cross-section view of the 3D substrate used for electrochemical measurements, inset image is the top-view (a), electrochemical performances of LTO film anodes deposited on planar and 3D substrates, respectively (b).

#### 4.5 LTO/LiPON/Li all-solid-state cell

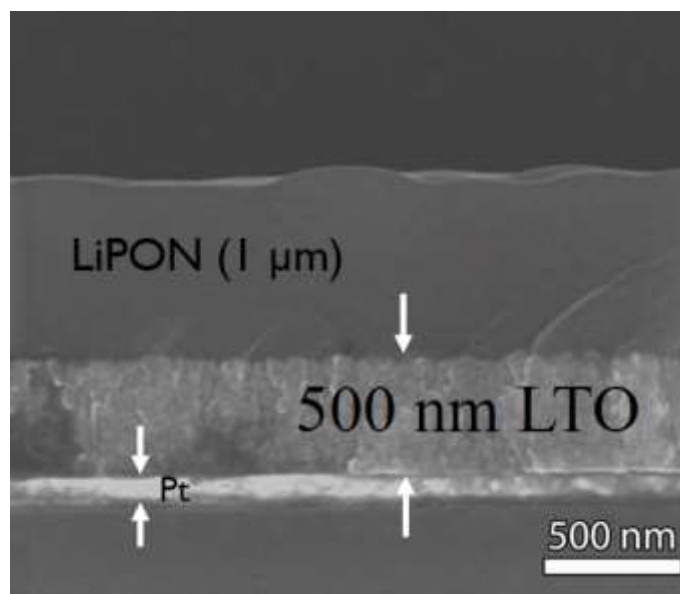


**Figure 4.15** Cross-section SEM image of Pt/LTO/LiPON half-cell.

As a demonstration of planar all-solid-state battery, 500 nm LTO was deposited on a Pt covered Si wafer. On top of the LTO electrode, a layer of 1 μm nitrogen doped lithium phosphate (LiPON) is deposited by magnetron sputtering. Subsequently, a layer of metallic lithium was deposited by thermal evaporation. In the end, the LTO/LiPON/Li pack was sealed inside a polymer resin to avoid the air and moisture contamination. Because metallic Li is sensitive to air, only the LTO/LiPON half-cell was subjected to SEM observation, as shown in Figure 4.15. From the cross-section view, all the deposited films are homogeneous and attach to

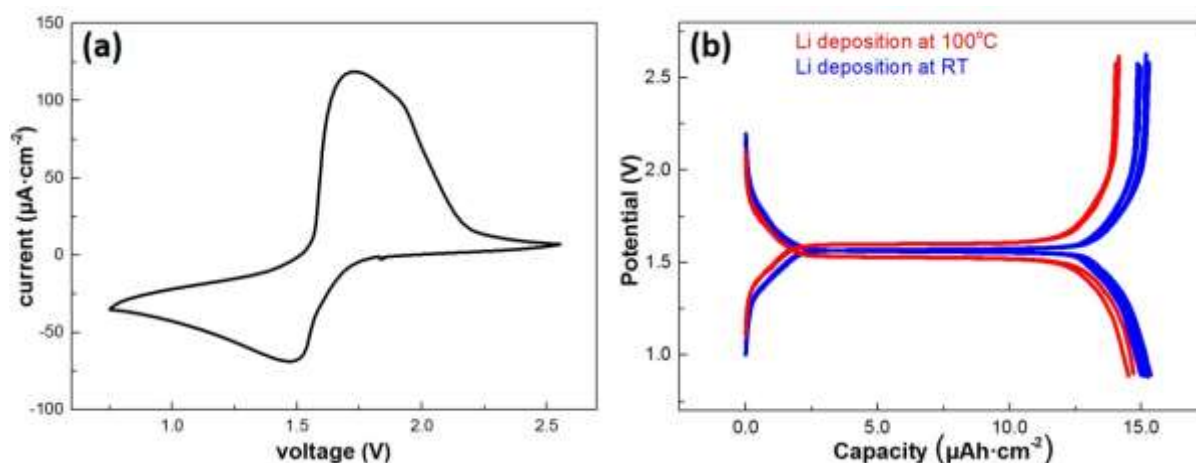
each other very well. For the 500 nm LTO layer, grain boundaries can be observed. While for the sputtered LiPON film, there are no visible cracks or grains, indicating that the deposited LiPON layer is likely to be amorphous.

Figure 4.16 shows the CV plot of the Li/LiPON/LTO all-solid-state battery. It is interesting to note that the CV plot of a full cell deviates a lot from the conventional LTO electrodes (Figure 4.8b), which is tested in a liquid electrolyte. The redox peaks become much broader and the overpotential between the oxidation/reduction peaks has increased. This deviation is likely attributed to the interfaces, *i.e.* the interface between LTO and LiPON (LTO/LiPON) and the interface between LiPON solid electrolyte and Li metal (LiPON/Li). Here, we focused on the interface between LiPON and metallic Li. For the LiPON/Li interface, there are two possibilities which may influence the electrochemical behavior of LTO electrode. One is that the attachment between the two layer is poor. The other possibility is that an interface is formed between Li and LiPON and that this interface has a poor ionic conductivity. Improving the temperature of Pt/LTO/LiPON half-cell during the deposition of Li metal is likely to improve the attachment between Li metal and LiPON, since high depositing temperature would facilitate the diffusion of deposited Li atom on the LiPON surface and improve the adhesion. However, as shown in Figure 4.16b, when Li metal was deposited at 100 °C, the Li/LiPON/LTO all-solid-state cell has higher overpotential but lower capacity than that deposited at room temperature, showing worse performance. So, it is likely that the higher deposition temperature facilitates the formation of interface layer between the LiPON solid electrolyte and Li metal and this interface layer has poor ionic conductivity, which compromises the electrochemical performance of the LTO/LiPON/Li all-solid-state cell.

Similar to the voltage curves tested in liquid electrolyte, the all-solid-state cell also manifests a flat (dis)charging plateau around 1.55 V (blue curve), showing the typical electrochemical behaviors of LTO electrode. Therefore, an electrochemical active LTO/LiPON/Li all-solid-state cell is successfully prepared. It is also worthy to notice that the capacity yield by the all-solid-state cell is only around 50% of the theoretical value, which is much less than the result shown in Figure 4.11, especially considering a much lower current rate (0.1 C) is applied. The likely reason is due to the two solid interfaces. As already shown in Figure 4.10, only by adding a thin layer of LiPO (200 nm), the capacity of the LTO/LiPO cell has already decreased a lot. Although the ionic conductivity of LiPON is two magnitudes higher than LiPO, the negative effect brought by the LTO/LiPON interface may still be significant.



For the interface between LiPON and Li metal, as already discussed, even the deposition temperature would significantly influence the overpotential and capacity. Therefore, to prepare all-solid-state batteries with good electrochemical performances, not only the deposition of each film component needs to be optimized, the interfaces between different film components also need to be carefully designed. Adding a very thin buffer layer or choosing suitable solid electrolyte are possible solutions.



**Figure 4.16** CV plot (a) and voltage curves (b) of the Li/LiPON/LTO all-solid-state cell. The scan rate of the CV is 1 mV/s. The C rate for the voltage curves measurement is 0.1 C.

## 4.6 Conclusions

High quality LTO thin films were successfully deposited by MOCVD. At low Li-precursor flow rates,  $\text{TiO}_2$  was formed in addition to LTO. The Li-precursor flow rate strongly affects the electrochemical performance of the deposited films. The attachment between LTO and Pt current collector can be improved by adding a thin  $\text{TiO}_2$  adhesion layer. A post-annealing process significantly improves the crystallinity and electrochemical performance of the deposited films. LTO films deposited at the optimized process conditions possess a high electrochemical storage capacity and excellent rate capability. The thin film electrodes show no significant capacity loss even after almost 600 cycles, and maintain 93% of the initial capacity at 10 C. The 3D deposition of LTO was also investigated. A step-coverage of 23% and 10% was achieved for the 30 and 10  $\mu\text{m}$  wide trenches, respectively. Compared to planar substrate, with the same footprint area, the 3D LTO film anode showed a 2.5 times higher storage capacity. As a demonstration, Li/LiPON/LTO all-solid-state cell was prepared by combining different deposition techniques. The prepared all-solid-state cell manifest (dis)charging

plateaus around 1.55 V, showing good electrochemical activity. However, only half of the theoretical capacity was achieved. The lost capacity is likely due to the increased internal resistance, which attributed to the two solid interface of the solid-state cell.

## References

1. L. Baggetto, R.A.H. Niessen, F. Roozeboom, and P.H.L. Notten, *High Energy Density All-Solid-State Batteries: A Challenging Concept Towards 3D Integration*. *Advanced Functional Materials* **18** (2008) 1057-1066.
2. T. Ohzuku, A. Ueda, and N. Yamamoto, *Zero-Strain Insertion Material of  $\text{Li}[\text{Li}_{1/3}\text{Ti}_{5/3}]\text{O}_4$  for Rechargeable Lithium Cells*. *Journal of the Electrochemical Society* **142** (1995) 1431-1435.
3. T.F. Yi, L.J. Jiang, J. Shu, C.B. Yue, R.S. Zhu, and H.B. Qiao, *Recent development and application of  $\text{Li}_4\text{Ti}_5\text{O}_{12}$  as anode material of lithium ion battery*. *Journal of Physics and Chemistry of Solids* **71** (2010) 1236-1242.
4. Y.H. Rho, K. Kanamura, M. Fujisaki, J. Hamagami, S. Suda, and T. Umegaki, *Preparation of  $\text{Li}_4\text{Ti}_5\text{O}_{12}$  and  $\text{LiCoO}_2$  thin film electrodes from precursors obtained by sol-gel method*. *Solid State Ionics* **151** (2002) 151-157.
5. L. Kavan and M. Gratzel, *Facile synthesis of nanocrystalline  $\text{Li}_4\text{Ti}_5\text{O}_{12}$  (spinel) exhibiting fast Li insertion*. *Electrochemical and Solid State Letters* **5** (2002) A39-A42.
6. C.L. Wang, Y.C. Liao, F.C. Hsu, N.H. Tai, and M.K. Wu, *Preparation and Characterization of Thin Film  $\text{Li}_4\text{Ti}_5\text{O}_{12}$  Electrodes by Magnetron Sputtering*. *Journal of The Electrochemical Society* **152** (2005) A653.
7. F. Wunde, F. Berkemeier, and G. Schmitz, *Lithium diffusion in sputter-deposited  $\text{Li}_4\text{Ti}_5\text{O}_{12}$  thin films*. *Journal of Power Sources* **215** (2012) 109-115.
8. Y. Yu, J.L. Shui, and C.H. Chen, *Electrostatic spray deposition of spinel  $\text{Li}_4\text{Ti}_5\text{O}_{12}$  thin films for rechargeable lithium batteries*. *Solid State Communications* **135** (2005) 485-489.
9. R. Inada, K. Shibukawa, C. Masada, Y. Nakanishi, and Y. Sakurai, *Characterization of as-deposited  $\text{Li}_4\text{Ti}_5\text{O}_{12}$  thin film electrode prepared by aerosol deposition method*. *Journal of Power Sources* **253** (2014) 181-186.
10. K. Tadanaga, A. Yamaguchi, A. Hayashi, M. Tatsumisago, J. Mosa, and M. Aparicio, *Preparation of  $\text{Li}_4\text{Ti}_5\text{O}_{12}$  electrode thin films by a mist CVD process with aqueous precursor solution*. *Journal of Asian Ceramic Societies* **3** (2015) 88-91.
11. P.H.L. Notten, F. Roozeboom, R.A.H. Niessen, and L. Baggetto, *3-D Integrated All-Solid-State Rechargeable Batteries*. *Advanced Materials* **19** (2007) 4564-4567.
12. J.F.M. Oudenhoven, L. Baggetto, and P.H.L. Notten, *All-Solid-State Lithium-Ion Microbatteries: A Review of Various Three-Dimensional Concepts*. *Advanced Energy Materials* **1** (2011) 10-33.
13. J. Xie, J.F.M. Oudenhoven, P.P.R.M.L. Harks, D.J. Li, and P.H.L. Notten, *Chemical Vapor Deposition of Lithium Phosphate Thin-Films for 3D All-Solid-State Li-Ion Batteries*. *Journal of the Electrochemical Society* **162** (2015) A249-A254.
14. L. Baggetto, H.C.M. Knoop, R.A.H. Niessen, W.M.M. Kessels, and P.H.L. Notten, *3D negative electrode stacks for integrated all-solid-state lithium-ion microbatteries*. *Journal of Materials Chemistry* **20** (2010) 3703-3708.
15. Z. Chen, I. Belharouak, Y.K. Sun, and K. Amine, *Titanium-Based Anode Materials for Safe Lithium-Ion Batteries*. *Advanced Functional Materials* **23** (2013) 959-969.
16. L. Aldon, P. Kubiak, M. Womes, J.C. Jumas, J. Olivier-Fourcade, J.L. Tirado, J.I. Corredor, and C.P. Vicente, *Chemical and electrochemical Li-insertion into the  $\text{Li}_4\text{Ti}_5\text{O}_{12}$  spinel*. *Chemistry of Materials* **16** (2004) 5721-5725.

17. M.S. Song, A. Benayad, Y.M. Choi, and K.S. Park, *Does  $\text{Li}_4\text{Ti}_5\text{O}_{12}$  need carbon in lithium ion batteries? Carbon-free electrode with exceptionally high electrode capacity*. Chem Commun (Camb) **48** (2012) 516-8.
18. X. Meng, J. Liu, X. Li, M.N. Banis, J. Yang, R. Li, and X. Sun, *Atomic layer deposited  $\text{Li}_4\text{Ti}_5\text{O}_{12}$  on nitrogen-doped carbon nanotubes*. RSC Advances **3** (2013) 7285-7288.
19. X. Li, M.Z. Qu, and Z.L. Yu, *Preparation and electrochemical performance of  $\text{Li}_4\text{Ti}_5\text{O}_{12}$ /graphitized carbon nanotubes composite*. Solid State Ionics **181** (2010) 635-639.
20. Y.B. He, B.H. Li, M. Liu, C. Zhang, W. Lv, C. Yang, J. Li, H.D. Du, B.A. Zhang, Q.H. Yang, J.K. Kim, and F.Y. Kang, *Gassing in  $\text{Li}_4\text{Ti}_5\text{O}_{12}$ -based batteries and its remedy*. Scientific Reports **2** (2012).
21. I. Belharouak, G.M. Koenig, T. Tan, H. Yumoto, N. Ota, and K. Amine, *Performance Degradation and Gassing of  $\text{Li}_4\text{Ti}_5\text{O}_{12}$ / $\text{LiMn}_2\text{O}_4$  Lithium-Ion Cells*. Journal of The Electrochemical Society **159** (2012) A1165-A1170.
22. K. Wu, J. Yang, Y. Zhang, C. Wang, and D. Wang, *Investigation on  $\text{Li}_4\text{Ti}_5\text{O}_{12}$  batteries developed for hybrid electric vehicle*. Journal of Applied Electrochemistry **42** (2012) 989-995.
23. J. Mosa, J.F. Velez, J.J. Reinoso, M. Aparicio, A. Yamaguchi, K. Tadanaga, and M. Tatsumisago,  *$\text{Li}_4\text{Ti}_5\text{O}_{12}$  thin-film electrodes by sol-gel for lithium-ion microbatteries*. Journal of Power Sources **244** (2013) 482-487.
24. J. Li, Y.L. Jin, X.G. Zhang, and H. Yang, *Microwave solid-state synthesis of spinel  $\text{Li}_4\text{Ti}_5\text{O}_{12}$  nanocrystallites as anode material for lithium-ion batteries*. Solid State Ionics **178** (2007) 1590-1594.
25. J.-Y. Liao, V. Chabot, M. Gu, C. Wang, X. Xiao, and Z. Chen, *Dual phase  $\text{Li}_4\text{Ti}_5\text{O}_{12}$ - $\text{TiO}_2$  nanowire arrays as integrated anodes for high-rate lithium-ion batteries*. Nano Energy **9** (2014) 383-391.
26. L. Shen, E. Uchaker, X. Zhang, and G. Cao, *Hydrogenated  $\text{Li}_4\text{Ti}_5\text{O}_{12}$  Nanowire Arrays for High Rate Lithium Ion Batteries*. Advanced Materials **24** (2012) 6502-6506.
27. T.-F. Yi, Z.-K. Fang, Y. Xie, Y.-R. Zhu, and S.-Y. Yang, *Rapid Charge–Discharge Property of  $\text{Li}_4\text{Ti}_5\text{O}_{12}$ - $\text{TiO}_2$  Nanosheet and Nanotube Composites as Anode Material for Power Lithium-Ion Batteries*. ACS Applied Materials & Interfaces **6** (2014) 20205-20213.
28. D. Golodnitsky, M. Nathan, V. Yufit, E. Strauss, K. Freedman, L. Burstein, A. Gladkikh, and E. Peled, *Progress in three-dimensional (3D) Li-ion microbatteries*. Solid State Ionics **177** (2006) 28112819.



# Chapter 5 Deposition of 3D-Structured TiO<sub>2</sub>

## Electrodes

### ***Abstract***

As sensors, wireless communication devices, personal health monitoring systems and autonomous micro-electro-mechanical systems (MEMS) become more distributed and continuously smaller, there is an increasing demand for miniaturized integrated power sources. Despite the many advantages of thin film batteries, their power and energy per unit area are however still too limited to cope with the energy and power needs of these devices. Moving from planar structures to high-aspect ratio 3D electrodes holds promise to significantly increase the energy density and rate performance. Here, we demonstrate an on-chip compatible method to fabricate high energy density TiO<sub>2</sub> thin film electrodes on 3D-structured silicon substrates. 3D-structured electrodes are fabricated by combining reactive ion etching (RIE) with low pressure chemical vapor deposition (LPCVD), enabling accurate control of the aspect ratio of substrates and the subsequent deposition of TiO<sub>2</sub> thin film electrodes onto these structured substrates. The prepared 3D-TiO<sub>2</sub> electrodes exhibit a current-dependent increase in storage capacity of a factor up to 16 as compared to conventional planar electrodes. In addition, these 3D electrodes also reveal an excellent power and cycling performance. This demonstrates that 3D-electrodes can simultaneously improve the storage capacity and power density of thin film batteries.

# 5.1 Introduction

Nowadays, many electronic products are becoming smart and connected. Thousands of wireless sensors united in networks collect useful data that make our lives safer and more convenient. As sensors, wireless communication devices, personal health monitoring systems and autonomous micro-electro-mechanical systems (MEMS) become more widespread and individual sensor nodes become more compact [1-5], there is an increasing demand for integrated power sources. Typically, there is a demand for batteries in the 1 ~ 10 mm<sup>3</sup> volume range, including all components and associated packaging [6]. Moreover, for use in miniaturized devices, it is usually required that the energy storage functions are physically located on a small chip area. A miniaturized on-chip battery would be highly desirable for these applications, making the energy and power density per footprint area a key attribute of these batteries.

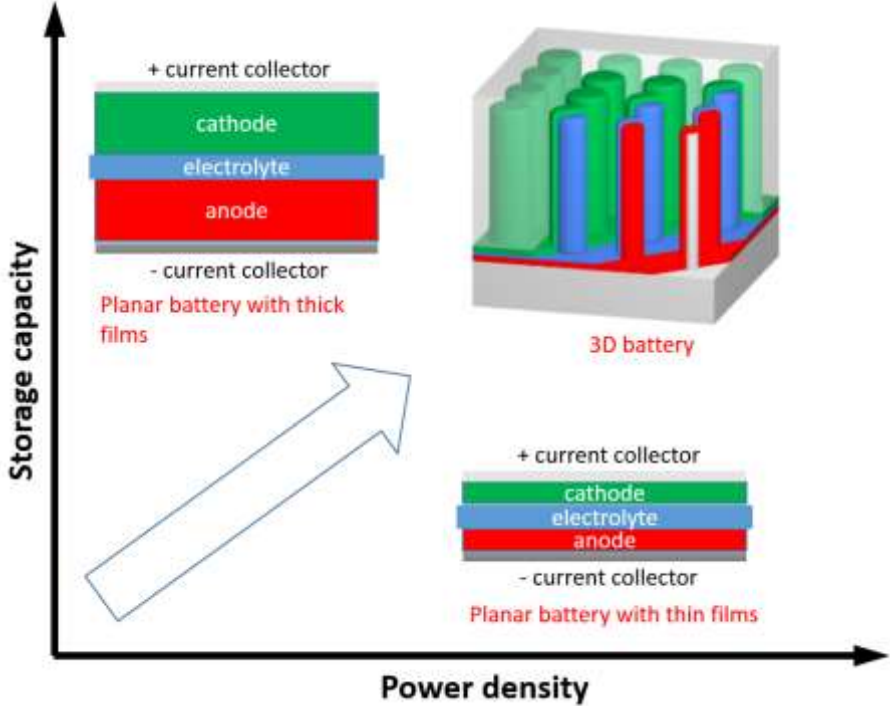


**Figure 5.1** Design of a 3D microbatteries and its advantages compared with planar microbatteries.

Conventional 2D thin film microbatteries can deliver high power, but require large footprint areas to store reasonable energies. On the other hand, making the electrodes thicker boosts the theoretical areal energy density but the resultant increase in electronic and ionic diffusion lengths reduces the effective power. This energy and power dilemma is schematically shown in Figure 5.1. The most promising way to combine a high storage capacity and high power

capability on a limited area is to integrate all batteries components, *i.e.* current collectors, electrodes and electrolyte, in a 3-dimensional (3D) arrangement, thus generating a 3D microbatteries (Figure 5.1) [7-11]. Due to the large surface area of these electrodes, high capacities per footprint area can be obtained. High power capabilities can also be realized by carefully designing the batteries to obtain short transport distances between the electrodes [12-14]. It is important to recognize that for small electronic- and MEMS-type devices, the available area is limited. Traditional performance indicators of batteries, namely gravimetric, volumetric energy and power densities are therefore less relevant. Instead, the real issue is how much energy and power a device can deliver per footprint area, measured in terms of  $\text{mAh}\cdot\text{cm}^{-2}$ ,  $\text{J}\cdot\text{cm}^{-2}$  or  $\mu\text{W}\cdot\text{mm}^{-2}$ , *etc.* [15].

$\text{TiO}_2$  has been considered as a promising electrode for Li-ion batteries as it is safe, non-toxic, readily available and has a high theoretical volumetric capacity. However, the poor conductivity and slow diffusion rate of  $\text{Li}^+$  in  $\text{TiO}_2$  has restricted the rate capability and storage capacity of  $\text{TiO}_2$  [16, 17]. A potential solution to overcome this limitation is simply by decreasing the thin film thickness. However, nano-sizing the film thickness typically leads to severe capacity reduction. Employing 3D- $\text{TiO}_2$  thin film electrodes is, however, a promising method to solve this dilemma [18-20].

Several reports have demonstrated that 3D- $\text{TiO}_2$  electrodes reveal a higher footprint areal storage capacity and power performance [18, 19, 21-23]. However, since these methods are not directly based on Si substrate technology, integrating these 3D batteries onto chips or micro-sensors would be very challenging. Besides, in some work, the applied deposition method is atomic layer deposition (ALD) [18, 19, 21]. The ALD processes are complicated and the growth rate is slow, limiting large scale production. Reactive ion etching (RIE) and low pressure chemical vapor deposition (LPCVD) are two commonly used techniques in the semiconductor industry. The RIE method is very convenient in creating periodically micro-structured 3D substrates with high aspect ratios and LPCVD is capable of producing high quality, high-performance thin films [14, 20, 24]. Here, we report a flexible and on-chip 3D microbatteries by combining the techniques of RIE with LPCVD. Here, we report a flexible and precise fabrication route to create 3D microbatteries by combining RIE with LPCVD. The RIE method creates a periodically micro-structured 3D substrate with high aspect ratios. Two kinds of 3D-structured substrates with varying aspect ratios have been investigated. One approach is to etch trenches; another approach is in the form of pillars. Trench substrates are convenient to prepare



samples for cross-section view to check the uniformity of deposited films. Due to more open space, Si pillar substrates are more convenient for mass production and easy to be coated with ALD-deposited TiN, which serves as current collector. LPCVD is commonly used in the semiconductor industry and capable for large scale wafer deposition. In this chapter, homogeneous 3D-TiO<sub>2</sub> thin film electrodes are deposited by LPCVD in 3D trenches and on pillar substrates. The energy density, power capability and cycle life of these 3D-structured TiO<sub>2</sub> electrodes are investigated.

## 5.2 Experimental details

### 5.2.1 Thin film deposition

(100) oriented silicon wafers were used as starting material. In order to increase the effective surface area of the Si substrates, etching of trenches with aspect ratios of 1 and 3 and Si pillars with length of 50 μm was conducted using photolithography and RIE, of which the parameters were published before <sup>[25]</sup>. The MOCVD setup used for TiO<sub>2</sub> deposition has been described in detail in chapter 2. In short, a cold wall MOCVD reactor (Aixtron 200 RF) was used, in which the substrate was positioned on a radio frequency heated susceptor. The precursor was titanium(IV) isopropoxide (TTIP), acquired from SAFC-Hitech (United Kingdom). TTIP was delivered in a stainless steel bubbler. This bubbler was thermostated at 25 °C, and the pressure was controlled at 300 mbar. The flow rate of argon through the bubbler to evaporate TTIP was fixed at 100 sccm, while the total flow through the reactor was 1550 sccm. The deposition temperature was varied from 350 to 550 °C. Argon was used as carrier gas. The pressure of the reactor was 5 mbar during the deposition processes.

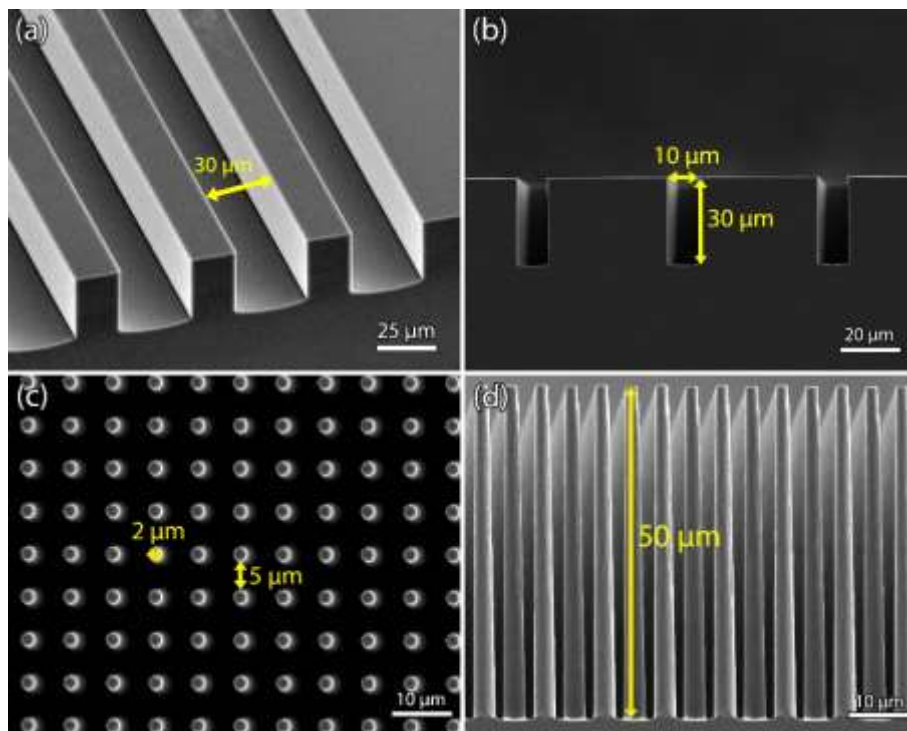


**Figure 5.2** SEM images of tilt view of a 30  $\mu\text{m}$  wide trench (a); cross-section view of a 10  $\mu\text{m}$  wide trench (b); top (c) and cross-section view (d) of a 3D pillar substrate.

TiO<sub>2</sub> films for thickness and surface morphology analyses were deposited onto square silicon substrates with a width of 3 cm. The planar TiO<sub>2</sub> electrodes prepared for electrochemical measurements were deposited on similar substrates covered with an adhesive barrier layer of TiN (30 nm) and a layer of platinum (70 nm) as current collector. To investigate the uniformity of the 3D deposition, TiO<sub>2</sub> films were deposited onto structured silicon substrates, in which trenches with a depth of 30  $\mu\text{m}$  and width of 30 and 10  $\mu\text{m}$  were etched with RIE, as shown in Figure 5.2a and b, respectively. To investigate the electrochemical performance of TiO<sub>2</sub> 3D-electrodes, the films were deposited on silicon into which a pillar structure was etched.

The pillars were coated with 30 nm TiN by ALD, which was used as current collector. The diameter and height of the Si pillars are 2  $\mu\text{m}$  and 50  $\mu\text{m}$ , respectively, and the distance between pillars is 5  $\mu\text{m}$ . SEM images of these pillar substrates are shown in Figure 5.2c and d. The surface enlargement factor ( $A$ ) of the pillar substrate used for the electrochemical investigations is calculated, according to

$$A = 1 + \pi dh / (d + l)^2 \quad (\text{Eq. 5.1})$$

where  $d$  and  $h$  represent the diameter and length of pillars, respectively.  $l$  is the distance between Si pillars.

## 5.2.2 Sample characterization

The thickness and morphology of the TiO<sub>2</sub> thin films were analyzed, using a scanning electron microscope (SEM, Philips/FEI XL 40 FEG). Measurements of Raman spectra were performed on an Olympus BX40 Raman Spectrometer under a backscattering geometry. A 633 nm line of a Helium-Neon laser was taken as the excitation source. The electrochemical measurements were performed in an argon-filled glove box (O<sub>2</sub> and H<sub>2</sub>O < 1 ppm). The samples were positioned in Teflon cells and used as working electrodes. Lithium metal foils were utilized as reference and counter electrodes. The cell was filled with 1 M LiClO<sub>4</sub> in propylene carbonate (Soulbrain MI, United States) as electrolyte. This three-electrode setup was connected to a M2300 galvanostat (Maccor, Tulsa, USA) to perform galvanostatic (dis)charging from 0 to 3 V vs. Li/Li<sup>+</sup> at different current densities: 4, 8, 20, 40 and 80 μA·cm<sup>2</sup> footprint area. All electrochemical tests were carried out at room temperature (~22 °C).

## 5.3 Results and discussion

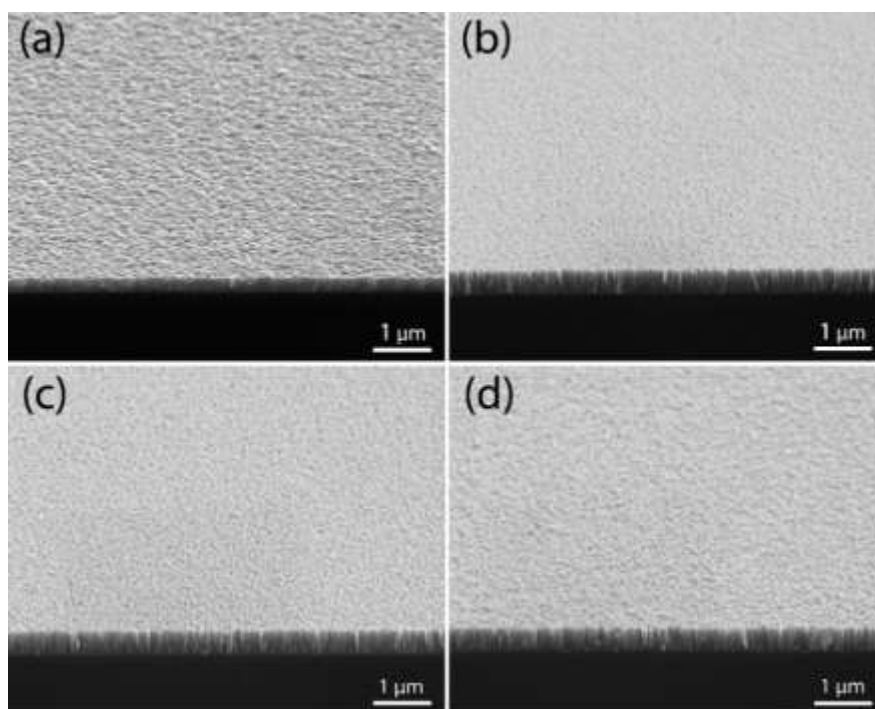


**Figure 5.3** SEM images of TiO<sub>2</sub> films deposited at 350 (a), 400 (b), 450 (c) and 550 (d) °C, respectively.

The SEM images of TiO<sub>2</sub> films deposited at different temperatures are shown in Figure 5.3. It is clear that all films are homogeneous without revealing any cracks or pinholes, which is an apparent advantage of LPCVD to deposit high quality thin films. The simplicity of the

deposition process also permits the processing of large wafer batch sizes. It is interesting to note that compared with films deposited at 350 °C, the films deposited at higher temperatures (450 and 550 °C) are more rough, which may be due to a higher degree of crystallization.

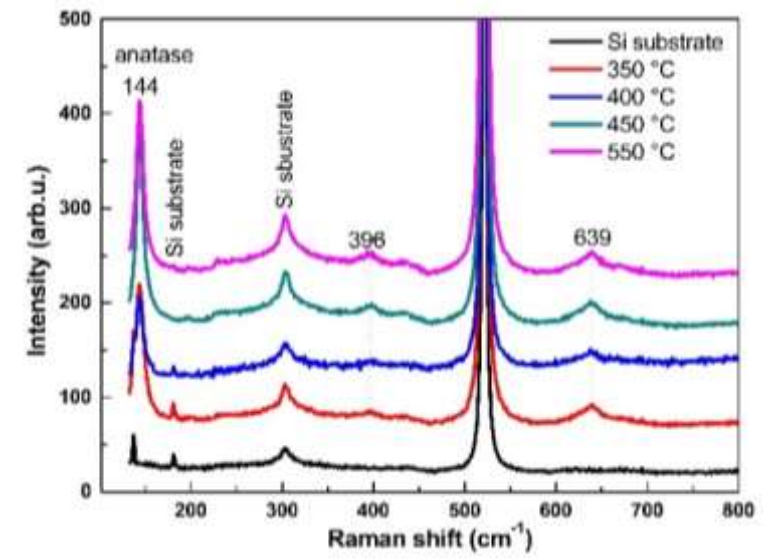


**Figure 5.4** Raman spectra of TiO<sub>2</sub> films deposited at various indicated temperatures.

The Raman spectra of the deposited films are shown in Figure 5.4 as a function of deposition temperature. The Raman spectra of the four films are very similar to each other, showing small peaks at 396 and 639 cm<sup>-1</sup> and a very sharp and intense peak at 144 cm<sup>-1</sup>, which match well with the reported Raman bands for anatase [26]. It can therefore be concluded that all deposited TiO<sub>2</sub> films have the anatase structure.

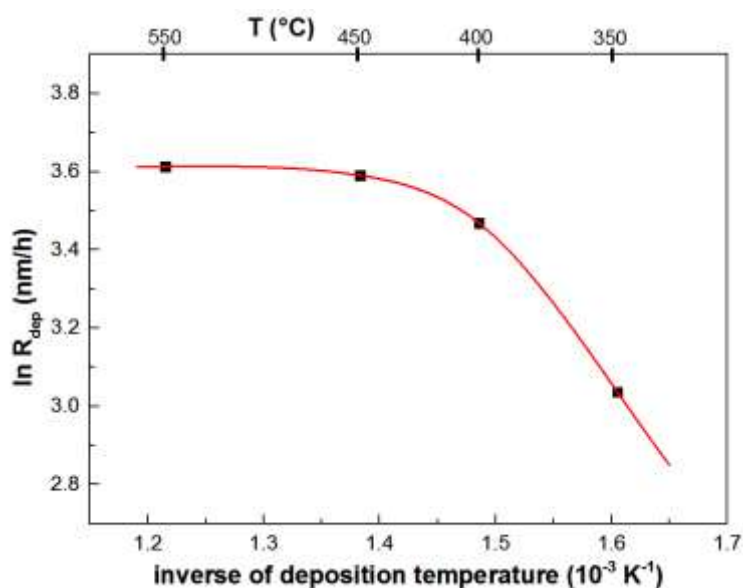


**Figure 5.5** Arrhenius plot for the deposition of planar TiO<sub>2</sub> films.

Figure 5.5 shows the Arrhenius plot of the growth of planar TiO<sub>2</sub> films. It is obvious that the growth of TiO<sub>2</sub> films can be divided into two parts, indicating that there are two different rate-determining processes in these temperature ranges. At high temperatures the deposition rate is only weakly dependent on the deposition temperature. Increasing the deposition temperature from 450 to 550 °C only result in a small increase of growth rate, which indicates that in this temperature range the growth of TiO<sub>2</sub> is a diffusion controlled process [27]. In contrast, in the low-temperature region where the slope in Figure 5.3f is much steeper, the deposition rate is strongly dependent on the temperature. The activation energy calculated from Figure 5.3f is 63.4 kJ/mole, which is relatively high, indicating the deposition of TiO<sub>2</sub> at 350 °C is a kinetically controlled process [27]. Therefore, it is concluded that the deposition rate is limited by diffusive transport in the high-temperature range, while at lower temperatures the deposition is a kinetically controlled process. Within the kinetically controlled region, the growth rate is relatively slow, implying that the chemical conversion of Ti-precursor during the transportation of precursor gas into trenches is slow. Thus, there will still be sufficient Ti-precursor available for the growth of TiO<sub>2</sub> films even towards the bottom of the trench. A uniform deposition at different parts of the 3D substrate can therefore be expected under these conditions.

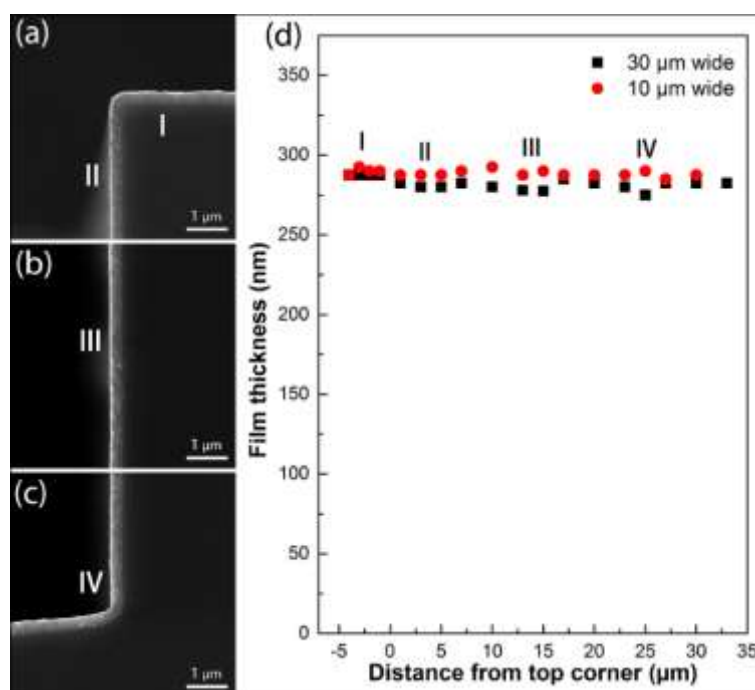


**Figure 5.6** SEM images of deposited TiO<sub>2</sub> films on top (a), middle (b) and bottom (c) part of a 10 μm trench; the development of deposited TiO<sub>2</sub> film thickness as a function of distance from the top surface (d).

Figure 5.6a-c shows a TiO<sub>2</sub> film deposited on different sections (I, II, III and IV) of a 10 μm wide trench. The applied deposition temperature is 350 °C, clearly within the kinetically controlled temperature region. Obviously, the deposited film is very homogeneous from top to bottom. Figure 5.6d shows the development of deposited film thickness as a function of distance from the top surface to the bottom on two trench substrates with different widths, 30 and 10 μm. For both trenches, the films deposited on the top part of the substrates are around 287 nm thick and slightly thinner at bottom, indicating a very high step coverage. Consistent with the prediction from the Arrhenius plot, the film deposited at 350 °C is very uniform.

To show the advantages of 3D-electrodes in improving both the capacity and power performances, TiO<sub>2</sub> thin film electrodes have been deposited on TiN-covered 3D micro-pillar substrates to investigate the electrochemical performances. Figure 5.7a shows the tilt-view of a pillar substrate. Based on geometrical calculations, the surface area enlargement factor is 7.4. Figure 5.7b-d show the film thickness distribution of a TiO<sub>2</sub> film deposited at 350 °C on the surface of Si pillars. A film with layer thickness of 80 nm is deposited on the top surface. At the bottom of the Si pillars, the film thickness is 75 nm. A step coverage of 94% was achieved.

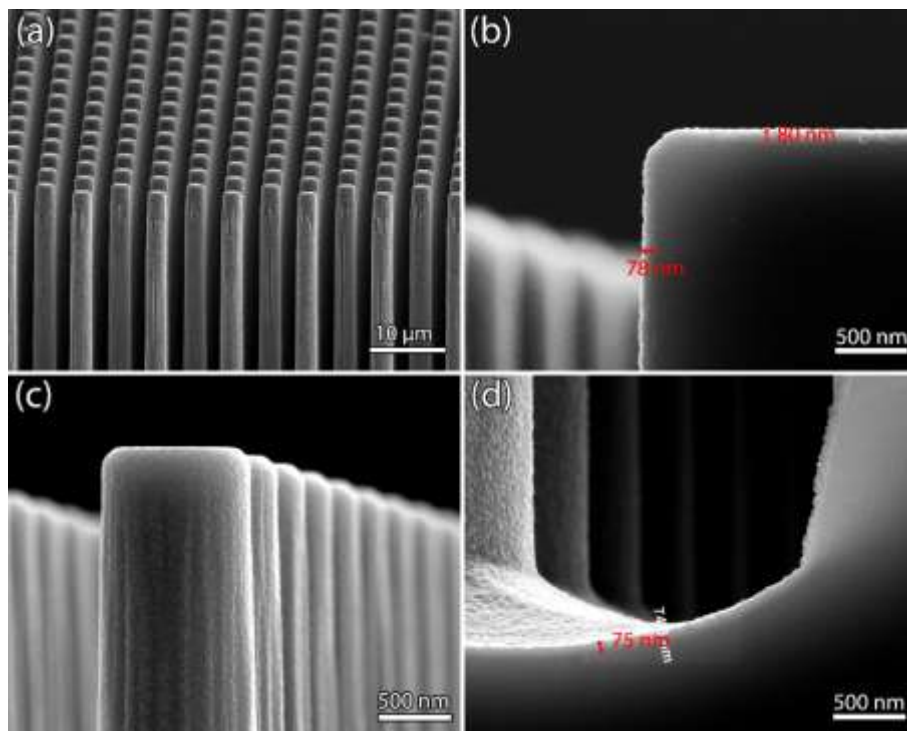


**Figure 5.7** Tilt view of 3D pillar substrates covered by TiO<sub>2</sub> (a), SEM images of deposited TiO<sub>2</sub> film on top (b), surface (c) and bottom (d) part of a 3D pillar substrate.

For LPCVD, the deposited film thickness increases linearly with deposition time<sup>[14]</sup>. The thickness of TiO<sub>2</sub> electrodes can be easily adjusted by changing the deposition time. In order to achieve a high power performance, thin TiO<sub>2</sub> films (40 nm) were chosen as demonstrators. The voltage curves of a planar and a 3D-structured TiO<sub>2</sub> electrode at different (dis)charging current densities are shown in Figure 5.8a and b, respectively. For these electrodes, the typical (dis)charging behavior of anatase TiO<sub>2</sub> is shown. Voltage plateaus at ~1.7 and ~2.0 V were observed in the charge-discharge curves of both planar and 3D TiO<sub>2</sub> film anodes, which can be attributed to the insertion and extraction of Li<sup>+</sup> through Li-poor tetrahedral TiO<sub>2</sub> and the Li-rich orthorhombic Li<sub>0.6</sub>TiO<sub>2</sub>, respectively<sup>[28]</sup>. Although more Li can be accommodated in Li<sub>0.6</sub>TiO<sub>2</sub> to form LiTiO<sub>2</sub> by further two-phase intercalation, the reaction is known to have sluggish kinetics<sup>[17, 29]</sup>. For bulk TiO<sub>2</sub> (> 40 nm), the theoretical capacity is 201 mAh/g (Li<sub>0.6</sub>TiO<sub>2</sub>)<sup>[17, 29]</sup> or 782 mAh·cm<sup>-3</sup>, considering the density of anatase to be 3.89 g·cm<sup>-3</sup>. Therefore, the theoretical area capacity is 78.2 μAh·cm<sup>-2</sup>·μm<sup>-1</sup> for a 1 μm thick TiO<sub>2</sub> film electrode. For a 40 nm planar electrode, 1 C equals to 78.2 × 0.04 = 3.1 μA cm<sup>-2</sup>. So, the (dis)charging current densities of 4 and 80 μA·cm<sup>-2</sup> correspond to a 1.3 and 25.8 C-rate for planar electrodes, respectively. It is noticed that the overpotentials of 3D TiO<sub>2</sub> electrode are smaller than for planar electrodes, especially at high (dis)charging current densities, which indicates that 3D TiO<sub>2</sub> electrode have better power performance.

As shown in Figure 5.8c, at all applied current densities, the 3D electrode shows much higher storage capacities than the planar electrode. For a planar TiO<sub>2</sub> electrode the storage capacity quickly decreases with increasing (dis)charging current. At 80 μA·cm<sup>-2</sup>, the storage capacity has dropped to 4.1 μAh·cm<sup>-2</sup>·μm<sup>-1</sup>, which is less than 14% of the initial capacity. Contrastingly, the storage capacity of the 3D-TiO<sub>2</sub> electrode measured at 80 μA·cm<sup>-2</sup> is 66.2 μAh·cm<sup>-2</sup>·μm<sup>-1</sup>, which is 16 times higher than that of the planar electrode at the same current density. It is also worthwhile to note that even at the highest current density applied (80 μA·cm<sup>-2</sup>), the capacity of the 3D electrode is still twice as high as the storage capacity of the planar electrode at low current densities, *i.e.* at 4 μA·cm<sup>-2</sup>. Obviously, the power performance per footprint area of TiO<sub>2</sub> is significantly improved by the 3D-structure.

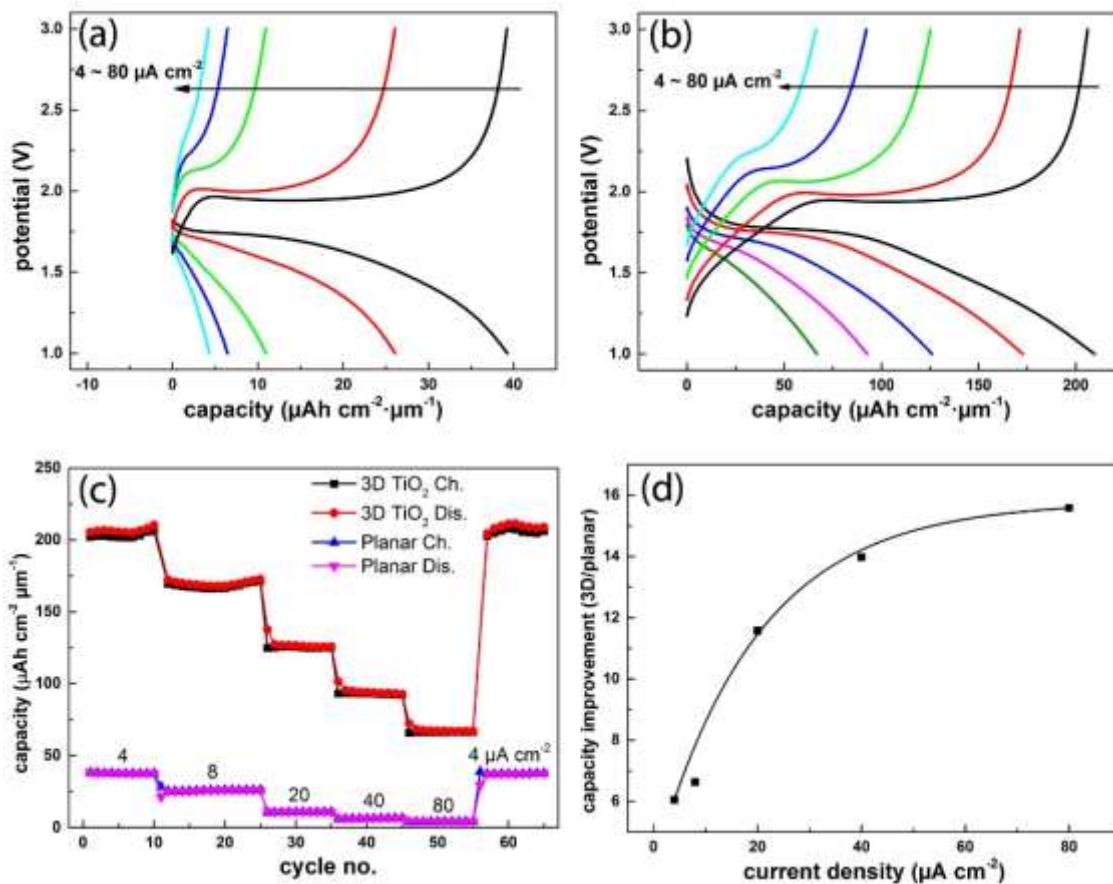


**Figure 5.8** Voltage curves of planar TiO<sub>2</sub> (a) and 3D TiO<sub>2</sub> electrodes (b); Areal capacity of planar and 3D TiO<sub>2</sub> electrodes for charging (Ch.) and discharging (Dis.) at different current densities (c); areal capacity improvement as a function of current densities (d).

For the 3D-electrodes, the surface area is enlarged by 7.4 times, which means that 7.4 times more TiO<sub>2</sub> has been deposited within the same footprint area compared to planar electrodes. Therefore, for 3D-electrodes, a 1 C-rate equals to  $78.2 \times 0.04 \times 7.4 = 23.1 \mu\text{A}\cdot\text{cm}^{-2}$ . For current density of  $80 \mu\text{A}\cdot\text{cm}^{-2}$ , the C-rate for 3D-electrodes is  $80/23.1=3.5$  C. Obviously, under the same output power, the actual C-rate of 3D-electrodes is much lower than for planar-electrodes, resulting in a better power performance. This improvement becomes more pronounced at high output powers. As shows in Figure 5.8d, the storage capacity improvement of 3D electrodes with respect to planar electrodes is more significant as the current density increases. At  $4 \mu\text{A}\cdot\text{cm}^{-2}$ , the storage capacity of the 3D electrode is 6 times higher than that of the planar electrode, which is smaller than the theoretical surface area enlargement of 7.4. As the applied (dis)charge current density increases, the capacity improvement of the 3D electrode becomes higher, even exceeding the surface area enlargement. This further manifests the advantage of the 3D



electrode geometry in improving the power performance, especially at high (dis)charging current densities.

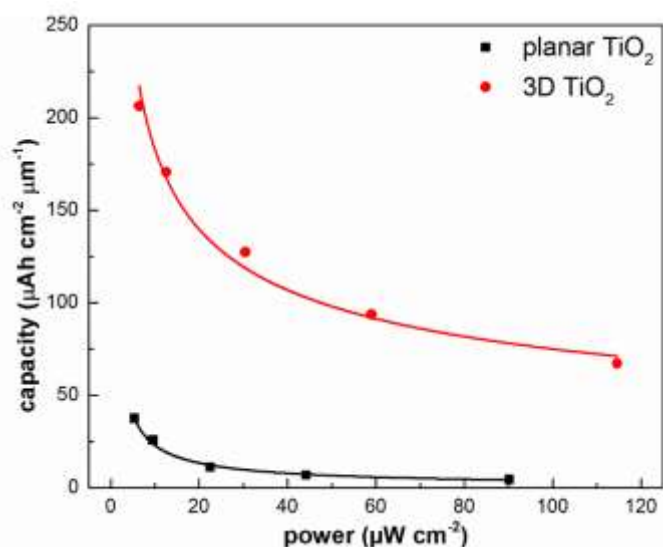


**Figure 5.9** Power and storage capacity comparison of planar and 3D  $\text{TiO}_2$  film electrodes.

Figure 5.9 shows the energy density as a function of power density for the planar and 3D  $\text{TiO}_2$  electrodes. It is clear that at all output powers, the 3D  $\text{TiO}_2$  film electrode reveals a higher capacity. Or alternatively, at a given storage capacity, the 3D electrode delivers a much higher power output. Based on the above discussion of electrochemical results, it is clear that by applying the concept of 3D film electrode, the storage capacity and power performance of thin film electrodes can be improved simultaneously.

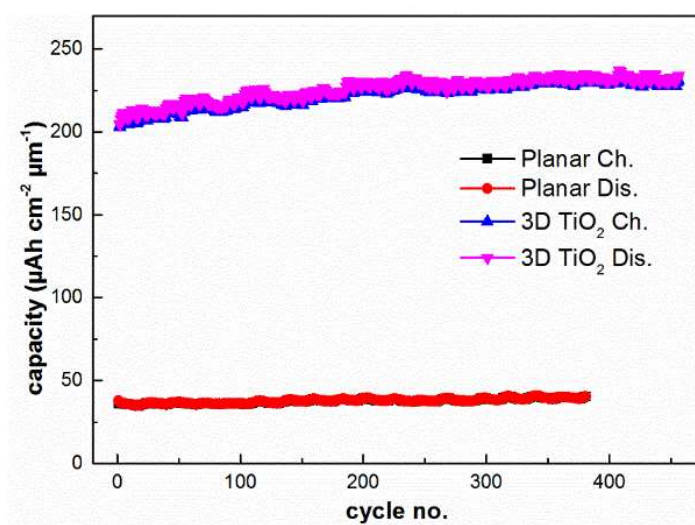


**Figure 5.10** Cycle performances of planar and 3D  $\text{TiO}_2$  film electrodes at a current density of  $4 \mu\text{A cm}^{-2}$ .

The cycling performance of 3D and planar TiO<sub>2</sub> film electrodes is shown in Figure 5.10. The applied current density per footprint area is 4 μA cm<sup>-2</sup>. During the entire cycling test, the 3D TiO<sub>2</sub> anode shows much higher storage capacity than the planar electrode. This is mainly attributed to the enlarged surface area, which allows more TiO<sub>2</sub> loaded per footprint area. What's more, up to 450 cycles, the 3D electrode doesn't show any significant capacity decay, demonstrating excellent cycle performance.

It is interesting to note that the storage capacity of the 3D electrode is slowly increasing during the first 100 cycles. Since the length of the pillars (50 μm) is much bigger than the distance between them (5 μm), some gas bubbles may be trapped at the bottom when the cell was filled with liquid electrolyte, resulting in a (partially) inactive (not wetted) electrode surface at the bottom. Due to the repeatedly expansion and shrinkage of TiO<sub>2</sub> electrodes during the electrochemical tests, the liquid electrolyte may slowly infiltrate to the bottom part, enlarging the active surface area and slowly increasing the storage capacity. Actually, after 100 cycles, the capacity of the 3D-structured TiO<sub>2</sub> electrode is stabilized at 230 μAh·cm<sup>-2</sup>·μm<sup>-1</sup> and this high storage capacity was maintained for more than 350 cycles.

## 5.4 Conclusions

A flexible and accurate 3D fabrication route to create 3D microbatteries electrodes by combining RIE with LPCVD has been demonstrated. It was found that the LPCVD deposition of TiO<sub>2</sub> thin films can be divided into a diffusion-controlled and a kinetically-controlled temperature region. Employing deposition conditions within the kinetically-controlled region, uniform 3D-TiO<sub>2</sub> electrodes have been deposited. Compared with planar TiO<sub>2</sub> electrodes, the storage capacity of 3D-TiO<sub>2</sub> electrodes increased more than 6 times at low current density (4 μA·cm<sup>-2</sup>) and even 16 times at high current density (80 μA·cm<sup>-2</sup>). This high storage capacity is maintained even after 450 cycles. Besides the significant improvement of the storage capacity, the power performance is also improved. At all output power densities, the 3D electrodes manifest a higher storage capacity than planar electrodes. Our results clearly demonstrate the advantages of 3D electrodes for improving both the storage capacity and power performance of thin film batteries.

## References

1. C. Hagleitner, A. Hierlemann, D. Lange, A. Kummer, N. Kerness, O. Brand, and H. Baltes, *Smart single-chip gas sensor microsystem*. *Nature* **414** (2001) 293-296.
2. D.C. Bock, A.C. Marschilok, K.J. Takeuchi, and E.S. Takeuchi, *Batteries used to power implantable biomedical devices*. *Electrochimica Acta* **84** (2012) 155-164.
3. J.F.M. Oudenhoven, R.J.M. Vullers, and R. Schaijk, *A review of the present situation and future developments of micro-batteries for wireless autonomous sensor systems*. *International Journal of Energy Research* **36** (2012) 11391150.
4. M. Zougagh and A. Rios, *Micro-electromechanical sensors in the analytical field*. *Analyst* **134** (2009) 1274-1290.
5. A.C. Fischer, F. Forsberg, M. Lapisa, S.J. Bleiker, G. Stemme, N. Roxhed, and F. Niklaus, *Integrating MEMS and ICs*. *Microsystems & Nanoengineering* **1** (2015) 15005.
6. K. Edström, D. Brandell, T. Gustafsson, and L. Nyholm, *Electrodeposition as a Tool for 3D Microbattery Fabrication*. *The Electrochemical Society interface* **20** (2011) 41-46.
7. P.H.L. Notten, F. Roozeboom, R.A.H. Niessen, and L. Baggetto, *3-D Integrated All-Solid-State Rechargeable Batteries*. *Advanced Materials* **19** (2007).
8. L. Baggetto, H.C.M. Knoop, R.A.H. Niessen, W.M.M. Kessels, and P.H.L. Notten, *3D negative electrode stacks for integrated all-solid-state lithium-ion microbatteries*. *Journal of Materials Chemistry* **20** (2010) 3703-3708.
9. J.W. Long, B. Dunn, D.R. Rolison, and H.S. White, *Three-dimensional battery architectures*. *Chem Rev* **104** (2004) 4463-92.
10. J.F.M. Oudenhoven, L. Baggetto, and P.H.L. Notten, *All-Solid-State Lithium-Ion Microbatteries: A Review of Various Three-Dimensional Concepts*. *Advanced Energy Materials* **1** (2011) 10-33.
11. S. Ferrari, M. Loveridge, S.D. Beattie, M. Jahn, R.J. Dashwood, and R. Bhagat, *Latest advances in the manufacturing of 3D rechargeable lithium microbatteries*. *Journal of Power Sources* **286** (2015) 25-46.
12. H.L. Ning, J.H. Pikul, R.Y. Zhang, X.J. Li, S. Xu, J.J. Wang, J.A. Rogers, W.P. King, and P.V. Braun, *Holographic patterning of high-performance on-chip 3D lithium-ion microbatteries*. *Proceedings of the National Academy of Sciences of the United States of America* **112** (2015) 6573-6578.
13. G. Kim, S. Jeong, J.-H. Shin, J. Cho, and H. Lee, *3D Amorphous Silicon on Nanopillar Copper Electrodes as Anodes for High-Rate Lithium-Ion Batteries*. *ACS Nano* **8** (2014) 1907-1912.
14. J. Xie, J.F.M. Oudenhoven, P.P.R.M.L. Harks, D.J. Li, and P.H.L. Notten, *Chemical Vapor Deposition of Lithium Phosphate Thin-Films for 3D All-Solid-State Li-Ion Batteries*. *Journal of the Electrochemical Society* **162** (2015) A249-A254.
15. Y. Wang, B. Liu, Q. Li, S. Cartmell, S. Ferrara, Z.D. Deng, and J. Xiao, *Lithium and lithium ion batteries for applications in microelectronic devices: A review*. *Journal of Power Sources* **286** (2015) 330-345.
16. M.P. Cantao, J.I. Cisneros, and R.M. Torresi, *Kinetic-Study of Lithium Electroinsertion in Titanium-Oxide Thin-Films*. *Journal of Physical Chemistry* **98** (1994) 4865-4869.
17. W.J. Borghols, D. Lutzenkirchen-Hecht, U. Haake, E.R. van Eck, F.M. Mulder, and M. Wagemaker, *The electronic structure and ionic diffusion of nanoscale LiTiO<sub>2</sub> anatase*. *Phys Chem Chem Phys* **11** (2009) 5742-5748.

18. S.K. Cheah, E. Perre, M. Rooth, M. Fondell, A. Harsta, L. Nyholm, M. Boman, T. Gustafsson, J. Lu, P. Simon, and K. Edstrom, *Self-Supported Three-Dimensional Nanoelectrodes for Microbattery Applications*. *Nano Letters* **9** (2009) 3230-3233.
19. W. Wang, M. Tian, A. Abdulagatov, S.M. George, Y.-C. Lee, and R. Yang, *Three-Dimensional Ni/TiO<sub>2</sub> Nanowire Network for High Areal Capacity Lithium Ion Microbattery Applications*. *Nano Letters* **12** (2012) 655-660.
20. J. Xie, P.-P.R.M.L. Harks, D. Li, L.H.J. Raijmakers, and P.H.L. Notten, *Planar and 3D deposition of Li<sub>4</sub>Ti<sub>5</sub>O<sub>12</sub> thin film electrodes by MOCVD*. *Solid State Ionics* **287** (2016) 83-88.
21. S. Moitzheim, C.S. Nimisha, D. Shaoren, J.C. Daire, C. Detavernier, and P.M. Vereecken, *Nanostructured TiO<sub>2</sub> /carbon nanosheet hybrid electrode for high-rate thin-film lithium-ion batteries*. *Nanotechnology* **25** (2014) 504008.
22. W. Wei, G. Oltean, C.-W. Tai, K. Edstrom, F. Bjorefors, and L. Nyholm, *High energy and power density TiO<sub>2</sub> nanotube electrodes for 3D Li-ion microbatteries*. *Journal of Materials Chemistry A* **1** (2013) 8160-8169.
23. D.P. Singh, A. George, R.V. Kumar, J.E. ten Elshof, and M. Wagemaker, *Nanostructured TiO<sub>2</sub> Anatase Micropatterned Three-Dimensional Electrodes for High-Performance Li-Ion Batteries*. *The Journal of Physical Chemistry C* **117** (2013) 19809-19815.
24. J.F.M. Oudenhoven, T.v. Dongen, R.A.H. Niessen, M.H.J.M.d. Croon, and P.H.L. Notten, *Low-Pressure Chemical Vapor Deposition of LiCoO<sub>2</sub> Thin Films: A Systematic Investigation of the Deposition Parameters*. *Journal of The Electrochemical Society* **156** (2009) D169.
25. F. Roozeboom, R.J.G. Elfrink, T. Rijks, J. Verhoeven, A. Kemmeren, J. van den Meerakker, Spie, and Spie, *High-density, low-loss MOS capacitors for integrated RF decoupling*, in *2001 International Symposium on Microelectronics, Proceedings*. 2001, Spie-Int Soc Optical Engineering: Bellingham. p. 477-483.
26. T. Ohsaka, F. Izumi, and Y. Fujiki, *Raman-Spectrum of Anatase, TiO<sub>2</sub>*. *Journal of Raman Spectroscopy* **7** (1978) 321-324.
27. A.C. Jones and M.L. Hitchman, *Chemical Vapour Deposition: Precursors, Processes and Applications*, Royal Society of Chemistry, Cambridge U.K. (2009).
28. J.L. Cheng, B. Wang, H.L.L. Xin, C. Kim, F.D. Nie, X.D. Li, G.C. Yang, and H. Huang, *Conformal coating of TiO<sub>2</sub> nanorods on a 3-D CNT scaffold by using a CNT film as a nanoreactor: a free-standing and binder-free Li-ion anode*. *Journal of Materials Chemistry A* **2** (2014) 2701.
29. M. Wagemaker, W.J. Borghols, and F.M. Mulder, *Large Impact of Particle Size on Insertion Reactions. A Case for Anatase Li<sub>x</sub>TiO<sub>2</sub>*. *Journal of the American Chemical Society* **129** (2007) 4323-4327.



# Chapter 6 Modelling TiO<sub>2</sub> Deep Trench Deposition Process

## ***Abstract***

3D microbatteries are indispensable to cope with the increasing energy demand of autonomous smart devices. To synthesize 3D microbatteries, step-conformal deposition of thin films into 3D-substrates is vital, and low pressure chemical vapor deposition (LPCVD) is a technique that is capable of achieving this. In this work, the 3D-deposition of TiO<sub>2</sub> is investigated. It is shown that the growth of anatase TiO<sub>2</sub> can be characterized by two rate-determining processes. In the diffusion-controlled temperature region, the TiO<sub>2</sub> films deposited into 3D-substrates lack step-conformity. In contrast, in the kinetically-controlled temperature region, uniform films were deposited inside these micro-structures. To understand and improve the LPCVD deposition process in more detail, the experimental results were simulated using a Markov chain Monte-Carlo (MCMC) model. Good agreement between the model and experiments was achieved in all cases. It was found that the deposition probability is low in the kinetically-controlled deposition region, while this probability was found to be high in the diffusion-controlled region. It is also shown that the reflections of precursor molecules inside the trenches play an important role in achieving homogeneous 3D deposition. To show the strength of the MCMC model, the optimized deposition parameters are applied to predict the film thickness profiles in narrower micro-structures.

## 6.1 Introduction

TiO<sub>2</sub> has been identified as a promising electrode material for Li-ion batteries as it is safe, non-toxic, readily available and has a high theoretical volumetric storage capacity (1303 mAh/cm<sup>3</sup>). However, the poor conductivity and slow diffusion rate of Li<sup>+</sup> in TiO<sub>2</sub> has restricted the rate capability and storage capacity of TiO<sub>2</sub> [1, 2]. A straightforward solution to overcome this limitation is to decrease the film thickness. However, nano-sizing the film thickness leads to a significant capacity reduction. Employing 3D-structured TiO<sub>2</sub> thin film electrodes is, however, a promising method to solve this dilemma [3-5].

Thin films of TiO<sub>2</sub> have been deposited by many techniques, such as sputtering [1], pulsed laser deposition [6] and e-beam evaporation [7]. Because of shadow effects, these methods are hardly suitable for 3D deposition. Atomic layer deposition (ALD) and LPCVD are two methods that can deposit step-conformal thin films on highly structured substrates. Unfortunately, the ALD method is relatively slow [8] and therefore rather unpractical for the deposition of battery materials. For LPCVD, the mean free path between gas molecule collisions is large compared to the substrate dimensions, enabling step-conformal deposition of high quality layers on high aspect ratio structures. Apart from the simplicity of LPCVD deposition processes, processing large wafer batches is another interesting asset, facilitating future industrialization. In recent years, LPCVD has received considerable attention as a way to produce 3D micro-structured solid-state batteries with significantly improved volumetric capacity and rate capability [5, 9, 10].

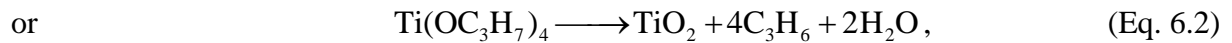
In order to deposit high-quality 3D-structured TiO<sub>2</sub> electrodes, it is required that these films are highly uniform and free of pinholes and cracks. For that reason, a lot of efforts have been spent in optimizing the deposition process. The ability to accurately predict the thickness profiles of the deposited thin films is highly valuable in decreasing the complexity of the LPCVD optimization process. Although a number of deposition models have been proposed for various applications [11-14], no simulation results on the deposition of TiO<sub>2</sub> have been reported in the literature up to now. Monte-Carlo methods are commonly applied tools to simulate the flow of low-pressure gases, which is typical for LPCVD processes [15, 16].

In the present study, titanium isopropoxide (TTIP) is used as Ti-precursor. Because oxygen is already included in TTIP, no addition reactants, such as O<sub>2</sub> or H<sub>2</sub>O, are required to be added in the deposition process. Therefore, only one precursor gas (TTIP) is carried into the reactor by Ar, which simplifies the deposition process. Furthermore, the deposition process has been

performed at low pressure. Consequently, molecular collisions in the gas phase and turbulence of the gas flow can be neglected <sup>[17]</sup>. The as-denoted Markov chain Monte-Carlo (MCMC) method is therefore very well suited to simulate the 3D-deposition process of TiO<sub>2</sub>. In the first part of this paper, the influence of experimental conditions on the deposition of TiO<sub>2</sub> in 3D-structures will be investigated. In the second part, the MCMC model will be introduced and validated by the experimental results. In addition, the predictive value of the optimized MCMC-model will be highlighted for other 3D-microstructures.

## 6.2 Experimental details

The deposition setup and applied deposition parameters have already been introduced in section 5.2. Since oxygen is already included in the Ti-precursor (TTIP), there is no additional supply of oxygen required during the deposition process. Examples of deposition reactions are given as follows <sup>[18]</sup>:



which can be generalized to be



The (100) oriented silicon wafers were used as starting material. Etching of trenches was conducted using photolithography and reactive ion etching, for which the experimental conditions has been published before <sup>[19]</sup>. After deposition of the TiO<sub>2</sub> films, the 3D-substrates can easily be cleaved along the mono-crystalline planes of Si to reveal cross-sections, which is convenient to investigate the thickness profiles of the deposited TiO<sub>2</sub> films by scanning electron microscope (SEM, Philips/FEI XL 40 FEG). The cross-sections of the trenches etched in the Si substrates with a depth of 30 μm and a width of 30 and 10 μm are shown in Figure 6.1a and b, respectively. Based on the SEM images, the film thickness along the trench depth is quantified, *i.e.* the thickness of the deposited TiO<sub>2</sub> films was measured as a function of position along the trenches. To determine the crystal structure of the deposited TiO<sub>2</sub> films, Raman spectra were measured using an Olympus BX40 Raman Spectrometer under a backscattering geometry. The 633 nm line of a Helium-Neon laser was taken as excitation source.



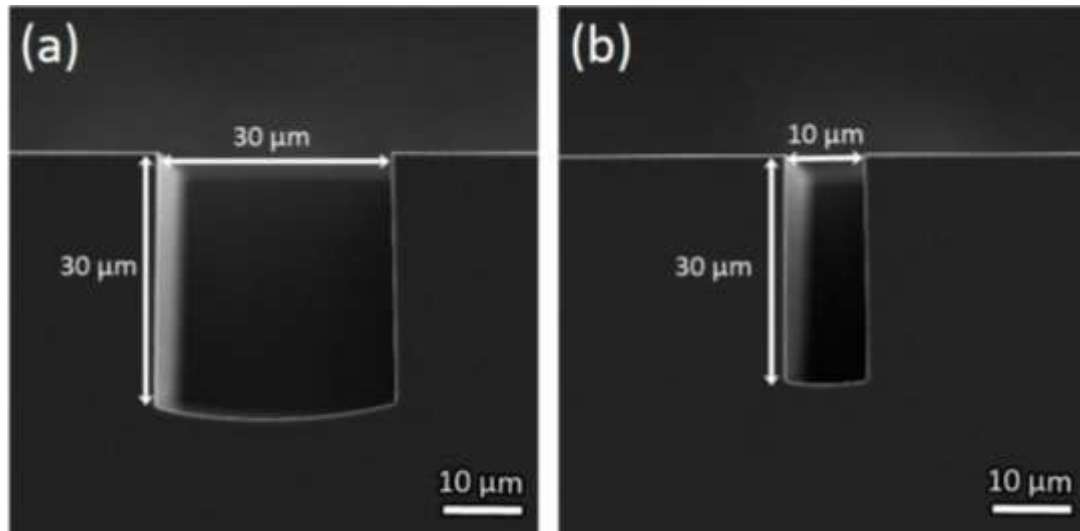


**Figure 6.1** Trenches with depth of 30  $\mu\text{m}$ , width of 30  $\mu\text{m}$  (a) and 10  $\mu\text{m}$  (b)

### 6.3 Deposition results

The surface morphology, Raman spectra and Arrhenius plot of planar  $\text{TiO}_2$  deposition have already been introduced in section 5.2.1. In this section, we focused on the 3D deposition.  $\text{TiO}_2$  films deposited into 30  $\mu\text{m}$  wide trench is shown in Figure 6.2. Consistent with the prediction of Arrhenius plot, at kinetically-controlled temperature (350  $^\circ\text{C}$ ), uniform film is deposited throughout the 30  $\mu\text{m}$  wide trench. The bottom film thickness is 230 nm, only slightly thinner than the top surface (250 nm), which presents a very high step-coverage. Figure 6.2b-f show different parts of the film deposited at 400  $^\circ\text{C}$ , which is within the diffusion-controlled region. Due to the higher growth rate at 400  $^\circ\text{C}$ , the film thickness on the top surface is 390 nm, which is much thicker than the film deposited at 350  $^\circ\text{C}$ . However, the film thickness instantly drops after entering into the trench and decreases continuously as the depth increases. At the bottom, the film thickness decreases to 80 nm, which is much thinner than that for the film deposited at 350  $^\circ\text{C}$ . The films deposited at 450 and 550  $^\circ\text{C}$  shows similar results as the film deposited at 400  $^\circ\text{C}$ . The film thickness inside the trench keeps decreasing as the distance from the top surface increases, except a slightly higher film thickness on the top surface.

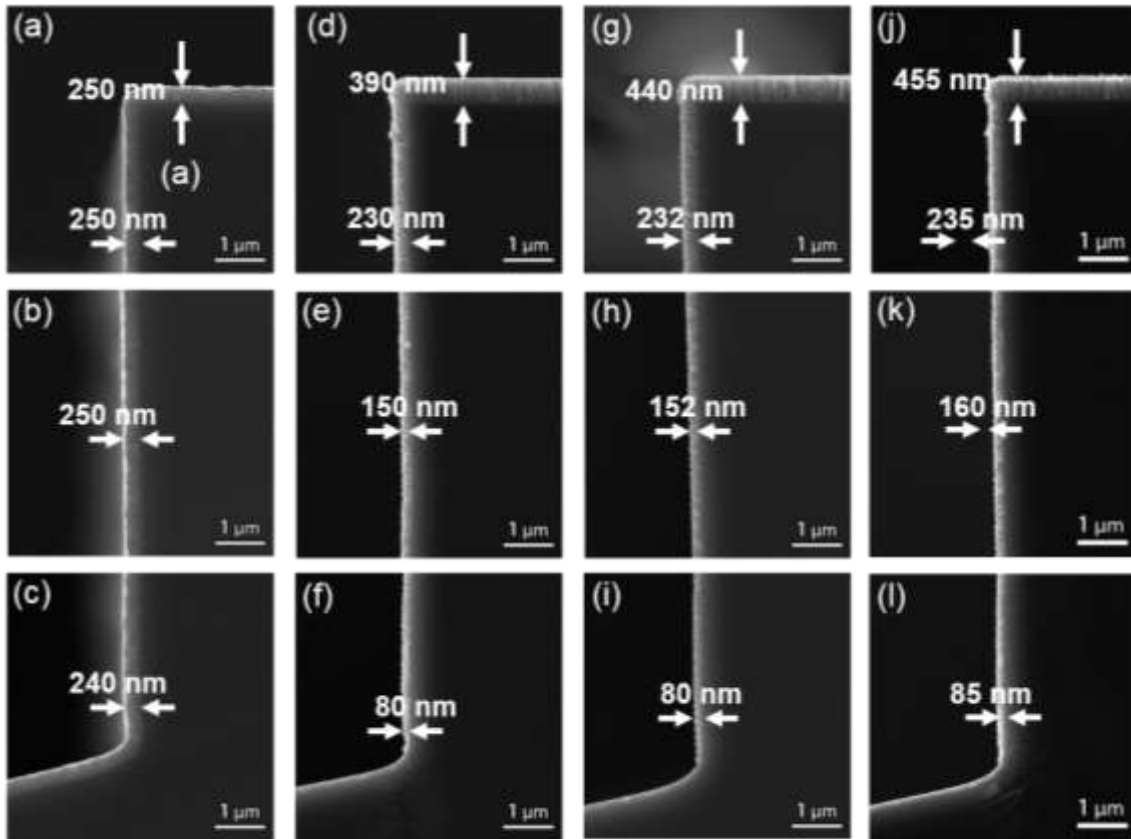


**Figure 6.2** SEM images of deposited  $\text{TiO}_2$  film on different parts of a  $30\ \mu\text{m}$  wide trench. Film deposited at  $350\ ^\circ\text{C}$  (a), (b) and (c);  $400\ ^\circ\text{C}$  (d), (e) and (f);  $450\ ^\circ\text{C}$  (g), (h) and (i);  $550\ ^\circ\text{C}$  (j), (k) and (l). Top part of trench (a), (d), (g) and (j), middle (b), (e), (h) and (k), bottom (c), (f), (i) and (l)

Similar results are observed for  $10\ \mu\text{m}$  width trench, as shown in Figure 6.3. The film deposited at  $350\ ^\circ\text{C}$  is still homogeneously distributed throughout the trench. For the film deposited at the temperature within mass-transfer controlled region ( $400$ ,  $450$  and  $550\ ^\circ\text{C}$ ), the film thickness drops immediately after entering into the trench substrate and keep decreasing to the bottom. Notably, the film thickness inside the trench decrease more pronouncedly than that in  $30\ \mu\text{m}$  wide trench. At the bottom, the film is nearly invisible. For narrower trench, less space is left for the precursor gas to diffuse into the trench, making inhomogeneity even worse.

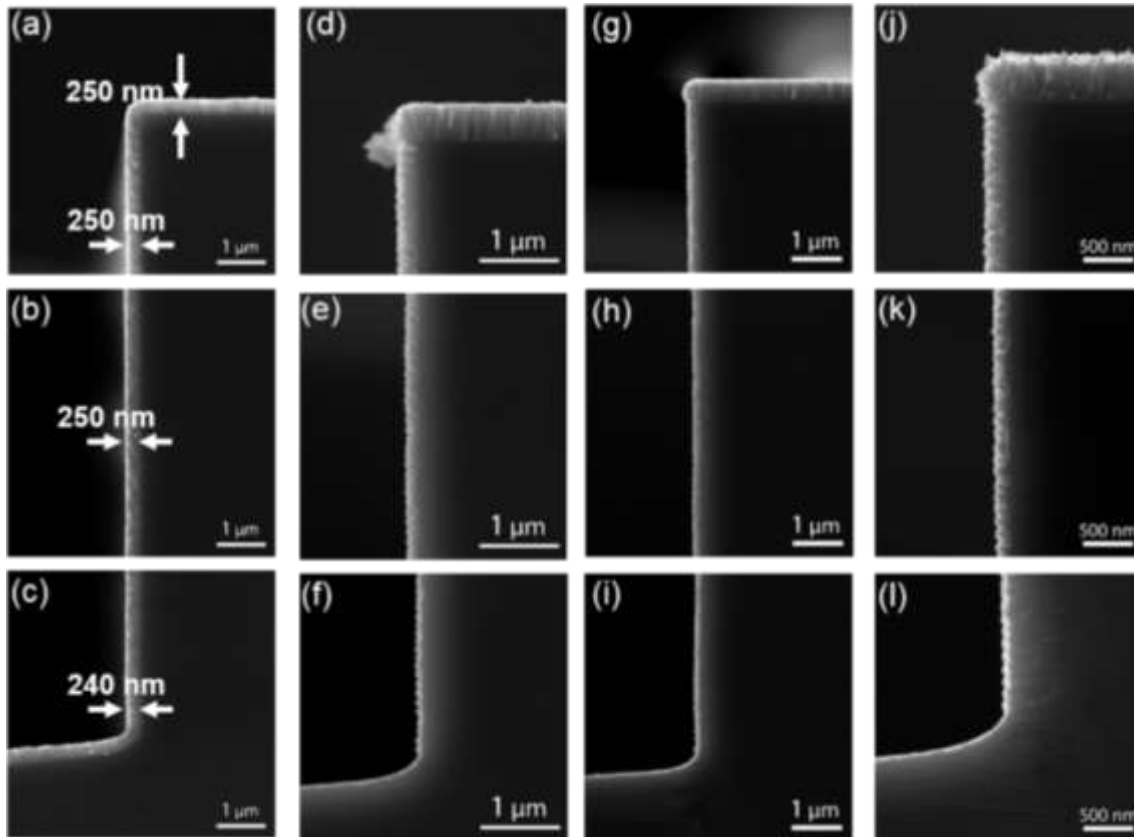


**Figure 6.3** SEM images of deposited  $\text{TiO}_2$  film on different parts of a  $30\ \mu\text{m}$  wide trench. Film deposited at  $350\ ^\circ\text{C}$  (a), (b) and (c);  $400\ ^\circ\text{C}$  (d), (e) and (f);  $450\ ^\circ\text{C}$  (g), (h) and (i);  $550\ ^\circ\text{C}$  (j), (k) and (l). Top part of trench (a), (d), (g) and (j), middle (b), (e), (h) and (k), bottom (c), (f), (i) and (l)

All 3D-deposition results are summarized in Figure 6.4. Top surface part corresponds to negative values of the trench depth. For the films deposited at  $350\ ^\circ\text{C}$  (Figure 6.4a), well within the kinetically controlled temperature region of Figure 5.5, a highly homogeneous distribution from the surface to the bottom of the trenches can be found for both the  $30\ \mu\text{m}$  (black symbols) and  $10\ \mu\text{m}$  (red symbols) wide structures. In contrast, the films deposited in the mass-transport controlled temperature region (Figure 6.4b-d) reveal a very strong depth dependence. The deposition rate at the surface has increased significantly in comparison to the kinetically controlled case, but the film thickness immediately drops inside the trenches and continues to decrease further towards the bottom of the trenches. It is also noted that for these latter inhomogeneous conditions, the films deposited into the  $30\ \mu\text{m}$  trenches (black symbols) always have a higher step-coverage than for the  $10\ \mu\text{m}$  trenches (red symbols), indicating that the geometry also has a strong effect on the uniformity of the deposited films.

Based on the above experimental results, it is clear that both the deposition temperature and the substrate geometry influence the uniformity of the deposited thin films. In order to get more insight into the mechanism of the LPCVD deposition process and to further optimize the deposition parameters for 3D-deposition processes, a MCMC model has been developed, which will be described below.

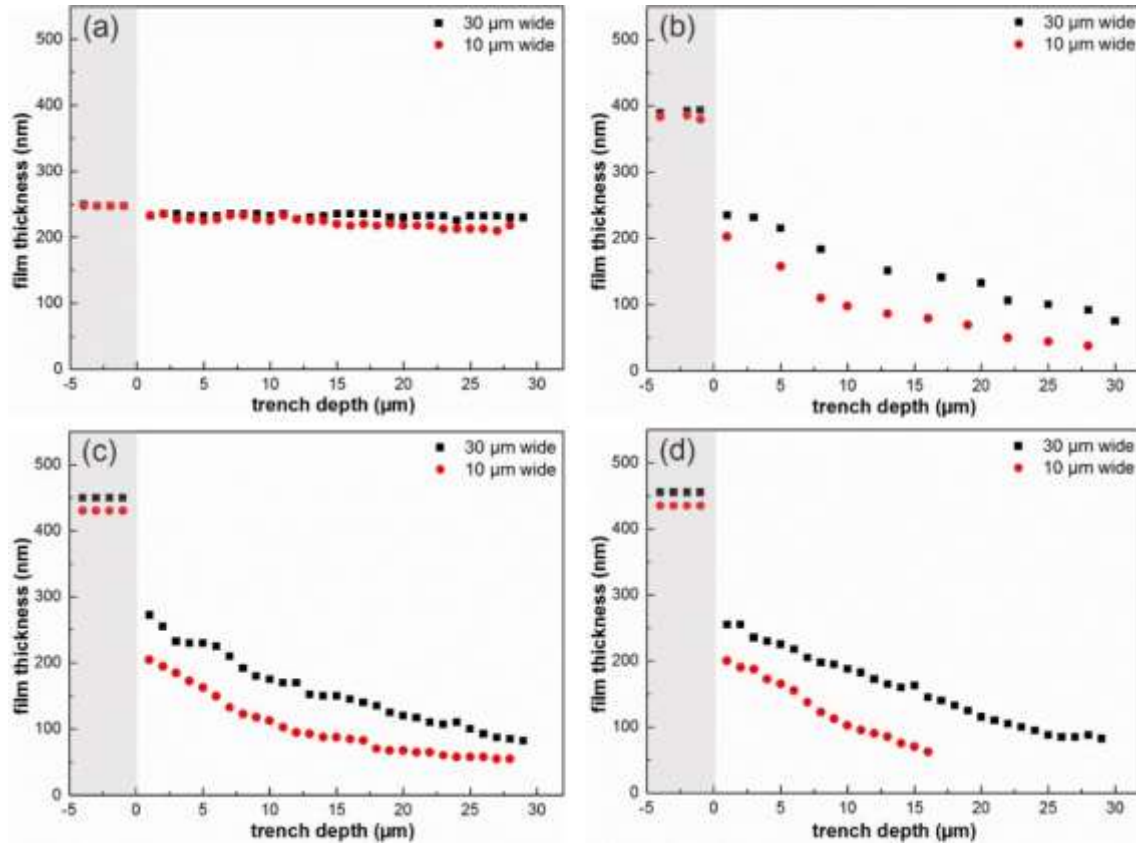


**Figure 6.4** Digitized film thickness evolution as a function of distance from top surface.

## 6.4 Theoretical considerations

Basically, the Monte-Carlo approach of LPCVD deposition of  $\text{TiO}_2$  is modeling a large number of independent precursor trajectories coupled with the chemical decomposition reaction at the substrate surface. The deposition of  $\text{TiO}_2$  (Eq. 6.3) can be presented as



where DR represents a precursor molecule, which is composed of a deposition part (D) and a residual part (R). During such a deposition event, DR from the gas phase collides with the substrate surface, depositing D at the substrate surface and releasing R to the gas phase. This

event happens with probability  $P_d$ . An alternative event is that DR is reflected away from the surface as a “hard ball” and continues its pathway in the gas phase.  $P_d$  is also known as the reactive sticking coefficient, which was reported to be dependent on the deposition temperature [11]. To perform Monte-Carlo simulations, the system has to be accurately defined first, including the dimensions of the micro-structured substrate, distribution of the incoming molecules as well as the precursor concentration at the substrate surface. These definitions will be described in the following two subsections, ultimately resulting in a simulation process.

#### 6.4.1 System definitions

To model the particle movements inside trenches, a coordinate system needs to be defined. Figure 6.6 shows the orientation of the  $x$ ,  $y$  and  $z$  axes, under the condition that the  $x$  axis is perpendicular to the trench walls, the  $y$  axis is directed along the trenches and the  $z$  axis points towards the bottom of the trenches. The  $xy$  plane at the surface ( $z = 0$ ) is defined as the source plane (S), where all precursor molecules (DR) originate from.

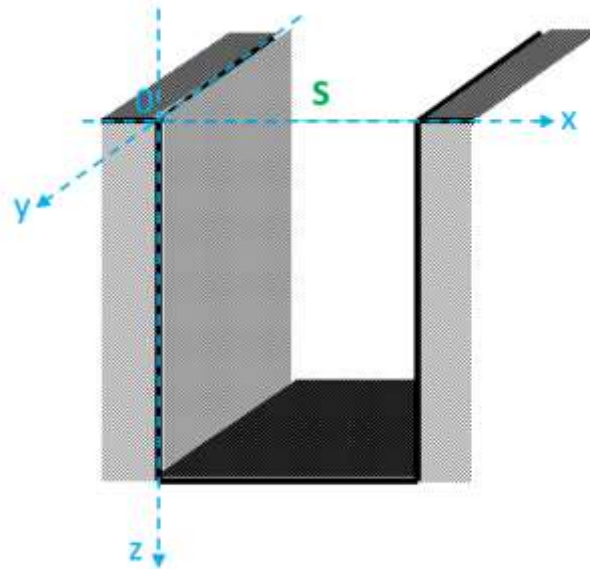


**Figure 6.5** Coordinate system of a trench.

The modeling of trajectory starts when particles cross the source plane  $S$ . The initial distribution of precursor molecules has a large influence on the deposited profiles estimated in deep trenches. Therefore, modeling of the initial distribution of precursor molecules (DR) is critical for the simulation procedure. The distribution of DR molecules includes two parts:

distribution of the entrance positions and the angular distribution of the DR molecules, *i.e.* for a DR molecule, both the position and its moving direction need to be modeled.

In the deposition process, the size of reactor chamber where the gas-phase resides is at least three orders of magnitude larger than the dimension of the trenches. Therefore, distribution of the molecules in the gas phase is similar to the usual gases, *i.e.* particles distribute uniformly and fly in all directions without any preference. Considering these facts, the initial points  $(x, y, z)$  are assumed to be uniformly distributed on the source plane  $S$ , *i.e.*  $x$  and  $y$  are uniformly distributed on the source plane  $S$ , while  $z = 0$ .

After determining the distribution of entrance position of source molecules (DR), the angular distribution of DR molecules is modeled in the following way. Figure 6.6 shows a spherical coordinate system, which is characterized by the radial distance  $r$ , the azimuthal angle  $0 \leq \varphi \leq 2\pi$  and polar angle  $0 \leq \theta \leq \pi/2$ . The relation between the spherical and Cartesian coordinate systems can be described by

$$x = r \sin(\theta) \cos(\varphi), \quad y = r \sin(\theta) \sin(\varphi), \quad z = r \cos(\theta). \quad (\text{Eq. 6.5})$$

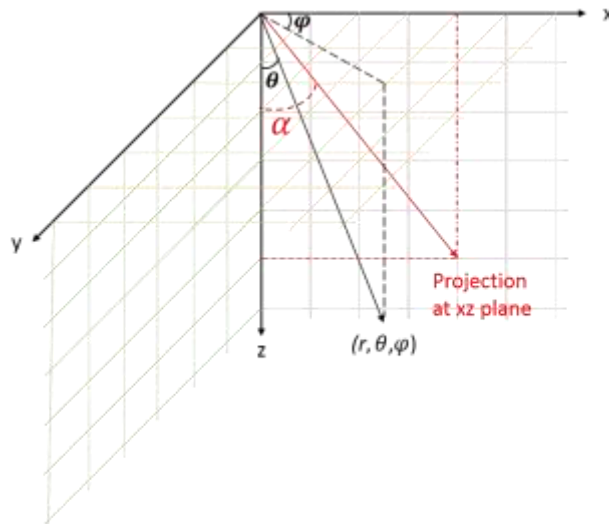


**Figure 6.6** Definition of the spherical coordinate system.

In the LPCVD deposition process, the gas flow is a Lambertian flux, which means the incoming molecules come from any direction and obey the probability distribution<sup>[20, 21]</sup>

$$dP = \frac{1}{\pi} \cos(\theta) d\Omega. \quad (\text{Eq. 6.6})$$

where  $P$  is distribution probability and  $d\Omega$  is differential solid angle <sup>[22]</sup>, which can be expressed via polar and azimuthal angles as

$$d\Omega = \sin(\theta) d\theta d\varphi. \quad (\text{Eq. 6.7})$$

Combining Eq. 6.6 and 6.7 results in

$$dP = \frac{1}{\pi} \cos(\theta) \sin(\theta) d\theta d\varphi = d \cos^2(\theta) d \frac{\varphi}{2\pi}. \quad (\text{Eq. 6.8})$$

Integrating Eq. 6.8, a distribution function of  $\theta$  in the form  $F(\theta) = 1 - \cos^2(\theta)$  is obtained in which  $\cos^2(\theta)$  is uniformly distributed between 0 and 1. Application of the inverse transform algorithm leads to the following modeling procedure: angle  $\varphi$  is uniformly distributed in interval  $[0, 2\pi]$ <sup>[23]</sup>, while angle  $\theta$  is independent and distributed according to  $\cos(\theta) = U^{1/2}$ , where  $U$  is uniformly distributed in interval  $[0,1]$ <sup>[16]</sup>. Therefore, the modeling formulas are

$$\varphi = 2\pi V, \quad \theta = \arccos(U^{1/2}), \quad (\text{Eq. 6.9})$$

where  $V$  and  $U$  are independent random variables, uniformly distributed in interval  $[0,1]$ .

In the present model, it is assumed that the film thickness along the  $y$ -axis is constant, which means that any point  $(x, y, z)$  with the same coordinates of  $x$  and  $z$ , the deposited film thickness is the same. Therefore, the 3D thickness profiles can be projected into the  $xz$  plane. Now consider a point with coordinates  $(x, y, z)$ , then a pair of coordinates  $(x, z)$  defines the projection of point  $(x, y, z)$  onto the  $xz$  plane. Considering a vector with the origin at  $(0, 0)$  and endpoint  $(x, z)$ , the angle between this vector and the coordinate axis  $z$  is defined to be the incoming angle ( $\alpha$ ), as shown in Figure 6.6. Applying the definition that  $\cos(\alpha) = z / \sqrt{x^2 + z^2}$  and combining this expression with Eq. 6.5 leads to

$$\alpha = \arccos(\cos(\theta) / \sqrt{\sin^2(\theta) \cos^2(\varphi) + \cos^2(\theta)}). \quad (\text{Eq. 6.10})$$

where  $\varphi$  and  $\theta$  are modeled according to Eq. 6.9.

In the following sections, the trench structure was projected to the  $xz$  plane and variations of film thickness along dimension  $y$  are not considered, since it is assumed that the deposited films are homogeneously distributed along  $y$ . The 2D projection of a trench are defined in Figure 6.7. Specific parts of the geometry are indicated: O is the trench opening, T<sub>1</sub> and T<sub>2</sub> are top parts

of the sample on the left and right side of the opening,  $W_1$  and  $W_2$  are two opposing walls,  $B$  corresponds to the bottom of the trench. The depth and width of the trench denoted as  $H$  and  $L$  ( $\mu\text{m}$ ), respectively. Parameter  $\Delta L$  ( $\mu\text{m}$ ) denotes the width of each top flat area. Precursor molecules come from the bulk of the gas phase. Note that zero of the coordinate system is aligned with left corner of the opening, indicated as 0 in Figure 6.6. Therefore, in this coordinate system, 6 specific parts of the system are defined as

$$\begin{aligned} O &= \{(x, z) : 0 \leq x \leq L, z = 0\}, & B &= \{(x, z) : 0 \leq x \leq L, z = H\}, \\ T_1 &= \{(x, z) : -\Delta L \leq x \leq 0, z = 0\}, & W_1 &= \{(x, z) : x = 0, 0 \leq z \leq H\}, \\ T_2 &= \{(x, z) : L \leq x \leq L + \Delta L, z = 0\}, & W_2 &= \{(x, z) : x = L, 0 \leq z \leq H\}. \end{aligned}$$

The source plane  $xy$  where precursor molecules are coming from (as illustrated in Figure 6.6) after projecting to  $xz$  plane becomes a source line, which combines  $T_1$ ,  $O$  and  $T_2$ , *i.e.*  $S = T_1 + O + T_2$ . Trajectories of the incoming molecules will be traced starting from crossing line  $S$ ,  $S = \{(x, z) : -\Delta L \leq x \leq L + \Delta L, z = 0\}$ .

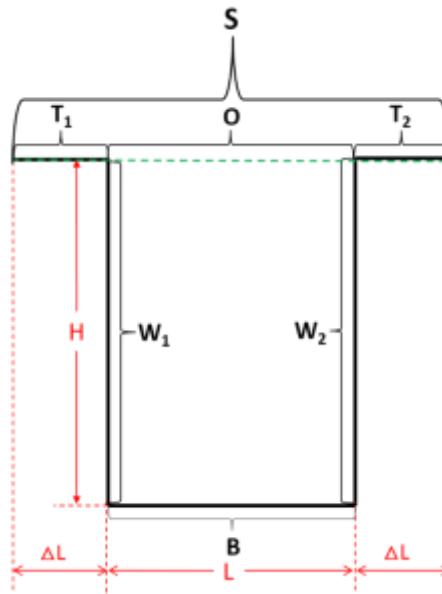


**Figure 6.7** Geometrical parameters of a trench.

The collisions between precursor molecules and the substrate surface are modeled according to the rule of absolutely elastic collision (hard balls): angle of incidence equals the angle of reflection. If a DR molecule hits the top flat surfaces ( $T_1$  or  $T_2$ ), then it either deposits with deposition probability  $P_d$ , or reflects and flies back into the bulk of the gas phase. If the



molecule hits the opening of trench, then a trajectory is simulated, *i.e.* the sequence of collision segments until the molecule leaves the system, which means the molecule is either being deposited or flies backward and crosses the source line  $S$ . Examples of trajectories of a DR molecule and corresponding events are presented in Figure 6.8. If  $P_d$  equals 0 (Figure 6.8a), and a DR molecule collides with the top surface area, then it will be reflected away immediately without deposition, as illustrated in the right corner ( $T_2$ ). If the molecule enters into the trench, then it will leave the trench after multiple reflections, still without any deposition. In contrast, if  $P_d$  equals 1 (Figure 6.8b), then in any situation, the molecule will be immediately deposited at the place of the first collision. If  $P_d$  is a value between 0 and 1 (Figure 6.8c), the DR molecule colliding with the top surface has two possibilities: depositing as  $\text{TiO}_2$  with probability of  $P_d$ , or reflecting away with probability  $1-P_d$ . However, for the molecule entering the trench, there is a third possibility. The molecule will reflect inside the trench, and for every collision with the wall or bottom of the trench, there is a chance of deposition. So, there is a possibility that deposition happens after multiple reflections.

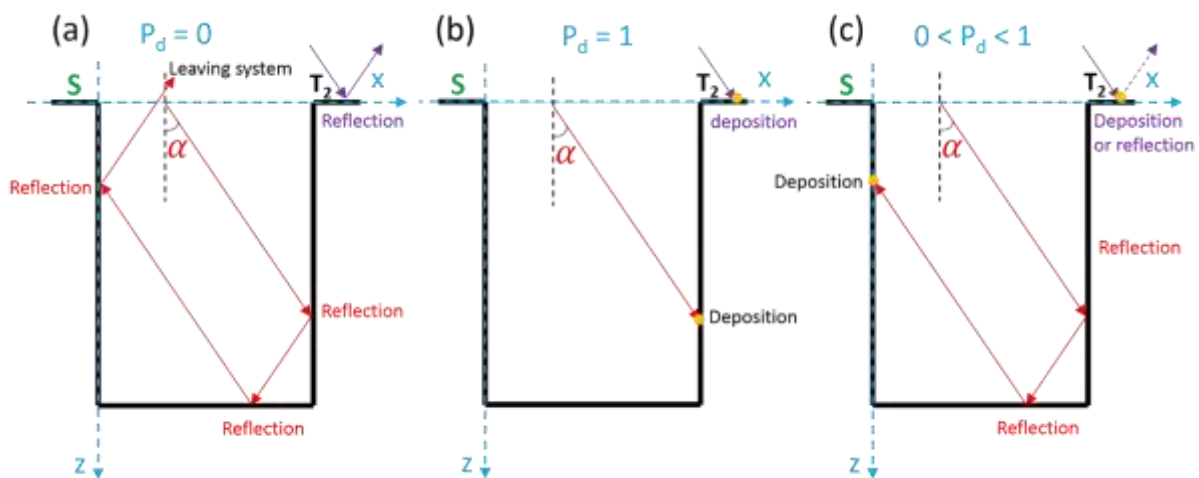


**Figure 6.8** Schematic of reflection and deposition at different deposition probabilities,  $P_d = 0$  (a),  $P_d = 1$  (b) and  $0 < P_d < 1$  (c).

When a number of trajectories are simulated, the position coordinates where deposition occurs are calculated. To simulate an informative measure of the deposition rate, averaging is applied by making use of histograms. Consider a sequence of  $K+1$  points at  $W_1$ , (*i.e.* points with  $x = 0$ ):  $z_0 = 0, z_1, z_2, \dots, z_{K-1}, z_K = L$ , as illustrated in Figure 6.9. This sequence of  $K+1$  points defines  $K$  bins of the histogram, *i.e.*  $K$  intervals  $[z_0, z_1], [z_1, z_2], \dots, [z_{K-1}, z_K]$ .

Calculating the number of deposition events within a certain histogram bin yields the average deposition rate in each interval and ultimately leads to thickness profiles of the deposited films.

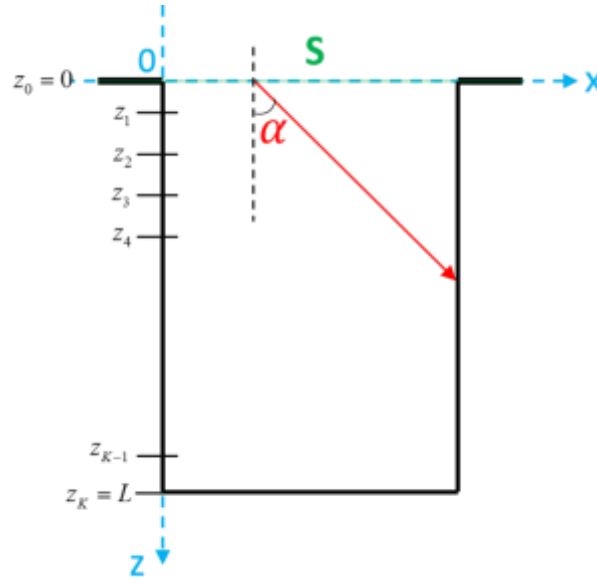


**Figure 6.9** Histogram bins on the wall.

#### 6.4.2 Monte-Carlo description

Consider the segments of the trench along dimension  $y$  has a length of  $Y$  [ $\mu\text{m}$ ]. All volumes and masses of deposited  $\text{TiO}_2$  will be related to these segments. Fix a point  $z$  at the wall, and consider the LPCVD deposition process during time  $t$  [s] is under the steady-state regime, *i.e.* the deposition rate is constant with time<sup>[24-26]</sup>. Denote the number of particles which entered system via the source boundary as  $M$ . For the experiment run at temperature  $T$  [K],  $M$  can be written as

$$M = kt c_s(T), \quad (\text{Eq. 6.11})$$

where  $c_s(T)$  [ $\mu\text{m}^{-3}$ ] is the precursor concentration at the source plane and  $k$  [ $\mu\text{m}^3/\text{s}$ ] is a proportionality constant. Denote  $d(z, \Delta z)$  [ $\mu\text{m}$ ] to be the average thickness of the deposited  $\text{TiO}_2$  in the interval  $\Delta z$  around point  $z$ , then, after running  $M$  particles, the deposited volume of the  $\text{TiO}_2$  is equal to  $d(z, \Delta z)Y \Delta z$  [ $\mu\text{m}^3$ ]. Denote volume of a single  $\text{TiO}_2$  molecule as  $V_{\text{TiO}_2}$  and the number of incoming (and colliding) particles in the interval  $\Delta z$  around point  $z$  as  $M_z$ , then the deposited volume can be expressed as

$$d(z, \Delta z)Y \Delta z = V_{\text{TiO}_2} M_z P_d(T). \quad (\text{Eq. 6.12})$$

Dividing both sides of Eq. 6.12 by  $MY\Delta z$  leads to

$$\frac{d(z, \Delta z)}{M} = V_{\text{TiO}_2} P_d(T) \frac{M_z}{MY\Delta z}. \quad (\text{Eq. 6.13})$$

Replacing  $M$  in the left hand side of Eq. 13 by Eq. 11, the following expression is obtained

$$\frac{1}{kc_s(T)} \frac{d(z, \Delta z)}{t} = V_{\text{TiO}_2} P_d(T) \frac{M_z}{MY\Delta z}. \quad (\text{Eq. 6.14})$$

Consider a limit of both parts of Eq. 6.14, when  $\Delta z \rightarrow 0$  and  $M \rightarrow \infty$  (implying  $t \rightarrow \infty$ ). The physical meaning of these limits is that deposition rate of a particular point at the wall is finite and the deposition time is sufficiently long. Note that the thickness of the already deposited layers has a negligible influence on the further deposition process, because the deposited layers are very thin in comparison with the trench size. By description of the process, the ratio  $\frac{d(z, \Delta z)}{t}$  should have a limit, corresponding to the steady-state deposition rate; denote it as

$d_r(z)$  [ $\mu\text{m/s}$ ]. Taking limits in both parts of Eq. 6.14 leads to

$$\begin{aligned} \frac{1}{kc_s(T)} \frac{d(z, \Delta z)}{t} &= V_{\text{TiO}_2} P_d(T) \frac{M_z}{MY\Delta z} \\ \downarrow \qquad \qquad \downarrow & \\ \frac{1}{kc_s(T)} d_r(z) &= V_{\text{TiO}_2} P_d(T) f(z) \end{aligned} \quad (\text{Eq. 6.15})$$

where function  $f(z)$  [ $\mu\text{m}^{-2}$ ] is defined as

$$\frac{M_z}{M} \frac{1}{Y\Delta z} \xrightarrow[\Delta z \rightarrow 0]{M \rightarrow \infty} f(z), \quad (\text{Eq. 6.16})$$

which represents the distribution density of collisions [ $\mu\text{m}^{-2}$ ] in point  $z$ . Rearranging Eq. 6.15, the deposition rate is expressed as

$$d_r(z) = kc_s(T) V_{\text{TiO}_2} P_d(T) f(z), \quad (\text{Eq. 6.17})$$

which holds in any point  $z$  at the wall. Eq. 6.17 can be considered as a generalization of the deposition rate of Eq. 6.3 given in Ref. [27].

Considering a uniform distribution of precursor molecules on the top (flat) part of the substrate, the distribution density of the number of collisions at any point of the top surface must be constant. Consequently,

$$d_r(top) = kc_s(T) V_{TiO_2} P_d(T) f(top), \quad (\text{Eq. 6.18})$$

where  $d_r(top)$  [ $\mu\text{m/s}$ ] is the steady-state deposition rate on the top part and  $f(top)$  is the corresponding distribution density of collisions [ $\mu\text{m}^{-2}$ ] on the top surface. The ratio of Eq. 6.17 and Eq. 6.18 can then be expressed by

$$\frac{d_r(z)}{d_r(top)} = \frac{f(z)}{f(top)}, \quad (\text{Eq. 6.19})$$

and, consequently,

$$d_r(z) = d_r(top) \frac{f(z)}{f(top)}. \quad (\text{Eq. 6.20})$$

Consider function  $h(z)$  to be defined by

$$h(z) = P_d f(z). \quad (\text{Eq. 6.21})$$

By definition,  $h(z)$  represents the density of depositions [ $\mu\text{m}^{-1}$ ] at any point  $z$ . Assuming that the deposition probabilities at the top and the wall of trench are equal, then, Eq. 6.20 can be rewritten as

$$d_r(z) = d_r(top) \frac{f(z)}{f(top)} = d_r(top) \frac{P_d f(z)}{P_d f(top)} = d_r(top) \frac{h(z)}{h(top)}. \quad (\text{Eq. 6.22})$$

For a deposition experiment runs for  $t$  seconds under steady-state conditions, the corresponding deposited film thicknesses ( $d(z)$  and  $d(top)$ ) can be represented by

$$d(z) = t d_r(z) \quad \text{and} \quad d(top) = t d_r(top). \quad (\text{Eq. 6.23})$$

From Eq. 6.20 it follows that

$$d(z) = d(top) \frac{f(z)}{f(top)} = t d_r(top) \frac{f(z)}{f(top)} = t d_r(top) \frac{h(z)}{h(top)}. \quad (\text{Eq. 6.24})$$

Eq. 6.24 clearly shows that changing the deposition time will increase or decrease the thickness of the deposited films in all available points simultaneously. The ratio of deposited film thicknesses in any two points depends on the geometry and deposition probability but not on the duration of the deposition process. Combining Eq. 6.18 and Eq. 6.23 results in

$$d(top, T) = t kc_s(T) v_0 P_d(T) f(top), \quad (\text{Eq. 6.25})$$

where only  $c_s(T)$  and  $P_d(T)$  depend on the deposition temperature. All other parameters are only dependent on the geometry or are physical constants. Since the temperature of the bulk gas phase is kept constant (room temperature), the dependency of  $c_s(T)$  on temperature is related to diffusion and precursor decomposition rate. For two deposition experiments with the same deposition time but different deposition temperatures  $T_1$  and  $T_2$ , the following relation holds

$$\frac{d(top, T_1)}{d(top, T_2)} = \frac{c_s(T_1)P_d(T_1)}{c_s(T_2)P_d(T_2)}, \quad (\text{Eq. 6.26})$$

and therefore

$$\frac{c_s(T_2)}{c_s(T_1)} = \frac{d(top, T_2)}{d(top, T_1)} \frac{P_d(T_1)}{P_d(T_2)}, \quad (\text{Eq. 6.27})$$

which will be used to estimate the degree of mass transport limitation (*i.e.* decrease in surface concentration) in the high temperature deposition region.

### 6.4.3 Monte-Carlo implementation

According to Eq. 6.24 or Eq. 6.25, the thickness of deposited film at any point can be calculated. However, the equations are of no practical use, since  $h(z)$  and  $h(top)$  are, in general, unknown. The same statement holds for  $f(z)$  and  $f(top)$ . However, both functions can be estimated by the Monte-Carlo method. Suppose that  $N$  independent trajectories of incoming particles were modelled, considering bin  $[z_{i-1}, z_i]$  on the wall and defining Monte Carlo estimator for  $h(z)$ ,  $z \in [z_{i-1}, z_i]$  as

$$\hat{h}_N([z_{i-1}, z_i]) = \frac{N_i}{N} \frac{1}{z_i - z_{i-1}}, \quad (\text{Eq. 6.28})$$

where  $N_i$  is the number of collisions of the simulated particles on the wall in the interval  $[z_{i-1}, z_i]$ . When  $N$  grows, the histogram estimate  $\hat{h}_N([z_{i-1}, z_i])$  converges to the average value of the density of collisions  $h(z)$  in interval  $[z_{i-1}, z_i]$ , that is

$$\hat{h}_N([z_{i-1}, z_i]) = \frac{N_i}{N} \cdot \frac{1}{z_i - z_{i-1}} \xrightarrow[N \rightarrow \infty]{P} \frac{1}{z_i - z_{i-1}} \int_{z_{i-1}}^{z_i} h(z) dz \approx h\left(\frac{z_{i-1} + z_i}{2}\right). \quad (\text{Eq. 6.29})$$

In turn, the density of collisions at the top flat part is also estimated on the basis of the same  $N$  emitted particles, producing  $\hat{h}_N(top)$ . The estimated deposition thickness in the interval  $[z_{i-1}, z_i]$  is therefore

$$\hat{d}([z_{i-1}, z_i]) = \tilde{d}_{top} \frac{\hat{h}_N([z_{i-1}, z_i])}{\hat{h}_N(top)}, \quad (\text{Eq. 6.30})$$

where  $\tilde{d}_{top}$  [ $\mu\text{m}$ ] is experimentally measured film thickness at the top surface of the substrate.

Note that when  $N$  is large, both  $\hat{h}_N([z_{i-1}, z_i])$  and  $\hat{h}_N(top)$  follow Gaussian distribution according to the Central Limit Theorem. Therefore, the Monte-Carlo distribution of Eq. 6.29 follows a ratio law<sup>[28]</sup>. In the subsequent sections, the Monte-Carlo simulations are studied. Eq. 6.29 is investigated for a number of experiments performed under a variety of temperatures.

## 6.5 Simulation results and discussion

### 6.5.1 Estimation of deposition probability

A Matlab program implementing the Markov chain Monte-Carlo model has been set up. The program includes the precursor distribution and the “hard ball” collision model described in section 4.1. The Monte-Carlo simulations were performed by averaging over  $5 \times 10^6$  trajectories, which takes 15 ~ 25 minutes of computing time on a HP notebook with Intel® Core(TM) i7-2920 XM CPU@2.53 GHz with 32 GB operational memory. Histogram with 30 bins was used to determine the deposition density. Figure 6.10 shows the simulation results for experimentally deposited  $\text{TiO}_2$  in 30  $\mu\text{m}$  and 10  $\mu\text{m}$  width trenches at various deposition temperatures. The experimental data are represented by the symbols, as shown in Figure 6.4, and the simulations are represented by the lines. The overall quality of fits is good, except for the slight deviations found at high temperatures.

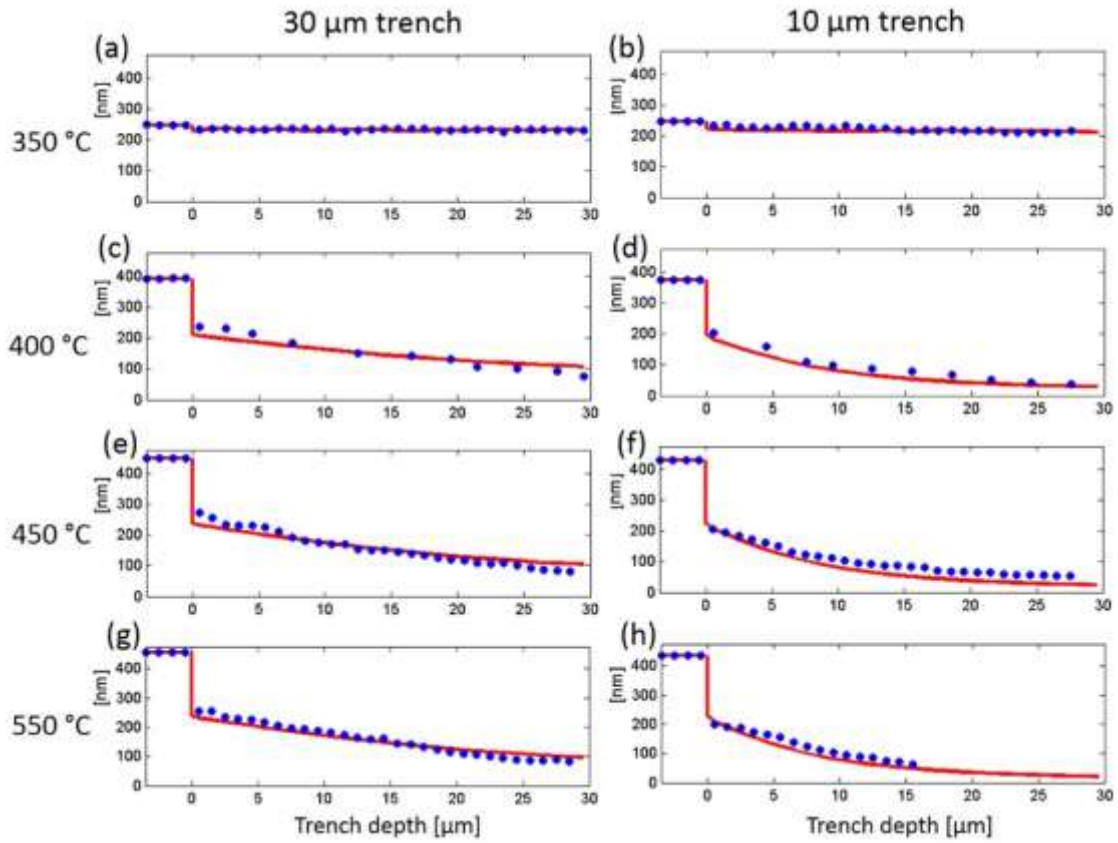


**Figure 6.10** Simulated (lines) and experimentally observed (symbols) profiles at the walls deposited at 350 °C (a) and (b); 400 °C (c) and (d); 450 °C (e) and (f); 550 °C (g) and (h).

The parameters extracted from the simulations are summarized in Table 6.1. The values of  $P_d$  listed in Table 6.1 are obtained by optimizing the simulated thickness profiles with respect to the experimentally measured ones, by varying deposition probability for each temperature separately. A non-linear least squares optimization algorithm was implemented in Matlab. The simulated thickness profiles were normalized to have exactly the same top thickness as in the measurements for each particular temperature. After that Eq. 6.27 was used to calculate the  $c_s(T)/c_s(350^\circ\text{C})$  ratio.

It is interesting to see how the Monte-Carlo simulations can be related to the Arrhenius plot of Figure 5.5. At 350 °C, clearly within the kinetically controlled temperature region, the deposition probability is very low ( $P_d = 0.0125$ ) and uniform depositions are achieved. In contrast, in the mass-transfer controlled regime, the deposition probability is moderate to high (above 0.65) and the films are inhomogeneous.

It also can be seen in Table 6.1 that the  $c_s(T)/c_s(350^\circ\text{C})$  ratio changes considerably with increasing temperature. Since the deposition of  $\text{TiO}_2$  is kinetically controlled at  $350^\circ\text{C}$ , the mass-transfer rate of the precursor is higher than the chemical decomposition rate on the substrate surface. Under these conditions, it is indeed to be expected that the surface concentration of precursor molecules at  $350^\circ\text{C}$  is equal to the precursor concentration in the bulk of the gas phase. When the deposition temperature increases, the decomposition reaction rate increases to higher values, depleting the precursor on the substrate surface more significantly. Consequently,  $c_s(T)$  decreases to lower values as Table 6.1 indicates [27].

**Table 6.1** Parameters of Monte-Carlo model for deposition process at various temperatures.

T [°C]	$P_d$ [%]	$\tilde{d}_{\text{top}}$ [um],	$c_s(T)/c_s(350^\circ\text{C})$	$\tilde{d}_{\text{top}}$ [um],	$c_s(T)/c_s(350^\circ\text{C})$
		10 $\mu\text{m}$ trench	10 $\mu\text{m}$	30 $\mu\text{m}$ trench	10 $\mu\text{m}$
350	1.25	0.247	1.00	0.248	1.00
400	65	0.375	0.03	0.391	0.03
450	75	0.430	0.03	0.450	0.03
550	80	0.435	0.03	0.455	0.03

## 6.5.2 Deposition efficiency

The deposition efficiency is defined as the total probability that a precursor molecule which is emitted from the source towards the trench at a particular angle  $\alpha$  in point  $x$  will be deposited. If the entrance point is at the top part of the substrate (segment  $T_1$  or  $T_2$ ), then the total deposition probability, denoted as  $P_d^{\text{tot}}(x, \alpha)$ , is equal to the probability of deposition in a single event  $P_d$ , because the precursor particle has only one chance to collide with the top surface, otherwise it will be reflected and return to the bulk gas phase. If the entrance point is at the opening of the trench, then, in general  $P_d^{\text{tot}} \neq P_d$ . Consider average total deposition probability ( $\bar{P}_d^{\text{tot}}$ ), where averaging is done across  $x$  and  $\alpha$  according to the precursor distribution. If  $P_d = 1$  then  $\bar{P}_d^{\text{tot}} = P_d = 1$ , otherwise  $\bar{P}_d^{\text{tot}}$  is a complicated function which can be evaluated only numerically by the Monte-Carlo method. The nominal estimate for  $\bar{P}_d^{\text{tot}}$  is



$$\bar{P}_d^{tot} = \frac{H\bar{d}_{wall_1} + H\bar{d}_{wall_2} + L\bar{d}_{bot}}{(L\bar{d}_{top} / P_d)} \quad (\text{Eq. 6.31})$$

where  $\bar{d}_{wall_1}$  and  $\bar{d}_{wall_2}$  are average thicknesses of the deposited material on both walls,  $\bar{d}_{bot}$  is an average thickness of the deposited material at the bottom and  $\bar{d}_{top}$  is the average thickness of the deposited material on the top part of the trench substrate. Eq. 29 is a ratio of the total amount of deposited material (in the numerator) to the amount of material which entered the trench (in the denominator).

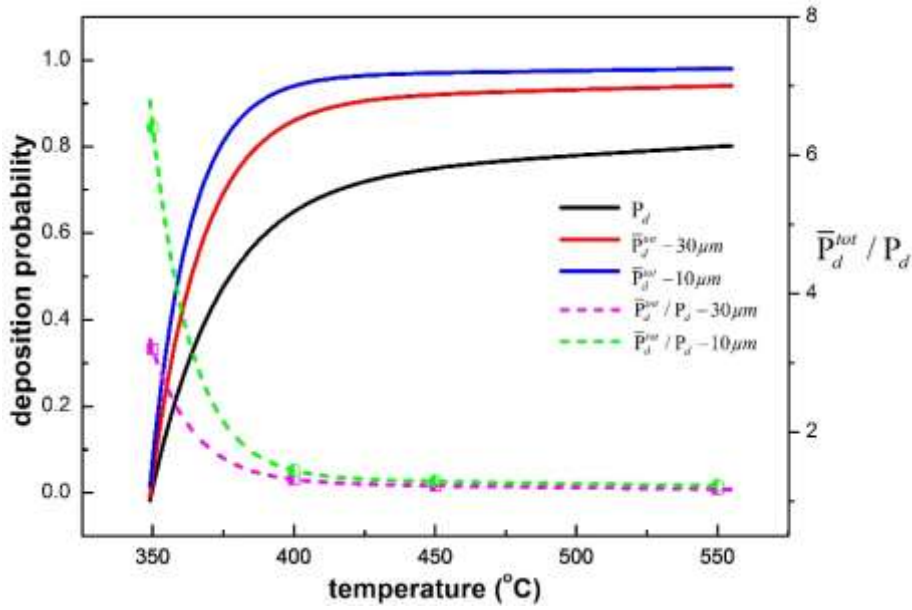


**Figure 6.11** Total deposition probabilities and the ratios of  $\bar{P}_d^{tot} / P_d$  at various temperatures.

Figure 6.11 shows that  $P_d$  increases with increasing temperature, which is consistent with the fact that high temperatures will enhance the precursor decomposition rate. It is interesting to note that  $\bar{P}_d^{tot}$  inside the trenches are always higher than  $P_d$ , for both the 30 and 10  $\mu\text{m}$  wide trenches. The trench geometry also influences the values of  $\bar{P}_d^{tot}$ . Narrow trench (10  $\mu\text{m}$ ) shows higher values for  $\bar{P}_d^{tot}$  at all temperatures.

The ratio of  $\bar{P}_d^{tot} / P_d$  reaches the highest value of 6.4 for the 10  $\mu\text{m}$  wide trenches at 350  $^{\circ}\text{C}$ . This means that compared to the top surface, the DR precursor molecules entering the 10  $\mu\text{m}$  trenches have a 6.4 times higher chance to be deposited than returning back to the bulk of the gas phase. As shown in Figure 6.8, molecules entering the trench can have multiple collision

options before they decompose. Contrastingly, the precursor molecules only have a single chance to be deposited at the top flat part of the substrate. The deposition probability inside the trenches ( $\bar{P}_d^{tot}$ ) is therefore higher than that on the top surface. However, when the deposition probability close to 1 as deposition temperature increases, the precursor molecules would immediately deposit as they collide with the substrate surface, leaving less opportunities to reflect inside the trench. Under this circumstance, without the contribution of multiple reflections inside the trench, there is no significant difference between  $\bar{P}_d^{tot}$  and  $P_d$ . Therefore, the ratio of  $\bar{P}_d^{tot} / P_d$  drops quickly as deposition temperature increases.

### 6.5.3 Distribution of precursor inside trench

As discussed in section 6.5.2 and illustrated by Figure 6.8, at lower temperatures, when the value of  $P_d$  is low, there are more precursor molecular reflections inside the trenches. However, at higher temperatures, the number of reflections decrease significantly as  $P_d$  increases. These reflections will facilitate the precursor molecules to transfer to the bottom of the trenches. Therefore, the final distribution of precursor inside trench is not only determined by the initial distribution as explained in section 4.1, but also influenced by the reflections inside trenches.

Figure 6.12 shows the simulated precursor distribution (*i.e.* normalized per one particle entered the trench) inside 30  $\mu\text{m}$  and 10  $\mu\text{m}$  wide trenches. Figure 6.12a and b corresponds to the deposition at 350°C, at which the deposition process is kinetically-controlled. The precursor concentrations in both trenches are more or less constant, with only minor concentration drops appear near the walls and bottoms. That is indeed to be expected for a kinetically controlled deposition process. This implies that not much precursor is consumed in the trenches and that almost all precursor molecules will eventually return back to the gas phase. Because of this homogeneous distribution of precursor, uniform films are deposited.

Figure 6.12c-d relates to the deposition at 550°C with  $P_d = 0.8$ , which corresponds to the mass-transport controlled deposition region. It is clear that the precursor density drops rapidly inside the trenches, which is different from the kinetically-controlled case shown in Fig. 6a and b. Because the deposition probability is high, the precursor molecules entered the trench are readily deposited, leaving less chance to be reflected to the bottom of the trench. Consequently, obvious concentration gradients are established. Difference in concentrations of precursor at the opening and near the bottom of the trench reaches almost three times for 30  $\mu\text{m}$  trench and

four times for 10  $\mu\text{m}$  trench. Naturally, the wider opening provides larger number of molecules, therefore more molecules reach the bottom of the trench.

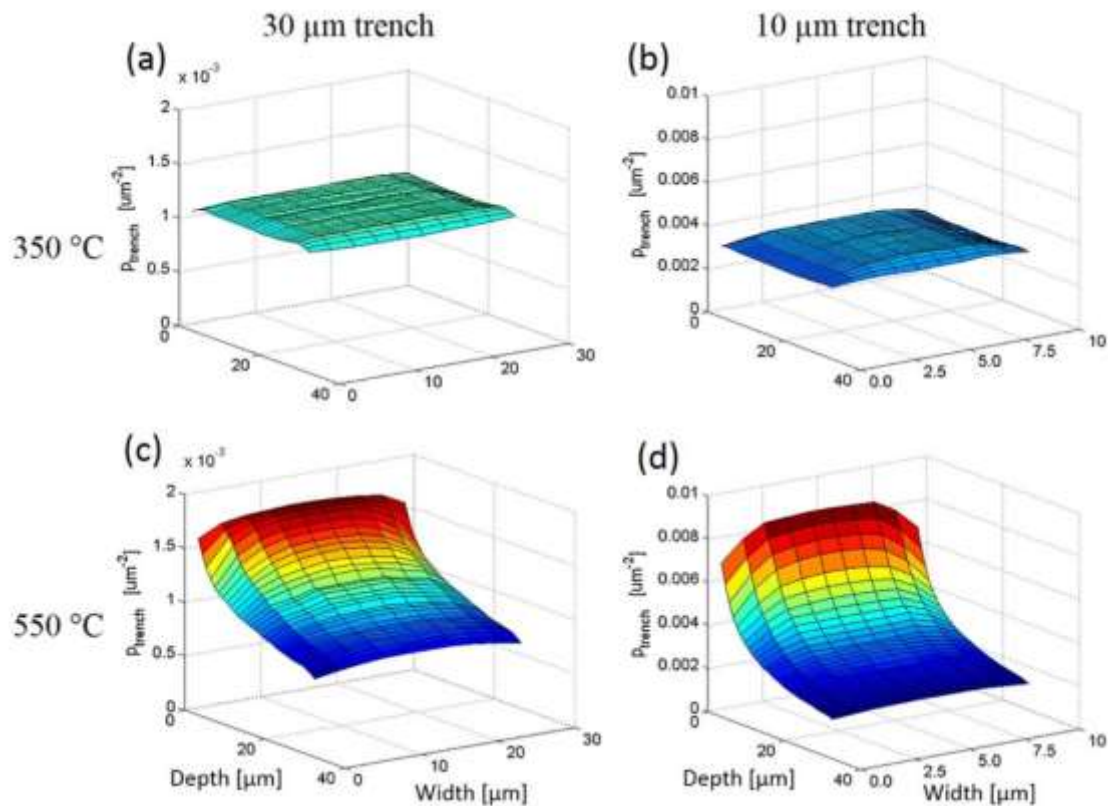


**Figure 6.12** Simulated precursor density in 30  $\mu\text{m}$  (a and c) and 10  $\mu\text{m}$  (b and d) trenches. Figures (a) and (b) correspond to the low temperature (350°C); (c) and (d) relates to high temperature deposition (550°C).

It also can be seen that at the small depths, there is a concentration profile across the width of the trench, with larger density values in the middle of the trench. Apparently, when deposition rate is high, the precursor near the substrate surface where deposition process taking place will be consumed, resulting in a lower concentration than the middle part of the trench. Near the bottom, the concentration profile across the trench is flat. There, not only reactions were carried on the surface of the bottom of the wall, the deposition also takes place on the bottom surface, therefore, no differences in concentration are observed. Note that Figure 6.12 represent probability density of the precursor molecules, *i.e.* normalized per one molecule entered the trench. By this reason, the average level of precursor densities in Figure 6.12a-b are consistent (30  $\mu\text{m}$  wide trench). The same holds for Figure 6.12c-d (10  $\mu\text{m}$  wide trench). The real density of precursor will depend on the surface concentration of the precursor, as discussed in section 6.4.1.

## 6.5.4 Overview of deposition profiles

After optimizing all the parameters, the overview of the thickness profiles trenches with three widths are plotted, as shown in Figure 6.13. In Figure 6.13a, 17c and 17e, deposition profiles are normalized to correspond to the same top thickness (400 nm), stressing the shape of deposition profiles. Profile for the top flat part is shown to illustrate the scale of figure; top flat part corresponds to negative values of the trench depth. It can be concluded that thickness of the deposited film on the wall increases with decreasing  $P_d$ , and all positions reach 400 nm when  $P_d$  approaches to zero. In this case the deposited layers are ideally conformal and no visible changes in film thickness can be observed. That conclusion holds for trenches of all widths, implying that kinetically controlled deposition of  $\text{TiO}_2$  is applicable up to the structures with large aspect ratio. In contrast, when  $P_d$  increases, the step coverage becomes worse. It also should be noted that thickness of deposited material declines faster when the trench becomes narrower, especially near the bottom of the trench. For example, in 5  $\mu\text{m}$  trench (Figure 6.13e), the film thickness starts to become negligibly small at a depth approximately 10  $\mu\text{m}$ .

The thickness profiles in Figure 6.13a, c and e are normalized to the same top deposition thickness, under the assumption of sufficiently long deposition time. In contrast, Figure 6.13b, d and f give the shape of deposition profiles at a constant deposition time. The deposition time is set to the value which gives 400 nm at the top flat part for  $P_d = 1$ . It is clear that deposition probability has a large influence on the thickness and shape of the deposited films. Apparently, low deposition probability creates more uniform deposited film, *i.e.* the film thickness difference between the top surface and bottom is small, but the intensity of deposition process is smaller, resulting in a thinner top film thickness. From these plots, it can be concluded that reducing deposition probability leads to decrease of deposition rate, and therefore to decline in top film thickness, but increasing uniformity.

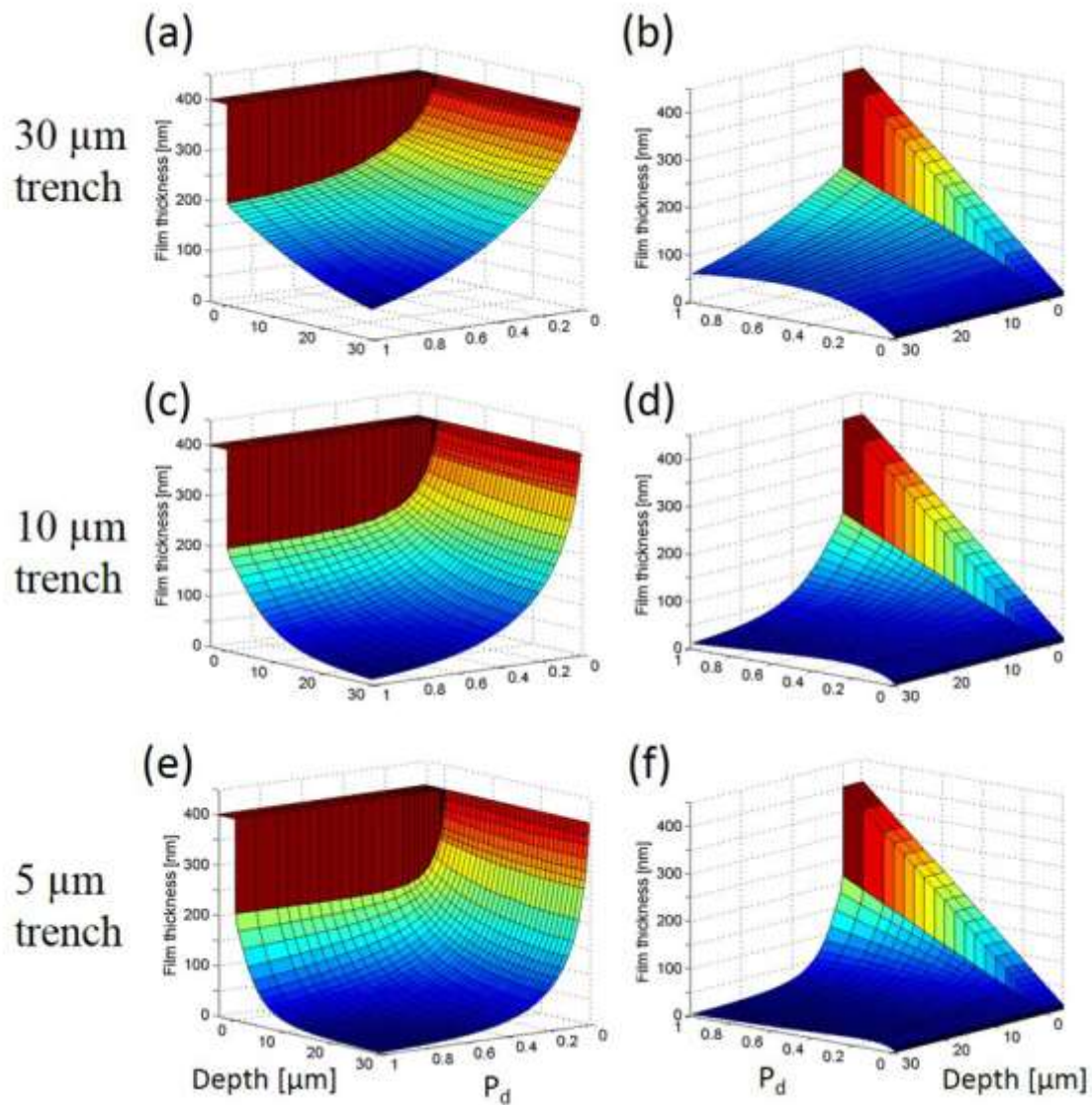


**Figure 6.13** Evolution of deposition profiles as a function of deposition probability for trench width 30  $\mu\text{m}$  (a and b), 10  $\mu\text{m}$  (c and d), 5  $\mu\text{m}$  (e and f), respectively.

## 6.6 Conclusions

The deposition of  $\text{TiO}_2$  thin films in 3D-structured substrates has been experimentally and theoretically investigated as a function of deposition temperature. It was experimentally found that the deposition kinetics on planar substrates can be accurately controlled by adjusting the deposition temperature. In the high-temperature region the deposition was found to be mass-transfer controlled whereas it becomes kinetically-controlled in the low-temperature region. The thickness profiles of deposited thin films in 3D-structured substrates have also been investigated as a function of temperature.

A Markov chain Monte-Carlo simulation model has been developed to simulate the experimentally determined 3D deposition profiles of TiO<sub>2</sub> in trenches as a function of trench depth and width at various temperatures. A theoretical description of the Monte-Carlo method is given. For the first time, a systematic study of the deposition process parameters has been performed.

The experimentally observed deposition profiles are compared with the developed MCMC model. Good agreement between the model and experiments has been achieved in all cases. It was found that the deposition probability (reactive sticking coefficient) of a single collision is close to zero in the kinetically-controlled temperature region and is close to one in the mass transport controlled temperature region. An estimation of the precursor distribution inside the trenches has also been extracted from the Monte-Carlo model. The precursor concentration keeps decreasing as the trench depth increases in the diffusion-controlled region. On the other hand, the precursor molecules are homogeneously distributed inside the trenches in the kinetically-controlled region. The reflections of precursor molecules inside trench play an important role in reaching a uniform 3D deposition. The Monte-Carlo approach was found to be successful in explaining the experimentally observed deposition profiles. A simple “hard ball collision” scheme without considering scattering between precursor molecules and carrying gas molecules, is sufficient to accurately describe the experimental LPCVD deposition process of TiO<sub>2</sub>.

## 6.7 Appendix: Markov chains and integral equations

Suppose that the deposition probability  $P_d$  is between zero and one. The phase variable of the model consists of three numbers: coordinates  $x$  and  $z$ , which denote a position inside the simulated area (including the boundaries); and  $\theta$ , which denotes the incoming angle of the precursor molecules. The set of all possible (boundary) coordinates is given by  $D = T_1 \cup T_2 \cup W_1 \cup W_2 \cup O \cup B$ . Consider  $\mathcal{D}' = D \times [0, 2\pi]$ , setting  $\mathcal{D}'$  by Borel  $\sigma$ -algebra  $\mathcal{B}'$ , forming measurable space  $(\mathcal{D}', \mathcal{B}')$ . A point in this phase space is denoted as  $r' = (z, x, \theta)$ . Variable  $r'$  takes values in  $D \times [0, 2\pi]$ . Extend the phase space by an additional special state  $\Delta$ , corresponding to the ‘End of Trajectory’ (EOT). The  $\Delta$  state is reached when particle is either deposited or flew back to the gas phase via the opening. The  $\Delta$  is an ‘absorbing’ state; particle which enter EOT will never leave it. Consider an extended phase space  $(\mathcal{D}, \mathcal{B})$ , where

$\mathcal{D} = (\mathcal{D}', \Delta)$  and  $\mathcal{B}$  is minimal  $\sigma$ -algebra containing  $\mathcal{B}'$  and  $\{\Delta\}$ . A sequence of points representing trajectory of the precursor molecule, i.e.  $\rho_1, \rho_2, \dots, \rho_\tau$  forms homogeneous Markov Chain with the phase space  $(\mathcal{D}, \mathcal{B})$ . Without restricting generality, assume that a probability space  $(\Omega, \mathcal{F}, \mathcal{P})$  associated with such Markov Chain is defined. The construction of this probability space follows the Markov Chain simulation scheme defined in section 4.1. A transition function of this Markov chain is well defined, i.e. there exists a regular conditional probability distribution  $p(r, \Gamma) = p(\rho_n \in \Gamma | r_{n-1} = r)$  for each  $r \in \mathcal{D}$  and  $\Gamma \in \mathcal{B}$ <sup>[29]</sup>. Since point  $\Delta$  is an ‘absorbing’ state, then  $p(\Delta, \{\Delta\}) = 1$ . A starting point of Markov Chain,  $\rho_1$ , is distributed in  $\mathcal{B}$  according to distribution  $\pi(dr)$ . The source distribution  $\pi(dr)$  defines a distribution of particles coming directly from the bulk of the gas phase without any collisions/reflections. By definition,  $\pi(dr)$  is the probability that precursor molecules coming into simulation area will collide with the top/wall/bottom in the ‘elementary volume’  $dr$  of the phase space near the point  $r$ . Denote the ‘absorption’ probability  $a(r) = p(\rho_n = \Delta | \rho_{n-1} = r)$  and define the length of the trajectory of Markov chain as  $\tau = \max(k : \rho_k \neq \Delta)$ . The ‘absorption’ probability determines probability of the Markov chain to go to the state  $\Delta$  at the next step if currently it is in the state  $r$ ,  $r \neq \Delta$ . Note that  $a(r) = P_d$  if  $r \in W_1 \cup W_2 \cup B$ ; and  $a(r) = 1$  if  $r \in T_1 \cup T_2 \cup O$ . Therefore,  $a(r) \geq P_d$  and  $\tau < \infty$ .

The constructed phase space agrees with the general probabilistic description of Markov chain for solution of linear integral equations<sup>[30, 31]</sup>. Denote the distribution of precursor molecules after the first collision with the walls by the expression

$$\delta^{(1)}(r_1) = \int_{\mathcal{D}} p(r_1 | r_0) \pi(dr_0), \quad (\text{Eq. A.1})$$

according to the total probability law. Consider an integral operator  $P$  corresponding to Eq. A.1, then Eq. A.1 can be rewritten as

$$\delta^{(1)} = P\pi. \quad (\text{Eq. A.2})$$

In a similar way one can define the distribution of precursor molecules after the second, third and higher order collisions as

$$\delta^{(n)}(r_n) = \int_{\mathcal{D}} p(r_n | r_{n-1}) \varphi^{(n-1)}(dr_{n-1}), \quad (\text{Eq. A.3})$$

or, in operator notations,

$$\delta^{(n)} = P^n \pi . \quad (\text{Eq. A.4})$$

Now define distribution  $\varphi$  according to

$$\delta = \sum_{n=0}^{\infty} P^n \pi , \quad (\text{Eq. A.5})$$

with apparent convention  $P^0 \pi = \pi$ . It can be shown that  $\delta$  satisfies the following integral equation

$$\delta = P\varphi + \pi , \quad (\text{Eq. A.6})$$

which is a Fredholm integral equation of 2<sup>nd</sup> kind. The Monte-Carlo simulation of the particle trajectories is, in fact, a calculation of the Neumann series solution of Eq. A.6. Denote the moment of absorption of the Markov Chain as  $\rho_\tau$ . According to Lemma 1.1.3 in reference<sup>[31]</sup>, a distribution  $\mu(dr) = P(\rho_\tau \in dr)$  is expressed as

$$\mu(dr) = a(r)\delta(dr) , \quad (\text{Eq. A.7})$$

where  $\delta$  is an iterative solution of Eq. A.6, (*i.e.* Eq. A.5). Suppose that a solution for  $\delta$  in Eq. A.6 is available and one must estimate a distribution of number of deposition events on the wall (say  $T_1$ ), in the histogram bin  $[z_i, z_{i+1}]$ , then the required absorption estimator can be given by

$$h_i = \int I_{H_i}(r) \mu(dr) , \quad (\text{Eq. A.8})$$

where set  $H_i$  determines the element of histogram

$$H_i = \{ r = (z, x, \alpha) \text{ such that } z \in [z_i, z_{i+1}], x = 0, \alpha \in [0, 2\pi] \} , \quad (\text{Eq. A.9})$$

and  $I_{H_i}(r)$  defines an indicator function of  $H_i$

$$I_{H_i}(r) = \begin{cases} 1, & r \in H_i \\ 0, & r \notin H_i \end{cases} . \quad (\text{Eq. A.10})$$

Now consider a sequence of independent trajectories of this Markov Chain. The simulated trajectory is a sequence of points in the phase space, *i.e.* after the modeling of  $N$  trajectories the following dataset is available



$$\begin{aligned}
r_1^{(1)}, r_2^{(1)}, \dots, r_{K_1}^{(1)}, & \quad \triangle \\
r_1^{(2)}, r_2^{(2)}, \dots, r_{K_2}^{(2)}, & \quad \triangle \\
\dots, \dots, \dots, \dots, & \quad \triangle \\
r_1^{(N)}, r_2^{(N)}, \dots, r_{K_N}^{(N)}, & \quad \triangle
\end{aligned} \tag{Eq. A.11}$$

where notation  $r_k^{(j)}$  refers to the  $k^{\text{th}}$  link of the  $j^{\text{th}}$  trajectory. Note that  $K_j$  is the length of  $j^{\text{th}}$  trajectory and all trajectories are finishes by an absorbing state  $\Delta$ . A natural (*first moment*) estimator for a number of depositions in  $i^{\text{th}}$  interval of histogram is, therefore, defined as

$$\hat{h}_i(N) = \frac{1}{N} \sum_{j=1}^N I_{H_i}(r_{K_j}^{(j)}). \tag{Eq. A.12}$$

Obviously  $\hat{h}_i(N)$  is a consistent estimator of  $h_i$ , *i.e.*

$$\hat{h}_i(N) \xrightarrow{N \rightarrow \infty} h_i. \tag{Eq. A.13}$$

If the deposition probability  $P_d$  is known, any consistent estimator of the number of collisions  $\hat{f}_i(N)$  can be used to obtain an estimator of the number of depositions, according to  $\hat{h}_i(N) = P_d \hat{f}_i(N)$ . In particular, one can use standard collision estimator<sup>[30]</sup>, defined as

$$\hat{f}_i(N) = \frac{1}{N} \sum_{j=1}^N \sum_{k=1}^{K_j} I_{H_i}(r_{K_j}^{(j)}), \tag{Eq. A.14}$$

which provides a large space for improvements and variance of reduction techniques.

## References

1. M.P. Cantao, J.I. Cisneros, and R.M. Torresi, *Kinetic-Study of Lithium Electroinsertion in Titanium-Oxide Thin-Films*. Journal of Physical Chemistry **98** (1994) 4865-4869.
2. W.J. Borghols, D. Lutzenkirchen-Hecht, U. Haake, E.R. van Eck, F.M. Mulder, and M. Wagemaker, *The electronic structure and ionic diffusion of nanoscale LiTiO<sub>2</sub> anatase*. Phys Chem Chem Phys **11** (2009) 5742-5748.
3. S.K. Cheah, E. Perre, M. Rooth, M. Fondell, A. Harsta, L. Nyholm, M. Boman, T. Gustafsson, J. Lu, P. Simon, and K. Edstrom, *Self-Supported Three-Dimensional Nanoelectrodes for Microbattery Applications*. Nano Letters **9** (2009) 3230-3233.
4. W. Wang, M. Tian, A. Abdulagatov, S.M. George, Y.-C. Lee, and R. Yang, *Three-Dimensional Ni/TiO<sub>2</sub> Nanowire Network for High Areal Capacity Lithium Ion Microbattery Applications*. Nano Letters **12** (2012) 655-660.
5. J. Xie, P.-P.R.M.L. Harks, D. Li, L.H.J. Raijmakers, and P.H.L. Notten, *Planar and 3D deposition of Li<sub>4</sub>Ti<sub>5</sub>O<sub>12</sub> thin film electrodes by MOCVD*. Solid State Ionics **287** (2016) 83-88.
6. S. Murugesan, P. Kuppusami, N. Parvathavarthini, and E. Mohandas, *Pulsed laser deposition of anatase and rutile TiO<sub>2</sub> thin films*. Surface and Coatings Technology **201** (2007) 7713-7719.
7. K.N. Rao, M.A. Murthy, and S. Mohan, *Optical properties of electron-beam-evaporated TiO<sub>2</sub> films*. Thin Solid Films **176** (1989) 181-186.
8. J. Hamalainen, J. Holopainen, F. Munnik, T. Hatanpaa, M. Heikkila, M. Ritala, and M. Leskela, *Lithium Phosphate Thin Films Grown by Atomic Layer Deposition*. Journal of the Electrochemical Society **159** (2012) A259-A263.
9. P.H.L. Notten, F. Roozeboom, R.A.H. Niessen, and L. Baggetto, *3-D Integrated All-Solid-State Rechargeable Batteries*. Advanced Materials **19** (2007) 4564-4567.
10. L. Baggetto, H.C.M. Knoop, R.A.H. Niessen, W.M.M. Kessels, and P.H.L. Notten, *3D negative electrode stacks for integrated all-solid-state lithium-ion microbatteries*. Journal of Materials Chemistry **20** (2010) 3703-3708.
11. T.S. Cale, G.B. Raupp, and T.H. Gandy, *Free molecular transport and deposition in long rectangular trenches*. Journal of Applied Physics **68** (1990) 3645-3652.
12. D.G. Coronell and K.F. Jensen, *Simulation of Rarefied Gas Transport and Profile Evolution in Nonplanar Substrate Chemical Vapor Deposition*. Journal of The Electrochemical Society **141** (1994) 2545-2551.
13. J. Schlote, S. Hinrich, B. Kuck, and K.W. Schröder, *Topological effects regarding trench structures covered with LPCVD and PECVD thin films*. Surface and Coatings Technology **59** (1993) 316-320.
14. Y. Akiyama and N. Imaishi, *Applicability of one - dimensional diffusion model for step coverage analysis—Comparison with a simple Monte Carlo method*. Applied Physics Letters **67** (1995) 620-622.
15. G.A. Bird, *Molecular Gas Dynamics and the Direct Simulation of Gas Flows*, Clarendon Press, Gloucestershire, U.K. (1998).
16. K. Nanbu, *Angular distributions of molecular flux from orifices of various thickness*. Vacuum **35** (1985) 573-576.
17. S.T. Rodgers and K.F. Jensen, *Multiscale modeling of chemical vapor deposition*. Journal of Applied Physics **83** (1998) 524-530.

18. K.-H. Ahn, Y.-B. Park, and D.-W. Park, *Kinetic and mechanistic study on the chemical vapor deposition of titanium dioxide thin films by in situ FT-IR using TTIP*. *Surface and Coatings Technology* **171** (2003) 198-204.
19. F. Roozeboom, R.J.G. Elfrink, T. Rijks, J. Verhoeven, A. Kemmeren, J. van den Meerakker, Spie, and Spie, *High-density, low-loss MOS capacitors for integrated RF decoupling*, in *2001 International Symposium on Microelectronics, Proceedings*. 2001, Spie-Int Soc Optical Engineering: Bellingham. p. 477-483.
20. J.T. Drotar, Y.P. Zhao, T.M. Lu, and G.C. Wang, *Surface roughening in low-pressure chemical vapor deposition*. *Physical Review B* **64** (2001) 5.
21. M. Born and E. Wolf, *Principles of Optics: Electromagnetic Theory of Propagation, Interference and Diffraction of Light*, Cambridge University Press, Cambridge, U.K. (1997).
22. G.B. Arfken, H.J. Weber, and F.E. Harris, *Mathematical Methods for Physicists: A Comprehensive Guide*, Elsevier, Amsterdam (2012).
23. S.M. Ross, *Simulation*, Elsevier, Amsterdam (2006).
24. J. Xie, J.F.M. Oudenhoven, P.P.R.M.L. Harks, D.J. Li, and P.H.L. Notten, *Chemical Vapor Deposition of Lithium Phosphate Thin-Films for 3D All-Solid-State Li-Ion Batteries*. *Journal of the Electrochemical Society* **162** (2015) A249-A254.
25. S. Mathur and P. Kuhn, *CVD of titanium oxide coatings: Comparative evaluation of thermal and plasma assisted processes*. *Surface and Coatings Technology* **201** (2006) 807-814.
26. A.C. Jones and M.L. Hitchman, *Chemical Vapour Deposition: Precursors, Processes and Applications*, Royal Society of Chemistry, Cambridge U.K. (2009).
27. C.R. Kleijn, R. Dorsman, K.J. Kuijlaars, M. Okkerse, and H. van Santen, *Multi-scale modeling of chemical vapor deposition processes for thin film technology*. *Journal of Crystal Growth* **303** (2007) 362-380.
28. D.V. Hinkley, *On the ratio of two correlated normal random variables*. *Biometrika* **56** (1969) 635-639.
29. M. Loeve, *Probability Theory II*, Springer, Michigan (1978).
30. S.M. Ermakov, *Die Monte-Carlo-Methode und verwandte Fragen*, Oldenburg, Michigan (1975).
31. S. Ermakov, V.V. Nekrutkin, and A.S. Sipin, *Random Processes for Classical Equations of Mathematical Physics*, Springer, Netherlands (1989).

## Chapter 7 Summary and Outlook

Nowadays, the raising concepts of IoT and industry 4.0 create the emerging markets of smart cards, RFID tags, MEMS and wireless sensors, which all need power supply, but the room left for power supply is limited to mini-scales. In some conditions, powering smart devices from grid is not convenient or even impossible, leaving thin film microbatteries the only option. Compared with other power solutions, thin film microbatteries have lots of advantages. First, the size and shape of microbatteries are very flexible, which makes them easily embedded on/into other devices. The opportunities in which to use the microbatteries are endless. Secondly, thin film microbatteries have excellent cycle life performance. Normally, there is no pressure for solid-state microbatteries to cycle over 5000 times, which is sufficient to cover the life span of most devices. Thirdly, the power needs of smart sensors are very small and the power generated by a solar cell or other energy harvesting systems under normal condition is sufficient to power these sensors. Thin film microbatteries can easily be combined together with solar cells or other environmental energy harvesting systems, creating a “Zero-Power Wireless Sensor”. Beside the above arguments, there are some other advantages of microbatteries, which have been illustrated in Chapter 1. In summary, the flexibility of size and shape, excellent cycle life and easy combination with environmental energy harvesting systems, make thin film microbatteries indeed an ideal power solution for MEMS and sensors, which will be widely distributed in our future smart society.

Planar solid-state microbatteries are already in commercial production. The fast development of autonomous devices pushes the demand for batteries with higher energy and power density. Moving from planar layered structures to high aspect ratio 3D-structures holds promise to significantly increase the energy and power density. Many methods have been applied to deposit thin film microbatteries. However, these methods are either unsuitable for 3D deposition, such as sputtering, e-beam evaporation and pulsed laser deposition, or too slow for large-scale production, like atomic layer deposition. Low pressure chemical vapor deposition (LPCVD) stands out to be a promising method to deposit homogeneous 3D-structured thin film microbatteries with a fast growth rate. In this thesis, thin films of a solid electrolyte (LiPO) and anode materials (Si, TiO<sub>2</sub> and Li<sub>4</sub>Ti<sub>5</sub>O<sub>12</sub>) have been deposited by LPCVD. The deposition parameters have been optimized for planar thin films and the electrochemical performance of the deposited films have been investigated. What’s more, the

feasibility of 3D deposition of these film is also investigated and a Monte Carlo simulation model is built to better understand the deposition mechanism.

High quality Lithium phosphate (LiPO) thin films have been deposited by LPCVD, using tert-butyllithium and trimethyl phosphate as precursors. The LiPO films deposited at 300 °C yielded the highest ionic conductivity of  $3.9 \times 10^{-8} \text{ S} \cdot \text{cm}^{-1}$ . As the deposition temperature increases, the surface morphology of the deposited films becomes more rough. XRD results show that LiPO starts to crystallize when the deposition temperature increases beyond 350 °C. The ionic conductivity of these films quickly decreases to lower values when the deposition temperature increases. A kinetic study on planar substrates indicates that the growth of LiPO films is a diffusion-controlled process. This is confirmed by investigating the thickness development of the deposited thin films inside 3D-structures.

Silicon is an excellent anode candidate for Li-ion batteries due to its extremely high storage capacity. However, the volume expansion induces tremendous material deterioration, resulting in a poor cycle life performance. In order to cope with this shortage, various strategies have been proposed. The electrochemical performances of Si anodes with various morphologies, such as nanowires, honeycomb structures, planar thin films and 3D-film structure, are reviewed. To suppress the SEI formation and improve the cycling stability of Si anode, thin films of LiPO were deposited as protecting layer on top of Si film anodes. The normalized voltage-capacity curves show that the capacity decay of unprotected Si is mainly attributed to active material losses. A thin film of LiPO with a thickness of only 200 nm fully suppresses the SEI formation and dramatically improves the cycle life of Si thin film electrodes. The coulombic efficiency of the LiPO-protected Si anode is higher than 99.98%. Up to almost 500 cycles, hardly any capacity loss can be observed. The SEM images of Si anodes after the cycling tests revealed that the LiPO-protecting layer suppressed SEI formation completely and kept the Si film anode intact. In contrast, the unprotected-Si cracked into many pieces and the Si layer was invisible.

$\text{Li}_4\text{Ti}_5\text{O}_{12}$  is well known to be a safe and efficient anode material for Li-ion batteries. An LPCVD process has been developed for the synthesis of  $\text{Li}_4\text{Ti}_5\text{O}_{12}$  thin film anodes on planar and 3D substrates. The influence of various deposition parameters, including precursor flow rates and post-annealing temperatures, has been investigated by material and electrochemical analyses.  $\text{Li}_4\text{Ti}_5\text{O}_{12}$  thin films deposited at the optimized process parameters showed a high crystallinity and high electrochemical activity. A reversible storage capacity of 151 mAh/g was achieved at a current of 0.5 C, corresponding to 86.3% of the theoretical specific capacity of

$\text{Li}_4\text{Ti}_5\text{O}_{12}$ . Up to almost 600 cycles, the electrodes showed no significant capacity losses. Furthermore, the deposited thin film anodes also showed excellent rate capability. Compared to the storage capacity at 0.5 C, 93% of the capacity was maintained at 10 C. Thin films were also deposited on highly structured substrates to investigate the uniformity and electrochemical performance. Compared to planar substrates, the capacity per footprint area of 3D LTO electrode was improved by a factor of 2.5. Demonstrations of planar all-solid-state microbatteries, LTO/LiPON/Li, were prepared. The prepared all-solid-state batteries are electrochemically active, but with a much lower capacity. Interfaces strongly influence the electrochemical performances of all-solid-state microbatteries. To prepare all-solid-state batteries with good electrochemical performance, not only the depositions of each film component need to be optimized, but also the interfaces between various films need to be carefully designed.

$\text{TiO}_2$  has been considered as a promising electrode for Li-ion batteries since it is safe, non-toxic, readily available and has a high theoretical volumetric capacity. A flexible and deterministic 3D fabrication route to create 3D- $\text{TiO}_2$  film anodes by combining reactive ion etching with LPCVD was demonstrated. The deposition kinetics has been investigated and showed that the LPCVD deposition of  $\text{TiO}_2$  thin films can be characterized by two rate-determining processes: diffusion controlled and kinetically controlled processes. Deposition within the kinetically controlled temperature range, uniform 3D  $\text{TiO}_2$  film electrodes were achieved. Compared with planar  $\text{TiO}_2$  electrodes, the storage capacity of 3D  $\text{TiO}_2$  electrodes increased more than 6 times at low current density (footprint area current density  $4 \mu\text{A cm}^{-2}$ ) and even 16 times at a high current density ( $80 \mu\text{A cm}^{-2}$ ). The high storage capacity is maintained even after 450 cycles at low current density. Beside the significant improvement of storage capacity, the power performance is also improved. At all output power densities, the 3D  $\text{TiO}_2$  electrodes manifested a higher capacity than planar electrodes. Our results clearly demonstrate the advantages of 3D electrodes in improving the storage capacity and power performance of thin film batteries.

To better understand and improve the deposition process, the experimental results of the 3D deposition of  $\text{TiO}_2$  are combined with Monte Carlo simulations. A Monte-Carlo Markov Chain (MCMC) method is applied to model the observed deposition profiles of  $\text{TiO}_2$  inside deep trenches as a function of the depth of the trench, width of the trench and deposition temperature. A theoretical description of the Monte-Carlo method was given. For the first time,

a systematic estimation of the parameters of deposition process was performed. It was found that the probability of deposition in a single collision (reactive sticking coefficient) is close to zero in the kinetically controlled regime and close to one in the mass-transfer controlled regime. It is also shown that the reflections of precursor molecules inside the trenches play an important role in achieving homogeneous 3D deposition. Experimentally observed deposition profiles are compared with the MCMC model. Good agreement between the model and experiment has been achieved in all cases. An estimation of the precursor density in the trenches has also been extracted from the Monte-Carlo model. A sharp drop of the precursor concentration with increase of depth was detected in the diffusion-controlled regime. In the kinetically-controlled regime, the precursor concentration remains constant within the trench. The Monte-Carlo approach is found to be successful in explaining the experimentally observed deposition profiles. A “hard balls wall-collision” scheme and the absence of scattering between precursor molecules and carrying gas appear are a good approximation to describe the experimental LPCVD deposition processes.

Overall, LPCVD is a very successful method to deposit electrode and electrolyte materials for thin-film all-solid-state microbatteries. The composition and crystal structure of deposited films can easily be adjusted by changing deposition temperature and flow rates of the precursors. In addition, the deposited films are generally very homogeneous and the deposition processes are reproducible. By selecting the proper precursors, LPCVD can deposit many kinds of battery materials and is capable for large wafer deposition. However, for many materials, uniform deposition is limited to planar deposition. Homogeneous 3D deposition by LPCVD is quite challenging. The thermodynamic characteristics of precursors play a very important role in determining whether a material can be deposited uniformly on 3D substrates or not. Adjusting deposition temperature, flow rates of precursors and reactor pressure can help to improve the uniformity of 3D deposition. For future research, two approaches may help to achieve uniform 3D deposition: one is exploring single-source precursors, which combines all required elements in one precursor. This will suppress the reaction in gas phase and simplify the mass-transfer and deposition processes; the other method is adding growth inhibitors to tune the chemical reaction rate. By decreasing the surface reaction rate, the growth of thin films may shift into the kinetically-controlled region, in which homogeneous 3D films are likely to be deposited. Finally, it was commented that for successful 3D thin-film batteries, their development should go hand in hand with the development of precursors and the energy demand of micro-device.

## Acronyms

3D	three-dimensional
ALD	atomic layer deposition
a-Si	amorphous Si
CE	columbic efficiency
c-Si	crystalized Si
CV	cyclic voltammetry
CVD	chemical vapor deposition
EBPVD	electron Beam Physical Vapor Deposition
EIS	electrochemical impedance spectroscopy
EOT	end of Trajectory
GC	galvanostatic cycling
HOMO	highest occupied molecular orbital
IoT	internet of things
LiPO	lithium phosphate
LiPON	nitrogen doped lithium phosphate
LPCVD	low pressure chemical vapor deposition
LTO	$\text{Li}_4\text{Ti}_5\text{O}_{12}$
LUMO	lowest unoccupied molecular orbital
MCMC	Markov chain Monte-Carlo
MEMS	micro-electro-mechanical systems
MOCVD	metal-organic chemical vapor deposition
PC	propylene carbonate
PECVD	plasma-enhanced chemical vapor deposition



PVDF	polyvinylidene fluoride
RIE	reactive ion etching
RPCVD	reduced pressure chemical vapor deposition
SEI	solid electrolyte interface
SEM	scanning electron microscope
SMT	surface-mount technology
SoC	state-of-charge
t-BuLi	tert-butyllithium
TMPO	trimethyl phosphate
TTIP	titanium isopropoxide
XRD	X-ray diffraction

## List of symbols

$a(r)$	absorption probability
$c_s(T)$	precursor concentration at the source plane, [ $\mu\text{m}^{-3}$ ]
$D$	geometrical set of all boundary points of a trench, $D = T_1 + T_2 + W_1 + W_2 + B$
$DR$	precursor molecule composed by deposition part $D$ and residual part $R$
$\bar{d}_{wall_1}, \bar{d}_{wall_2}$	average thicknesses of the deposited material on both walls
$\bar{d}_{bot}$	average thickness of the deposited material at the bottom
$\bar{d}_{top}$	average thickness of the deposited material at the flat-top part
$\tilde{d}_{top}$	experimentally measured film thickness at the top surface
$d(z, \Delta z)$	average thickness of the deposited film in the interval $\Delta z$ around point $z$
$d_r(z)$	steady-state deposition rate around point $z$
$d_r(top)$	steady-state growth rate on the top flat part
$d\Omega$	differential solid angle
$f(top)$	density of collision numbers on the top flat part, [ $\mu\text{m}^{-2}$ ]
$f(z)$	density of collision numbers in point $z$ , [ $\mu\text{m}^{-2}$ ]
$h(z)$	density of depositions in point $z$ , [ $\mu\text{m}^{-2}$ ]. $h(z) = P_d f(z)$
$h(top)$	density of depositions on the top flat part, [ $\mu\text{m}^{-2}$ ]
$\hat{h}_N([z_{i-1}, z_i])$	average value of the density of depositions $h(z)$ in the interval $[z_{i-1}, z_i]$
$k$	proportionality constant, [ $\mu\text{m}^3/\text{s}$ ]
$M$	molecules entered system via the source boundary in time $t$
$M_z$	incoming particles in the interval $\Delta z$ around point $z$
$O$	trench opening

$P$	distribution probability of precursor molecules
$P_d$	probability of deposition in a single collision
$\bar{P}_d^{tot}$	average total deposition probability
$S$	source line, $S = T_1 + O + T_2$
$T_1, T_2$	top parts of the substrate on the left and right side of the opening
$V_{TiO_2}$	volume of a single $TiO_2$ molecule
$W_1, W_2$	two opposing walls of the trench
$Y$	length of segment along dimension $y$
$\alpha$	flying angle of precursor molecular
$\Delta$	absorbing state

# List of publications

## Peer-reviewed journal publications

1. **J. Xie**, D. Danilov, R.-A. Eichel, P.H.L. Notten; Monte Carlo Simulation of 3D Chemical Vapor Deposition of TiO<sub>2</sub>, *Journal of Physical Chemistry C*, DOI: 10.1021/acs.jpcc.6b07594.
2. **J. Xie**, J.F.M. Oudenhoven, DJ. Li, P.H.L. Notten; High Power and High Capacity 3D-structured TiO<sub>2</sub> Electrodes for Lithium-ion Microbatteries, *Journal of The Electrochemical Society*, 163 (10) A2385-A2389 (2016).
3. **J. Xie**, P.P.R.M.L. Harks, DJ. Li, L.H.J. Raijmakers, P.H.L. Notten; Planar and 3D deposition of Li<sub>4</sub>Ti<sub>5</sub>O<sub>12</sub> thin film electrodes by MOCVD, *Solid State Ionics*, 287 (2016) 83–88.
4. **J. Xie**, J.F.M. Oudenhoven, P.P.R.M.L. Harks, DJ. Li, P.H.L. Notten; Chemical Vapor Deposition of Lithium Phosphate Thin-Films for 3D All-Solid-State Li-Ion Batteries, *Journal of The Electrochemical Society*, 162 (2015) A249-A254.

## Publications out of this thesis

1. M. Ma, B.J. Trzeźniewski, **J. Xie**, W.A. Smith; Selective and Efficient Reduction of CO<sub>2</sub> to CO on Oxide-Derived Nanostructured Ag Electrocatalysts, *Angewandte Chemie International Edition*, 55 (2016) 9748-9752.
2. DJ. Li, D. Danilov, **J. Xie**, L.H.J. Raijmakers, L. Gao, Y. Yang, P.H.L. Notten; Degradation Mechanisms of C<sub>6</sub>/LiFePO<sub>4</sub> Batteries: Experimental Analyses of Calendar Aging, *Electrochimica Acta*, 190 (2016) 1124-1133.
3. **J. Xie**, XH. Wang, YC. Zhou; Corrosion Behavior of Selected MAX Phases in Hot Concentrated HCl Solution: Effect of A Element and MX Layer, *Corrosion Science*, 60 (2012) 129-135.
4. **J. Xie**, XH. Wang, YC. Zhou; Understanding Formation Mechanism of Titanate Nanowires Through Hydrothermal Treatment of Various Ti-containing Precursors, *Journal of Materials Science & Technology*, 28 (2012) 488-494.
5. X. Qin, JM Wang, **J. Xie**, L. Wen, FZ. Li, XH. Wang; Simultaneous suppression of crystal growth along [010] and antisite defect formation in hydrothermally synthesized

- LiFePO<sub>4</sub> crystals to improve electrochemical properties, *Physical Chemistry Chemical Physics*, 14 (2012) 2669-2677.
6. X. Qin, XH. Wang, **J. Xie**, L. Wen; Hierarchically Porous and Conductive LiFePO<sub>4</sub> Bulk Electrode: Binder-Free and Ultrahigh Volumetric Capacity Li-Ion Cathode, *Journal of Materials Chemistry*, 21 (2011) 12444-12448.
  7. X. Qin, XH. Wang, HM. Xiang, **J. Xie**, JJ. Li, YC. Zhou; Mechanism for Hydrothermal Synthesis of LiFePO<sub>4</sub> Platelets as Cathode Material for Lithium-Ion Batteries, *Journal of Physical Chemistry C*, 114 (2010) 16806-16812.
  8. HJ. Guo, XH. Li, **J. Xie**, ZX. Wang, WJ. Peng, QM. Sun; Effects of Ni substitution on the properties of Co<sub>3</sub>O<sub>4</sub>/graphite composites as anode of lithium ion batteries, *Energy Conversion and Management*, 51 (2010) 247-252.

#### Conference contributions

1. **J. Xie**, L. Baggetto, D.L. Danilov and P.H.L. Notten, "Silicon Anode Materials for All-Solid-State Lithium-ion Microbatteries", *TMS2013 Proceedings*, DOI: 10.1002/9781118663547.ch95, American Chemical Society, San Antonio (USA) 2013.
2. **J. Xie**, J.F.M. Oudenhoven and P.H.L. Notten, "3D Deposition of TiO<sub>2</sub> Thin Film Electrodes by Chemical Vapor Deposition", MRS fall meeting, Boston (USA) 2015.
3. **J. Xie**, P.P.R.M.L Harks, D. Li and P.H.L. Notten, "Planar and 3D deposition of lithium phosphate thin film electrolyte by MOCVD", Advanced Batteries Power Conference, Münster (Germany) 2016.
4. **Jie Xie**, D.L. Danilov, P.H.L. Notten, "Chemical Vapor Deposition of 3D-structured TiO<sub>2</sub> Electrodes for Lithium-ion Microbatteries - from experimental and simulation points of view", E-MRS spring meeting, Lille Europe (France) 2016.

## Curriculum Vitae

Jie Xie was born on the 1<sup>st</sup> of January 1986 in Hubei, China. In 2004, he started his bachelor program of metallurgical engineering at Central South University, Changsha, China. In 2008, he graduated cum laude. Directly after, he was recommended to the Institute of Metal Research, Chinese Academy of Sciences for a Master's study, with specialization in high-performance ceramics. During the Master program period, he published two papers as first author, co-authored three papers in peer reviewed journals and applied for three patents. In 2011, the master program was successfully completed and he graduated with the thesis entitled "Corrosion behaviors of MAX phases in acid and base solutions", supervised by Prof. Xiaohui Wang and Prof. Yanchun Zhou. After graduation, Jie Xie started a PhD project titled "3D all-solid-state micro-batteries" at the Eindhoven University of Technology, the Netherlands. The research has been financially supported by the SoS-Lion project (coordinated by IMEC) and is carried out in the Energy Materials and Devices group, and was supervised by Prof. Peter H.L. Notten and Prof. Rüdiger-A. Eichel.



## Acknowledgements

Like most PhD students, the journey of my PhD study is full of pains and happiness, ups and downs. My journey is a little bit more bumpy due to the reorganization of the faculty. It is the support and help from many people that makes this journey possible and joyful. Hereby, I want to express my sincere gratitude to them.

First, I want to sincerely thank my first promotor, prof. dr. Peter H.L. Notten, for his helpful and inspiring supervision and continuous support. He gave me enough freedom to do what I preferred during my PhD study while keeping the research on the right track. He is very good at explaining a concept or an idea, and is a master of making presentations. These skills are beneficial to me and will be valuable throughout my life. I thank my second promotor, Prof. dr. R-A. Eichel, who have given me a lot of suggestions on improving the skills like reasoning of ideas, writing research papers, *etc.* I thank both of them for their kindness and patience, as well as their encouragements.

I would like to thank my committee members, prof.dr.ir. J.C. Schouten, prof.dr. F.M. Mulder, prof.dr. C. Detavernier, prof.dr. R.A. van Santen and prof.dr. F. Roozeboom, for their reviews, comments, and approvals of my thesis.

My sincere thanks go to dr. H.T. (Bert) Hintzen and dr. Jos Oudenhoven. At the beginning of my PhD study, I met Bert quite a lot during the night time at the office. His enduring enthusiasm for science encouraged me a lot and his critical thinking inspired me. Jos acted like a daily supervisor at the beginning, who guided me to make batteries and operate MOCVD. Without him, my PhD journey would be much more difficult.

EMD group has a nice working atmosphere. All the students are hardworking and passionate about their work. It's a great pleasure to work with my nice group members, whom I want to thank here. Special thanks to my co-promotor, dr. Dmitry Danilov, for the help on simulation work and reviewing my thesis. I thank Xuefei Chen for the Si anode characterization, who contributed to chapter 3. Dongjiang Li, Luc Raijmakers and Peter-Paul Harks are very nice officemates and make a very good office environment. I am very grateful for the time we spent together. I also would like to thank Lu Gao, Chunguang Chen .... for the interesting discussion during coffee, lunches. Your made the PhD life more colorful.



Although there was lack of technical support, I was very lucky to get a lot of help from others, including Frank van Otten (physical department), Wytze Keuning (TNO), Tiny Verhoeven, Gijsbert Gerritsen, Dr. Sergej Pasko (Aixtron), Anneke Delsing, Marcel Vliex and Jan Verwijlen *etc.* Thanks for their kindness and generous help.

Last but not the least, I want to thank my family for their love and always support. In the middle of this PhD journey, I had many doubts and seriously considered quitting the PhD study. Without their understanding, persistent support and encouragement, I could not finish this journey alone.